**Defence, Safety and Security**
Oude Waalsdorperweg 63
2597 AK Den Haag
P.O. Box 96864
2509 JG The Hague
The Netherlands

www.tno.nl

T +31 88 866 10 00

**TNO report**

**TNO 2018 R11671**

# Wozep – WP2: update of the Aquarius models for marine pile driving sound predictions

| | |
|---|---|
| Date | January 2019 |
| Author(s) | Christ de Jong<br>Bas Binnerts<br>Mark Prior<br>Mathieu Colin<br>Michael Ainslie<br>Ingrid Mulder<br>Iris Hartstra |
| Copy no | |
| No. of copies | |
| Number of pages | 94 (incl. appendices) |
| Number of appendices | 4 |
| Sponsor | RWS WVL |
| Project name | 31130184 Wozep onderwatergeluid zeezoogdieren |
| Project number | 060.29036 |

# Contents

**Appendices**

# 1 Introduction

As part of the research programme *Wozep* (‘*Wind op zee ecologisch programma*’), which investigates the ecological effects of offshore wind energy development in The Netherlands, TNO has been asked by Rijkswaterstaat (RWS) to:

- Investigate whether or not there is a need to incorporate the frequency spectrum of the piling sound (pile driving at sea is needed during the construction of offshore wind farms) in relation to the frequency sensitive hearing in the assessment of the impact of these sounds on porpoises and seals
- Update the acoustic models (collectively known as *Aquarius*) that are being applied in studies of environmental impact assessment for marine pile driving projects

.

The first point was addressed in a memorandum [de Jong & von Benda-Beckmann, 2018]. Though no firm conclusions could be drawn yet, it is likely that some form of frequency weighting will be incorporated in future impact assessment.

The current report describes the update of the acoustic models (*Aquarius*). The goal of this update is to reduce the uncertainty in the calculated distances at which the piling sound in the North Sea could affect the hearing (TTS/PTS) of porpoises and seals or induce significant behavioural disturbance. The update concerns an attempt to improve various aspects in the modelling to reduce the uncertainties that have been observed in the Aquarius validation study [Binnerts et al, 2016].

# 2 Aquarius models

TNO uses different models (collectively known as *Aquarius*) for the calculation of underwater noise due to offshore piling activities. There are currently several Aquarius variants available:

- ***Aquarius 1***[1] combines an empirical energy source level for an equivalent point source, that has been derived from measurement data obtained during the construction of the Princess Amalia Wind Farm (Q7), with a propagation model based on the energy flux method described by Weston [1971,1976]. To date, *Aquarius 1* has been used by TNO in all assessments of the effects of offshore piling activities in the North Sea on porpoises and seals.
- ***Aquarius 2***[2] combines a detailed numerical (finite element) model of the pile and the surrounding near environment (using the finite element method) with an efficient adiabatic range dependent normal mode model for shallow water sound propagation [Zampolli et al, 2013, Nijhof et al, 2014-2015]. The excitation force of the hammer is modelled as a synthetic pulse, that is tuned to match the shape of the force pulse from a pile drivability study [Binnerts et al, 2016]. *Aquarius 2* has been used in research projects in which detailed information of pile and hammer force were available. It was benchmarked against other advanced piling sound models in the international Compile workshops [Nijhof et al, 2014].
- ***Aquarius 3***[3] is based on a novel efficient implementation of the hybrid propagation model '*Soprano'* for range-dependent shallow waveguides developed by Sertlek [2016]. It combines the accuracy of an incoherent adiabatic range dependent normal mode model with the speed of Weston's flux integral approach. For this model the same point source level has been used as for Aquarius 1, derived from measurement data obtained during the construction of the Princess Amalia Wind Farm (Q7). *Aquarius 3* has been used in the large scale impact assessment studies of underwater sound in the North Sea, such as the KEC studies [Heinis & de Jong, 2015], ship and dredger sound maps, and assessments of impulsive sound sources for the Marine Strategy Framework Directive [von Benda-Beckmann et al, 2017].

The uncertainties in all three Aquarius variants have been assessed in [Binnerts et al, 2016].

## 2.1 Uncertainty reduction for acoustic modelling for KEC

The current framework for the assessment of the impact of pile driving underwater sound on porpoises and seals (KEC, see [Heinis & de Jong, 2015]) prescribes the following steps:

1. calculation of the spatial distribution of the **single strike sound exposure level** ($SEL_{ss}$) around the pile (for the 'loudest' hammer blow during a calendar day).
2. calculation of the **area** around the pile in which that level exceeds a threshold value for behavioural disturbance (for harbour porpoises and/or seals).

[1] Current software version Aquarius 1.2
[2] Current software version Aquarius 2.1
[3] Current software version Aquarius 3.2

3. calculation of the **number of harbour porpoises and/or seals** possibly suffering **disturbance** (using abundance estimates)
4. calculation of the number of **animal disturbance days** (the number of disturbed animals per day multiplied by the number of impulse days)
5. estimation of the possible effect on the **population** on the basis of the number of animal disturbance days using the Interim PCoD model

Additionally, the Aquarius models are used to calculate the cumulative sound exposure of harbour porpoises and seals swimming in the vicinity of the pile, to determine the distance within which there is a risk on a permanent hearing threshold shift (PTS) for animals, plus an investigation and description of how this risk will be mitigated.

The first two steps above are calculated using the Aquarius models. The following steps (3 to 5) involve derived calculations and another model (Interim PCoD model, in step 5). Each step in this procedure is subject to uncertainties, in the applied models as well as in the input data to these models. In order to determine balanced requirements for reducing the uncertainty in the Aquarius models, an attempt was made for a (backward) assessment of the uncertainties. It must be concluded that most of these uncertainties cannot be quantified well, due to a general lack of knowledge and data in this relatively new field of research.

- The statistics included in the Interim PCoD model [Harwood et al, 2014; Heinis & de Jong, 2015], used in **step 5**, are based on the assumption that the estimations of the number of disturbed animals per piling day (step 3) have a normal distribution with a 25% standard deviation. Or, in other words, on the assumption that there is a 95% probability that the number of disturbed animals does not exceed the estimated mean value plus 50%.
- For a given agenda of piling days, the calculation of the number of animal disturbance days, in **step 4**, does not add uncertainty.
- The estimations of the abundance of harbour porpoises on the Dutch Continental Shelf, used in **step 3**, are reported by [Geelhoed et al 2013] with a 95% confidence interval that ranges from about -50% to about +100% around the mean value. This exceeds the uncertainty assumed in the PCoD model by a factor of 2. The consequence of this exceedance could not be investigated within the scope of this study.
- The uncertainty in the estimated threshold for value for animal behavioural disturbance, used in **step 2**, cannot be quantified due to a lack of data.
- The uncertainties in the current Aquarius acoustic model predictions (Aquarius 1, 2 and 3), used in **step 1**, are described in [Binnerts et al, 2016]. These are elaborated below.

Figure 1 (from [Binnerts et al, 2016]) shows a comparison of the predictions of the different Aquarius models with measured broadband SEL values measured at four distances from pile U8 of the Gemini wind farm.

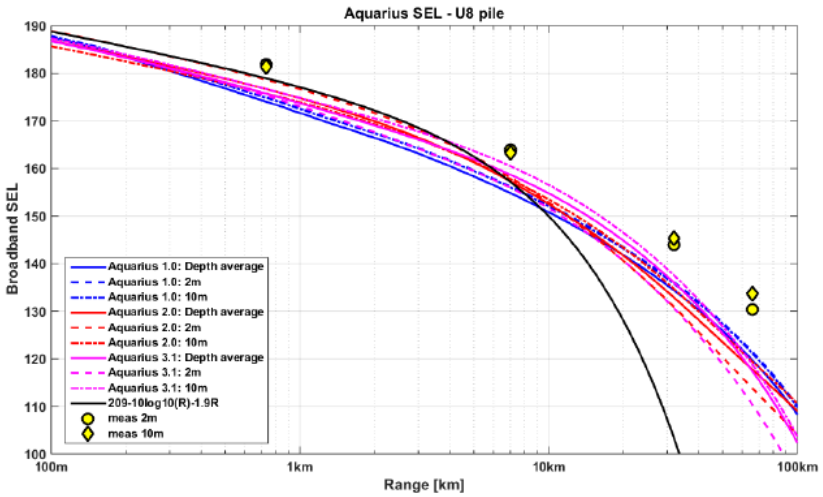


Figure 1: Comparison of the unweighted broadband singe strike sound exposure level ($SEL_{ss}$, in dB re 1 µPa²s) for measurements and the three models for Gemini pile U8 as a function of range for a constant water depth of 34 meters. The colour of the lines indicate the model versions (blue: Aquarius 1, red: Aquarius 2 and magenta: Aquarius 3). The line style indicates the hydrophone depth (solid: depth averaged SEL, dashed and dot-dashed: 2 m and 10 m above the sea floor. The black line represents a damped cylindrical spreading trend for a pile in a medium sand environment, which is close to the Aquarius 2 model prediction up to ~7 km.

The different Aquarius models predict (see the coloured lines in Figure 1) that the threshold value for avoidance behaviour in harbour porpoises (140 dB re 1 µPa²s) is exceeded at a distance of about 20 to 30 km from the pile. Assuming that the impact area is approximately circular, that means that the statistical uncertainty in the avoidance area predictions by the various model versions[4] is about 44%.

Additionally, Figure 1 shows that the predicted broadband SELs are consistently lower than the measured SELs. Interpolation between the measured SELs at 32 and 66 km from the pile indicates that the 140 dB threshold is exceeded at about 40 to 50 km from the pile, which means that the applied Aquarius models underestimate the avoidance area by a factor of 3 to 4. The statistics of the Interim PCoD modelling does not account for such a bias. Hence, an important goal for the model update described in this report is aimed at reducing this bias.

Figure 2 shows that the bias in the predictions is mainly caused by an underestimation of the SEL at the lowest frequencies (<100 to 500 Hz, dependent on the distance). This underestimation appeared to be due to the source model as well as to the description of the sediment [Binnerts et al, 2016]. Both are addressed in the Aquarius update that is described in this report.

[4] For an uncertainty $\Delta r$=5 km around an average radius $r$=25 km, the uncertainty $\Delta A$ in the area of a circle follows from: $A + \Delta A = \pi(r + \Delta r)^2$, so that $\frac{\Delta A}{A} = \frac{2r\Delta r + \Delta r^2}{r^2} \approx$

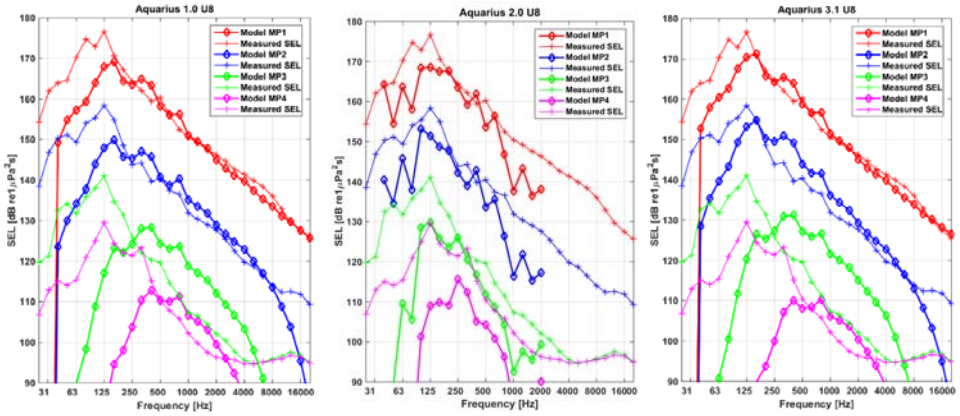


Figure 2: Aquarius 1 (left), Aquarius 2 (middle) and Aquarius 3.1 (right) model-measurement comparison of the SEL for the Gemini U8 pile, from [Binnerts et al, 2016]. The thick lines with diamond (◊) markers indicate the model predictions and the thin lines with plus (+) markers indicate the measured levels. The colours indicate the receiver range (MP1 (red) at 732 m, MP2 (blue) at 7.0 km, MP3 (green) at 31.8 km, and MP4 (magenta) at 65.8 km). Spectral levels are given at 10 m from bottom. The Aquarius 2 result has been generated for a constant water depth of 34 meter and no wind speed. The Aquarius 1 and 3.1 include the effect wind (here assumed 8.8 m/s)

As demonstrated in the first phase of this project [de Jong & von Benda-Beckmann, 2018], the selection of the metric (e.g. weighted or unweighted SEL) for which the threshold value is set has a large impact on the calculated disturbance area. The uncertainty (and bias) associated with this selection can only be reduced by further studies and data gathering, aimed at a better understanding of how to quantify a 'significant behavioural response', which metric provides the best indicator for such a response and what is the appropriate threshold value for that indicator.

In KEC related studies, the Aquarius models are used to calculate an unweighted broadband $SEL_{ss}$ in dB re 1 $\mu Pa^2s$, with a corresponding threshold value for behavioural response of porpoises. If a metric would be selected that incorporates the frequency sensitivity of porpoise or seal hearing, which deemphasizes the relevance of the lower frequencies, the deviations between Aquarius 1 predictions and measurements at various distances from a pile in the Gemini wind farm are strongly affected, as can be seen in Table 1 (from [de Jong & von Benda-Beckmann, 2018]).

Table 1 Unweighted and weighted broadband values of single strike sound exposure level as measured and calculated (Aquarius 1) for the piling of Gemini pile U8. Weighting functions for porpoises (HF = high frequency cetaceans) and seals (PW = phocoid pinnipeds in water) are taken from the 'Technical Guidance for Assessing the Effects of Anthropogenic Sound on Marine Mammal Hearing: Underwater Acoustic Thresholds for Onset of Permanent and Temporary Threshold Shifts' from the US National Marine Fisheries Service [NMFS 2016].

| | | | MP1 | MP2 | MP3 | MP4 |
|---|---|---|---|---|---|---|
| | Distance | km | 0.7 | 7 | 32 | 66 |
| | Calculated unweighted $SEL_{ss}$ | dB re 1 $\mu Pa^2s$ | 174 | 156 | 134 | 119 |
| | Measured unweighted $SEL_{ss}$ | dB re 1 $\mu Pa^2s$ | 178 | 163 | 144 | 128 |
| | Unweighted calculated - measured | dB | -4 | -7 | -10 | -9 |
| porpoise | Calculated NMFS HF $SEL_{ss}$ | dB re 1 $\mu Pa^2s$ | 132 | 111 | 91 | 77 |
| | Measured NMFS HF $SEL_{ss}$ | dB re 1 $\mu Pa^2s$ | 133 | 112 | 84 | 67 |
| | NMFS HF calculated - measured | dB | -1 | -2 | +7 | +10 |
| seal | Calculated NMFS PW $SEL_{ss}$ | dB re 1 $\mu Pa^2s$ | 156 | 139 | 122 | 108 |
| | Measured NMFS PW $SEL_{ss}$ | dB re 1 $\mu Pa^2s$ | 157 | 141 | 121 | 107 |
| | NMFS PW calculated - measured | dB | -1 | -2 | +1 | +1 |

The uncertainty in the $SEL_{ss}$ calculations depends on the selected metric (weighted or unweighted) as well as on the specifics of the scenario for which these calculations are performed. The observed maximum deviation of $\pm$10 dB between calculated and measured $SEL_{ss}$ values for the Gemini piling, dependent on the selected metric (see Table 1), is too large for a reliable impact assessment.
To achieve an uncertainty of less than 10 dB (and a smaller bias) in unweighted as well as in frequency weighted broadband $SEL_{ss}$ calculations, not only the broadband value but also the underlying frequency spectrum of the received piling sound must be determined sufficiently accurately.

## 2.2 Model improvements incorporated in "Aquarius 4"

The aim of the 'Aquarius update' project is to reduce the uncertainty in the acoustic modelling that is applied in environmental impact assessment studies and in the development of permitting conditions for future windfarm installations.

The current modelling uncertainties are described in [Binnerts et al, 2016].
To address the required reduction of uncertainty (see Section 2.1),a new 'hybrid' Aquarius model version (Aquarius 4) has been developed, in which updated versions of modules of the existing models are combined to achieve a more reliable and numerically efficient model that is fit for use in the early stages of wind farm development, where the precise details of piles, hammers and environmental parameters are not readily available. This model version is also applicable for studies of ambient noise in the North Sea (e.g. for making sound maps in the JOMOPANS project[5]) and for large scale studies of cumulative impact (e.g. in the impact assessment of impulsive sources for indicator 11.1 of the European Marine Strategy Framework Directive).

The updated **'Aquarius 4**' model combines the normal mode propagation loss modelling approach as used in the current 'Aquarius 2' with new simplified line

[5] INTERREG VB Joint Monitoring Programme for Ambient Noise in the North Sea, see https://northsearegion.eu/jomopans/

source models for the pile. The Aquarius 4 development includes the following model updates:

A. A normal mode propagation model (such as currently used in Aquarius 2 and 3) with an appropriate normal mode solver (Chapter 3).

B. A line source model, to provide a better description of the 'Mach waves' radiated by the pile and the associated directivity of the radiated sound than the current point source model used in Aquarius 1 (Chapter 4). This improves the description of the actual physics of the acoustic source mechanism in the modelling.

C. An energy flux model (such as currently used in Aquarius 1 and 3) to evaluate the trends calculated by the normal mode model and, possibly, for future extension of the modelling capability towards higher frequencies where the normal mode model may be too computationally expensive (Section 4.3).

D. A model for the hammer force, as input for a line source model, to replace the current empirically derived point source level (Chapter 5). This reduces the uncertainties associated with scaling the source level with pile diameter, water depth and hammer mass and energy. It is also applicable for the finite element modelling in Aquarius 2.

E. An updated model for the effects of wind induced bubbles (absorption) and surface waves (scattering) on the calculated propagation loss (Chapter 6). This mainly addresses the uncertainty of the current extrapolation of mid frequency (1-4 kHz) wind models towards lower frequencies.

F. An updated geoacoustic model for the description of the acoustic properties of the sediment in the propagation loss model (Chapter 7). This mainly addresses the current overestimation of low frequency (<1 kHz) propagation loss due to the extrapolation of mid frequency (1-10 kHz) sediment parameters towards lower frequencies.

G. A first-order model for the frequency dependent loss associated with mitigation measures such as bubbles screens (Chapter 7). This is needed to address the predicted effectiveness of underwater noise limits (at 750 m from the pile) for controlling the calculated disturbance area, in particular when this will be based on (porpoise) weighted $SEL_{ss}$ criteria, for which the mitigation measures are much more effective than for unweighted $SEL_{ss}$ criteria.

H. Update and verification of the Aquarius modelling suite infrastructure (Chapter 9)

## 2.3 Validation of model improvement

The various updates and improvements to the Aquarius modelling would ideally require a step-by-step experimental validation. Unfortunately, the number of parameters of hammers, piles and environment for which the model has been updated exceeds the amount of scenarios for which measurement data are available. This is illustrated by an overview of North Sea piling sound data available at TNO, see de Jong & Ainslie [2012], Remmerts & Bellmann [2015&2016].
The relevant parameters for the projects in which these data were measured are summarized in Table 2. Example data are shown in Figure 3.

These figures illustrate that the received sound exposure levels in vary in (1/3-octave bands) by up to 20 dB. The corresponding broadband levels (summed over the spectrum) are dominated by the frequency bands between (roughly) 50 Hz and 500 Hz. The unweighted broadband levels differ by at maximum 10 dB.

Many parameters differ between the various data sets. These parameters all have their specific effect on sound generation and propagation, so it is nearly impossible to draw firm conclusions on how valid the individual model updates for source and propagation effects are on the basis of these limited data. Only the combined effect of the updates on the total predicted levels at the hydrophones can be evaluated.

Some global conclusions can however be drawn from the available data:

- The largest piles in the deepest water (Gemini U8 & Z2) produce the highest SEL, particularly at low frequencies (below ~200 Hz), which dominate the unweighted broadband SEL. The dependence of radiated sound on pile diameter and water depth was not accounted for the Aquarius 1 model. It is addressed in the updated source model in Aquarius 4 (Chapters 4 and 5).
- At higher frequencies (above ~200 Hz) measurements show a dependency on wind speed: at a higher wind speed (U8, EL42) the measured SEL values are lower than in the same environment at lower wind speed (Z2, EL39), see Figure 3 (mid). This is addressed in the updated wind loss model in Aquarius 4 (Chapter 6).

Table 2 Overview of data from North Sea wind farm projects for which underwater noise data are available at TNO [de Jong & Ainslie, 2012], [Remmerts & Bellmann, 2015-2016].

| **Project** | | **Gemini** | | | **Luchterduinen** | | **PAWP (Q7)** | |
|---|---|---|---|---|---|---|---|---|
| **Pile** | | **U8** | **Z2** | **OHVS** (jacket) | **EL39** | **EL42** | **53** | **OHVS** |
| Pile diameter [m] | | 7.0 | 6.6 | 2.4 | 5.0 | 5.0 | 4.0 | 4.0 |
| Pile length [m] | | 66.5 | 63.4 | 58.4 | 68.4 | 75.9 | 54.0 | 54.0 |
| Hammer energy [kJ] | | 1100 | 600 | 600 | 750 | 1100 | 800 | 800 |
| Water depth at the pile [m] | | 34.1 | 30 | 35 | 21.5 | 20.6 | 21.5 | 22 |
| Average wind speed [m/s] | | 8.8 | 6.6 | 4 | 5 | 9 | 4-6 | 4-6 |
| Measurement distance [m] | MP1 | 732 | 677 | 921 | 750 | 750 | 891 | 981 |
| | MP2 | 7017 | 3933 | 5100 | 4724 | 5245 | 1079 | 1209 |
| | MP3 | 31816 | 28059 | 20163 | 13232 | 13749 | 3200 | 2226 |
| | MP4 | 65764 | 61891 | 54069 | 46578 | 47054 | - | 5650 |

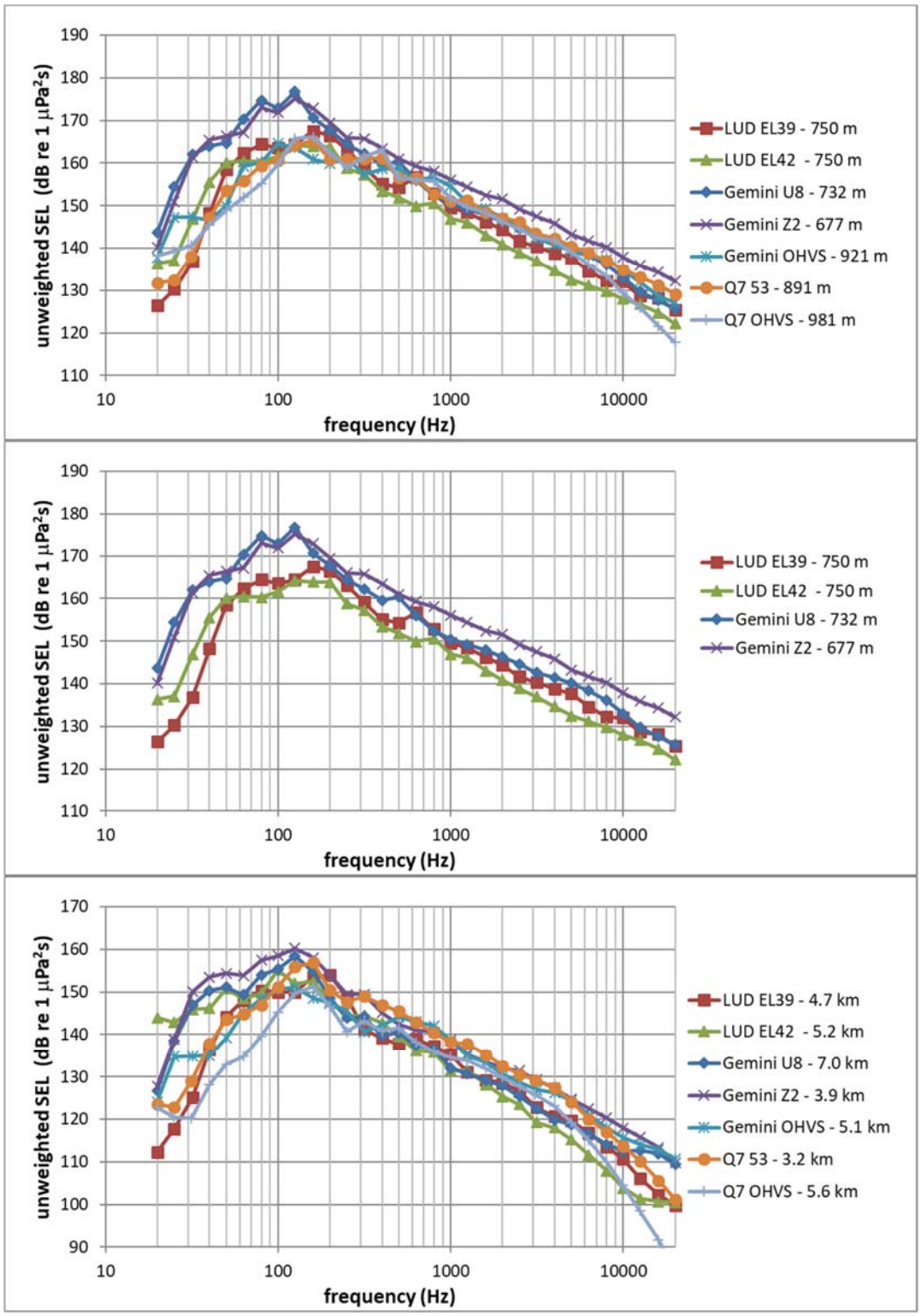


Figure 3 Average one-third octave band spectra of the measured single strike sound exposure level for the different North Sea piling projects summarized in Table 2. Upper figure: measurement positions close to the reference distance (750 m), mid figure: just LUD and Gemini piles to illustrate effect of wind, lower figure: positions between 3 and 7 km from the pile.

# 3 Selection of an appropriate normal mode solver

## 3.1 Introduction

The Aquarius 2 and Aquarius 3 models both make use of a normal mode model [Jensen et al, 2001] to compute the propagation of sound underwater using adiabatic mode theory and disregarding the contribution of the branch cut integral [Porter, 2001]. The difference between the models is the way how they compute the complex wavenumber associated with the normal modes in the waveguide representation of the shallow water environment.

*The Aquarius 2 model* uses an external numerical rootfinder to find these modes. Two implementations of such rootfinders are available to TNO:

a) A solver for the complex eigen-values of the dispersion equation for an axisymmetric Pekeris waveguide, developed by TNO (a Matlab based implementation). This implementation is more exact than the solver used by Aquarius 3 (see below) but also less computationally efficient.
The advantage of this rootfinder over the KrakenC rootfinder (see below) is that the details of the software are better understood because it was internally developed, enabling easier future maintenance. Although this solver is currently limited to a description of the sea bottom as a semi-infinite uniform 'equivalent' fluid, it can be extended to include multiple sediment layers and sediment shear properties. This in-house developed solver is not yet integrated in the Aquarius software.

b) An open source finite difference-based solver, which is part of Mike Porter's 'KrakenC' normal mode propagation code [Porter, 2001] available from the Ocean Acoustics Library site[6] (implementation in Fortran). The KrakenC solver includes the options to model multiple sediment layers and sediment shear properties. Also, the KrakenC code is widely known and tested by the underwater acoustic community. A disadvantage of the KrakenC code is that future development is more costly than development of in-house developed code, as this would require additional effort to understand all details of the existing implementation. On the other hand, there is currently no need for editing as the code fulfills the requirements. The computational efficiency of this solver is equal to the Matlab based implementation described above. The KrakenC solver is already integrated in the Aquarius software.

*The Aquarius 3 model*, based on the 'Soprano' model developed by Özkan Sertlek in his PhD project [Sertlek, 2016], calculates the analytic mode shapes of an equivalent free-free fluid wave guide, using Weston's 'effective depth' approximation, in combination with an approximation of the modal loss factor, as introduced by Kornhauser and Raney [1955]. This solver is computationally very efficient, but increasingly inaccurate for larger modal grazing angles (i.e. for decreasing water depth and frequency).

[6] http://oalib.hlsresearch.com/Modes/index.html

Prior to the implementation of improved models for the line source and of effects of wind and seabed properties on propagation loss, the output of the three mode solvers is compared. A description of the benchmark scenario is provided in Section 3.2. In Section 3.3 the model output is compared and conclusions are drawn on the performance of the three solvers. Finally, recommendations are given on the future use of the models in Section 3.4.

## 3.2 Verification scenario

In order to assess the accuracy of the three models describes in Section 3.1, their output is compared for four constant water depths ranging from 10 m to 40 m with steps of 10 m. The sediment is modelled as a semi-infinite fluid layer with 'medium sand' properties in accordance with the values from table 4.18 in [Ainslie, 2010], the sound speed is modelled as being constant over the water column and the effect of surface disturbance by wind is not considered. Table 1 provides the parameter values (density $\rho$, sound speed $c$ and attenuation $\alpha$) used as input for the models.

Table 3: description of selected environmental parameters for the North Sea scenarios.

| | |
|---|---|
| **Wind** | No wind modelled, ocean surface considered flat |
| **Sediment** | $\rho_s$= 2136 kg/m$^3$, $c_s$=1797 m/s, $\alpha_s$=0.88 dB/$\lambda$ |
| **Water** | $\rho_w$=1024 kg/m$^3$, $c_w$=1500 m/s, $\alpha_w$=0 dB/km |
| **Water depth** | 10 m, 20 m, 30 m and 40 m |

## 3.3 Comparison of root finders

For the environmental parameters described in Table 3, the output of the three rootfinders is compared in order to gain a better understanding of their numerical accuracy.

In normal mode modelling, the real part of the horizontal mode wavenumber $\kappa_m$ as computed by the rootfinders determines the mode shape ($\Psi_m$) and the imaginary part determines the modal damping and phase of the modes. In the Aquarius normal mode models, the incoherent mode sum transmission loss (TL) is computed using the asymptotic approximation of the Hankel function, as derived in [Jensen et al, 2011, eq.(5.18)] for a range independent scenario:

$$\mathrm{TL}(r,z) = -20\log_{10}\left\{\frac{1}{\rho_w}\sqrt{\frac{2\pi}{r}\sum_{m=1}^{\infty}\left|\Psi_m(z_s)\Psi_m(z)\frac{\mathrm{e}^{\mathrm{i}\kappa_m r}}{\sqrt{\kappa_m}}\right|^2}\right\}\ \mathrm{dB}$$

As explained in [Jensen et al, 2011], a mode can be thought of as consisting of an up and down going plane wave with an angle of propagation $\theta_m$ defined by

$$\theta_m = \tan^{-1}(\gamma_m/|\kappa_m|)$$

with horizontal mode wavenumber $\gamma_m = \sqrt{k_w^2 - |\kappa_m|^2}$ , and $k_w = 2\pi f/c_w$ the acoustic wavenumber in water.

The modal angle of propagation corresponds with the grazing angle at which the sound waves interact with the seabed. Modes whose angles are less than the 'critical angle' $\theta_c = \cos^{-1}(k_s/k_w)$, with $k_s = 2\pi f/c_s$ the wavenumber for compressional waves in the sediment, are trapped in the water, i.e. radiate little

energy into the seabed. Modes whose angles are greater than the critical angle are so-called ‘leaky’ modes, that lose a significant amount of their energy to the lower half-space with every refection.

Hence, each mode of the waveguide is associated with a modal damping (in dB) due to mode-sediment interaction:

$$\text{Modal damping (dB)} = 20\log_{10}\left(\left|\mathrm{e}^{\mathrm{i}\kappa_m r}\right|\right)\ \text{dB} = -\text{Imag}(\kappa_m) r \cdot 20\log_{10}(\mathrm{e})\ \text{dB}$$

Figure 4 and Figure 5 visualize the calculated modal damping as a function of mode angle. The figures show the results for the parameters described in Table 3, for one-third octave band centre frequencies ranging from 25 to 250 Hz (Figure 4) and for the centre frequency of the 20 kHz band (Figure 5). The circle markers represent the results of the TNO model, the crosses the KrakenC model, and the dots the Aquarius 3 ‘effective depth’ based model. The modal damping is computed at a horizontal distance $r$ equal to 10 times the water depth. The following observations can be made from this comparison:

- The KrakenC and the TNO model find the same wave numbers (mode angle and damping), except above and very close to the critical angle, where the TNO model is better able of finding the leaky modes than the currently used version of KrakenC, as shown by the circle and cross markers plotted in Figure 4. However, these modes are less relevant for long range propagation.
- For the 10 m depth scenario, the TNO model found modes for the 25 and 32 Hz centre frequencies with mode grazing angle close to 0 and very small modal damping. The model however does not find modes at 40 and 50 Hz, and predicted a higher modal loss for the first modes at higher frequencies. Although it is not understood what is the mechanism for these modes to be found, these modes should be disregarded as they are well below the waveguide cut-off frequency.
- The modal grazing angles and damping computed by the effective depth based model deviate significantly from the KrakenC and TNO models, making this less suitable for this application, as the other are fast enough to be used for pile driving modelling.

Finally, with regard to the computational efficiency of the models, it was found that although significantly slower than the effective depth based model, both the TNO and KrakenC rootfinders are sufficiently fast for North Sea piling noise simulations.

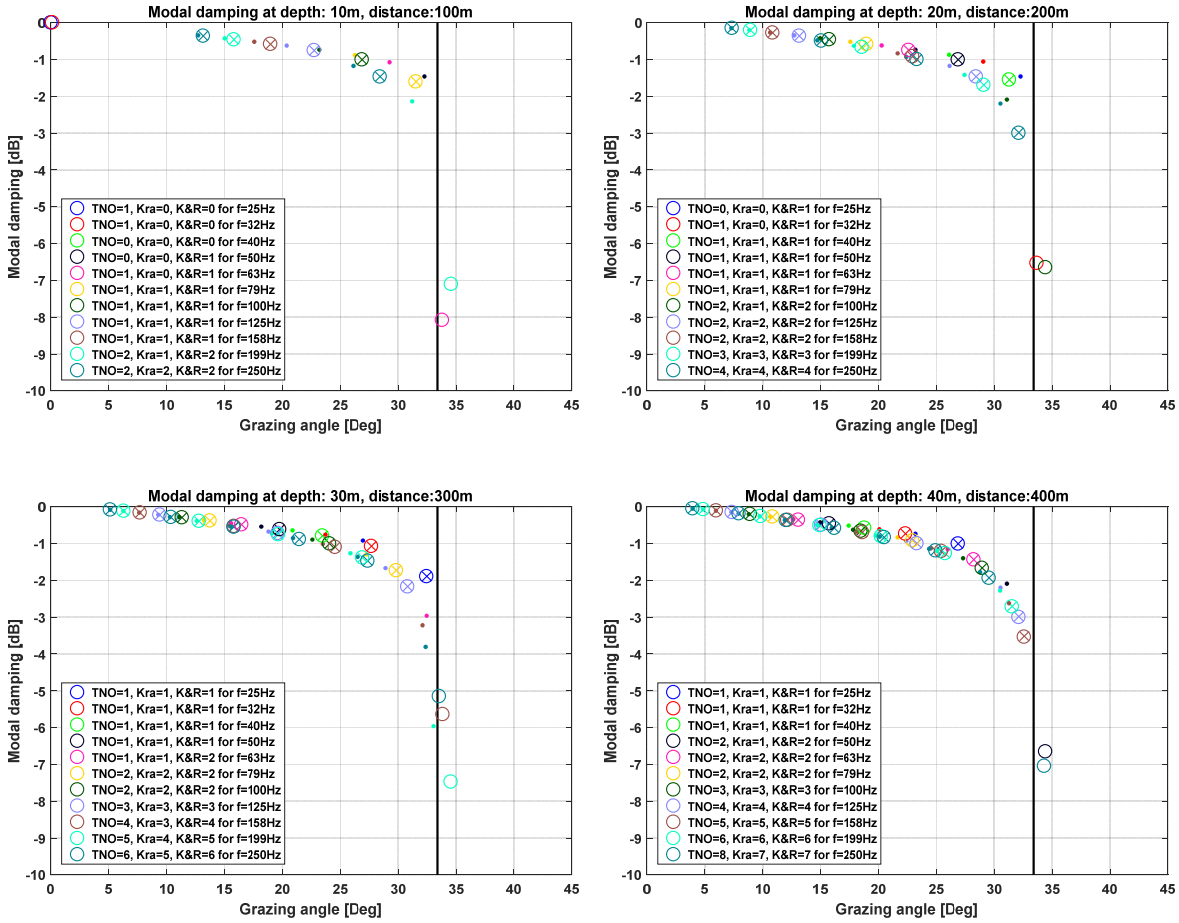


Figure 4: Modal damping against mode grazing angle at a range of 10 times the water depth. Results are shown for 10, 20, 30 and 40 m water depth and for the parameters described in Table 3. The 'O' markers indicate the results of the TNO model, the 'X' markers the KrakenC model ('Kra'), and the dots the 'effective depth' based model ('K&R'). The colours of the markers correspond with the different frequencies, which indicated in the legend together with the number of modes found by the three algorithms. The vertical line indicates the critical angle for this scenario.

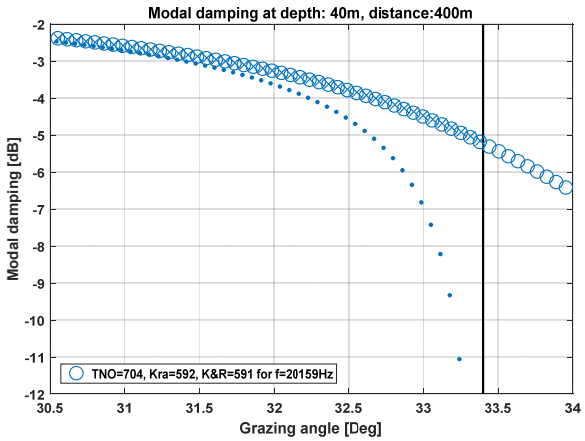


Figure 5: Plot of the modal damping against mode grazing angle for the 20 kHz third octave band.

## 3.4 Conclusion

From the rootfinder model comparison (described in 3.3) it was found that the performance of the KrakenC and TNO codes for finding the wavenumber (mode angle and modal damping) of the propagating modes for the relevant water depth found in the North Sea is equal.

The in-house TNO model has the advantage that it enables to calculate the contribution of the leaky modes, which can play a significant role at short ranges (a few water depths) and low frequencies. It is important to note however that the incoherent normal mode modelling approach used by the Aquarius models is increasingly inaccurate at these short ranges. Improving the accuracy of the modelling close to the pile is considered less relevant for the large scale cumulative impact assessment studies that are considered in Wozep.

The ‘effective depth’ based rootfinder used by Aquarius 3 has the advantage that it is faster than the other two. However, the resulting modes deviate significantly from those found by the complex mode solvers. The implications of these differences have not been further investigated. Because for the North Sea pile driving noise assessments the amount of simulations that needs to be carried out is of manageable order of magnitude, there seems no need to favour the faster effective depth based approach over the other two mode solvers for future studies.

For the Aquarius update described in the next chapters, we have decided to make use of the KrakenC mode solver. As KrakenC was already integrated in the Aquarius modelling software, this is the model that was used to generate mode look-up tables for the Aquarius 4 code introduced in this report.

# 4 Line source models (improvements B and C)

The compressional waves that travel down the pile after each hammer strike travel faster than the sound speed in water and hence result in a so-called ‘Mach wave’. The sound radiation from the pile in these Mach waves has a strong directionality, with the main sound energy radiated in angles of about 17 degrees from the direction normal to the pile axis, see Figure 6. This directionality is not captured by the omni-directional point source models applied in the current Aquarius 1 & 3 approach. One of the main recommendations that followed from the VUM-validation project [Binnerts et al, 2016] was to include the directionality of the radiation in these models.

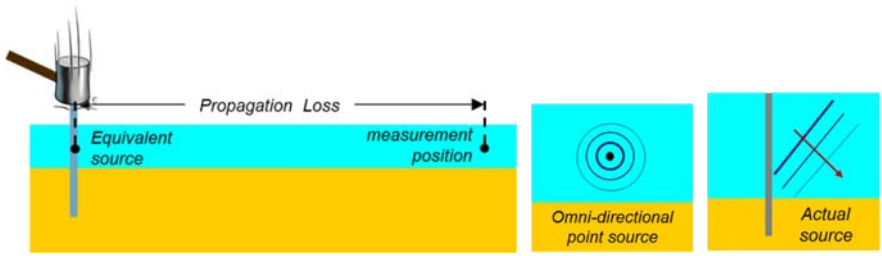


Figure 6 Sketch of the use of the equivalent omni-directional point source model in Aquarius 1 & 3 (middle) compared to the line source behaviour of the pile during percussive piling used in Aquarius 2 and 4 (right). The ‘grazing’ angle between the propagation direction (arrow in sketch of line source) and the sea floor is referred to as the ‘Mach-angle’.

The finite-element (FE) analysis of the pile in the Aquarius 2 model includes the directionality of the ‘Mach wave’. However, this FE approach requires the availability of sufficient details of the pile geometry to create a model, and, because of the computational requirements, this approach is less suitable for modelling the sound radiation at frequencies of more than a few kHz. As these higher frequencies include the majority of the energy when applying auditory weighting functions [de Jong & von Benda-Beckmann, 2018], it is critical to be able to model the sound propagation at these frequencies accurately.

We have investigated two simplified approaches to model the line source.

The first approach (Sections 4.1 and 4.2) uses a one-dimensional model for waves travelling up and down the pile, where these waves are directly converted to an array of acoustic sources, as input for the normal mode propagation model. This wave model is excited by the hammer force from the model described in Chapter 5.

The second approach (Section 4.3) applies an energy flux approach in which the vertical directivity of the line source is taken into account. For the higher frequencies where the acoustic energy is mainly radiated at the Mach cone angle this leads to a ‘damped cylindrical spreading’ [Zampolli et al, 2013] [Lippert et al, 2018].

## 4.1 One-dimensional pile model (Improvement B)

### *4.1.1 Introduction*

To first approximation, the sound radiation from pile driving is governed by the pulse that travels down the pile and is reflected up at the pile end. The local axial compression of the pile wall due to this pulse results in a radial expansion of the pile diameter. This time varying diameter change creates an acoustic volume velocity. A first order approximation of this behaviour can be described in a one-dimensional model of the pile as an acoustic waveguide.

### *4.1.2 Derivation of governing wave equations in pile*

In a one-dimensional approach, the pile impedance is governed by axial compression waves travelling down the pile. Ignoring the effects of interaction with the surrounding water and sediment, harmonic axial waves in the pipe wall (force $F = \hat{F}e^{-\mathrm{j}\omega t}$ and displacement $u = \hat{u}e^{-\mathrm{j}\omega t}$) are governed by the equations [de Jong, 1994]:

$$\frac{\mathrm{d}\hat{F}}{\mathrm{d}z} = -\rho_p A_p \omega^2 \hat{u} \quad \text{and} \quad \frac{\mathrm{d}\hat{u}}{\mathrm{d}z} = \frac{1}{E_p A_p}\hat{F},$$

with pipe wall material density $\rho_p$ and Young's modulus $E_p$ and pipe wall cross-sectional area $A_p$. For a thin-walled pipe of radius $a$ and wall thickness $h$ ($\ll a$): $A_p \approx 2\pi a h$.

Wave solutions are

$$\hat{F}(\omega, z) = \hat{F}_+(\omega)e^{\mathrm{j}k_p z} + \hat{F}_-(\omega)e^{-\mathrm{j}k_p z}$$

$$\hat{u}(\omega, z) = \frac{1}{-\mathrm{j}\omega Z_p}\left(\hat{F}_+(\omega)e^{\mathrm{j}k_p z} - \hat{F}_-(\omega)e^{-\mathrm{j}k_p z}\right)$$

With axial wavenumber $k_p = \frac{\omega}{c_p} = \omega\sqrt{\frac{\rho_p}{E_p}}$ and axial pile wall impedance

$$Z_p = \frac{k_p E_p A_p}{\omega} = A_p \rho_p c_p.$$

For a uniform pile of length $L$, terminated with impedance $Z_L$:

$$\hat{F}(\omega, L) = \hat{F}_+ e^{\mathrm{j}k_p L} + \hat{F}_- e^{-\mathrm{j}k_p L} = -\mathrm{j}\omega Z_L \hat{u}(\omega, L) = \frac{Z_L}{Z_p}\left(\hat{F}_+ e^{\mathrm{j}k_p L} - \hat{F}_- e^{-\mathrm{j}k_p L}\right)$$

So that: $\hat{F}_- = \hat{F}_+ \frac{Z_L - Z_p}{Z_L + Z_p} e^{2\mathrm{j}k_p L}$

The hammer force on the pile (see Chapter 5) can be estimated from the velocity of the hammer ('ram') mass and the impedance of the pile. According to the one-dimensional wave model, the impedance as seen by the hammer on top of the pile is:

$$Z(\omega, 0) = \frac{\hat{F}(\omega, 0)}{-\mathrm{j}\omega\hat{u}(\omega, 0)} = Z_p \frac{\hat{F}_+ + \hat{F}_-}{\hat{F}_+ - \hat{F}_-} = Z_p \frac{Z_L \cos k_p L - \mathrm{j}Z_p \sin k_p L}{Z_p \cos k_p L - \mathrm{j}Z_L \sin k_p L}$$

- For a semi-infinite ($L \to \infty$) pile $Z_L = Z_p$ and hence $Z(\omega, 0) = \frac{\hat{F}(\omega,0)}{-\mathrm{j}\omega\hat{u}(\omega,0)} = Z_p$.
- For a finite pile with a free end $Z_L = 0$ and hence $Z(\omega, 0) = -\mathrm{j}Z_p \tan k_p L$

The force distribution along the pile is:

$$\hat{F}(\omega,z) = \hat{F}_+\left(e^{\mathrm{j}k_p z} + \frac{Z_L - Z_p}{Z_L + Z_p} e^{2\mathrm{j}k_p L - \mathrm{j}k_p z}\right)$$
$$= \hat{F}_+ e^{\mathrm{j}k_p L} \frac{2}{Z_L + Z_p}\left(Z_L \cos k_p(L-z) - \mathrm{j}Z_p \sin k_p(L-z)\right)$$

For a given excitation force $\hat{F}_0(\omega) = \hat{F}(\omega,0)$ it follows that:

$$\hat{F}_0(\omega) = \hat{F}_+\left(1 + \frac{Z_L - Z_p}{Z_L + Z_p} e^{2\mathrm{j}k_p L}\right) = \hat{F}_+ e^{\mathrm{j}k_p L} \frac{2}{Z_L + Z_p}\left(Z_L \cos k_p L - \mathrm{j}Z_p \sin k_p L\right)$$

Hence:

$$\hat{F}(\omega,z) = \hat{F}_0(\omega) \frac{Z_L \cos k_p(L-z) - \mathrm{j}Z_p \sin k_p(L-z)}{Z_L \cos k_p L - \mathrm{j}Z_p \sin k_p L}$$

- For a semi-infinite pile: $\hat{F}(\omega,z) = \hat{F}_0(\omega) e^{\mathrm{j}k_p z}$
- For a finite pile with a free end ($Z_L = 0$): $\hat{F}(\omega,z) = \hat{F}_0(\omega) \frac{\sin k_p(L-z)}{\sin k_p L}$

### 4.1.3 *Damping in the pile*

The effect of damping in the pile material and, more important, due to interaction with the surrounding water and in particular the sediment can be incorporated by adding an imaginary part (loss factor $\eta \ll 1$) to the wave number:

$$k_p^* = k_p(1 + j\eta)$$

This may be different for different sections of the pile, embedded in different surrounding media, but that effect has not yet been included in the Aquarius 4 code, as we do not expect that this effect has a significant impact on the modelling results.

### 4.1.4 *Anvil*

The hammer usually hits the top of the pile via a so-called ‘anvil’. This is a steel structure that transfers the hammer force from the central excitation position to the cylindrical pile wall. The mass $M_A$ of this anvil reduces the force transmitted to the pile wall:

$$\hat{F}(\omega,0) = \hat{F}_0(\omega) - M_A\omega^2\hat{u}(\omega,0) = \hat{F}_0(\omega) - \frac{M_A\omega^2}{-\mathrm{j}\omega Z(\omega,0)}\hat{F}(\omega,0)$$

Hence, the excitation force on top of the pile (under the anvil) for a given hammer force $\hat{F}_0(\omega)$ is:

$$\hat{F}(\omega,0) = \frac{Z(\omega,0)}{Z(\omega,0) + \mathrm{j}\omega M_A}\,\hat{F}_0(\omega)$$

Hence the anvil reduces the force transmitted to the pile at frequencies where its mass impedance ($M_A\omega$) is of the same order of magnitude or larger than the pile impedance ($Z(\omega,0)$).

For example: a steel cylinder pile of 6 m diameter, with a wall thickness of 60 mm, has an axial pile impedance $Z_p \approx 46\ \mathrm{MNs/m}$. The mass impedance of a steel anvil of the same diameter, with a mass $M_A = 50{,}000\ \mathrm{kg}$ equals the pile impedance at about 150 Hz. The anvil mass reduces the transmitted force above that frequency.

However, the high-frequency response of the anvil will be dominated by modal behaviour that is not described by the mass impedance.

The force along the pile under the anvil is:

$$\hat{F}(\omega,z) = \hat{F}_0(\omega)\left(1+\frac{\mathrm{j}\omega M_A}{Z(\omega,0)}\right)^{-1}\frac{Z_L\cos k_p(L-z)-\mathrm{j}Z_p\sin k_p(L-z)}{Z_L\cos k_pL-\mathrm{j}Z_p\sin k_pL}$$
$$= \hat{F}_0(\omega)\frac{Z_L\cos k_p(L-z)-\mathrm{j}Z_p\sin k_p(L-z)}{Z_L\cos k_pL-\mathrm{j}Z_p\sin k_pL+\frac{\mathrm{j}\omega M_A}{Z_p}\left(Z_p\cos k_pL-\mathrm{j}Z_L\sin k_pL\right)}$$

- For a semi-infinite pile: $\hat{F}(\omega,z)=\hat{F}_0(\omega)\left(1+\frac{\mathrm{j}\omega M_A}{Z_p}\right)^{-1}e^{\mathrm{j}k_pz}$
- For a finite pile with a free end: $\hat{F}(\omega,z)=\hat{F}_0(\omega)\left(1-\frac{\omega M_A}{Z_p\tan k_pL}\right)^{-1}\frac{\sin k_p(L-z)}{\sin k_pL}$

The effect of the anvil is included in the 'Deeks' hammer model described in Section 5.1.

#### *4.1.5 Radial expansion*

Radial motion of the pile will result in acoustic radiation. The radial expansion $\hat{w}$ of the pile as a function of distance $z$ can be inferred from the local compression of the pile:

$$\frac{\hat{w}(\omega,z)}{a}=\nu_p\frac{\mathrm{d}\hat{u}(\omega,z)}{\mathrm{d}z}=\nu_p\frac{\hat{F}(\omega,z)}{E_pA_p}$$

So that for a semi-infinite pile excited at $z=0$:

$$\hat{w}(\omega,z)=\frac{\nu_pa}{E_pA_p}\hat{F}_p(\omega,0)e^{\mathrm{j}k_pz}$$

#### *4.1.6 Source factor for sound radiation*

The acoustic volume displacement $\hat{Q}'(\omega,z)$ per unit pile length due to radial expansion of the pile wall is:

$$\hat{Q}'(\omega,z)=2\pi a\hat{w}(\omega,z)$$

The corresponding 'rms source factor' (i.e. the product $\hat{S}=\hat{p}(r)r$ of the 'free field' sound pressure at distance $r$ and that distance) per unit pile length is:

$$\hat{S}(\omega,z)=\frac{\rho_f\omega^2}{4\pi}\hat{Q}'(\omega,z)=\frac{\rho_fa\omega^2}{2}\hat{w}(\omega,z)$$

So that:

$$\hat{S}(\omega,z)=\frac{\nu_p\rho_fa^2\omega^2}{2E_pA_p}\hat{F}(\omega,z)$$

For example, for a semi-infinite pile (without anvil) excited at $z=0$:

$$\hat{S}(\omega,z)=\frac{\nu_p\rho_fa^2\omega^2}{2E_pA_p}\hat{F}_p(\omega,0)e^{\mathrm{j}k_pz}$$

In the numerical model, the pile is discretized in segments of length $\mathrm{d}z$, which each have an energy source factor $\hat{S}(\omega, z)\mathrm{d}z$.

### *4.1.7 Limitations*

The one-dimensional pile model assumes that the compressional waves travelling down the pile are the dominant contributor to the acoustic radiation. This linear modelling approach does not describe the essential non-linear interaction between the pile and the soil. The pile-soil interaction is approximated by a linear loss factor for the axial compression waves travelling in the pile. The uncertainty associated with this approximation could not be further investigated within the scope of this project, but it contributes to the total uncertainty of the predicted piling sound levels (Section 9.4).

Higher order waves travelling along a cylindrical pile exhibit a cut-on frequency [de Jong, 1994]. In dimensionless form, these cut-on frequencies are:

$$\Omega_n^2 \approx \beta^2 \frac{n^2(n^2-1)^2}{1+n^2+2n\mu}$$

Here $\Omega_n = f_n/f_{ring}$with $f_{ring} = c_p/2\pi a$ the so-called 'ring frequency' at which a single compressional wavelength in the pipe wall fits on the circumference of the pipe. Parameter $\beta^2 = h^2/12a^2$ quantifies the ratio of wall thickness to pipe radius and $\mu = \rho_w a/\rho_p 2h$ denotes the ratio of the mass per unit length of fluid and pipe.

For example: a steel pile of 6 m diameter (radius $a = 3\ \mathrm{m}$) has its ring frequency at about $f_{ring} \approx 280\ \mathrm{Hz}$. For a wall thickness of 60 mm: $\beta \approx 0.006$ and in water $\mu \approx 3$. The $n = 2$ mode cuts on at $f_2 \approx 2\ \mathrm{Hz}$. For this example, the cut-on frequencies of the first 14 modes are all below $f_{ring}$. Hence, many higher order waves will travel in the pile, if they are excited by the hammer. This requires complex, non-axisymmetric behaviour of the hammer and anvil, which is not unlikely to occur, but difficult to quantify. These higher order waves propagate at a much lower axial speed than the $n = 0$ compressional wave in the pipe wall. For supersonic wave speeds this will result in much steeper Mach angles and subsonic waves will not radiate sound efficiently. The one-dimensional model does not include the contribution of these waves to far field sound radiation in shallow water. It is also not included in the axisymmetric finite-element model that is applied in the axisymmetric Aquarius 2 model. It is our expectation that this effect can be neglected for distances of multiple water depth.

## 4.2 A line source normal mode model (improvement C)

Line source properties can be included in a normal mode model via the modal amplitudes, in a similar manner as currently applied in Aquarius 2. In that case, the modal amplitudes are calculated from the sound pressure distribution across the water depth that is calculated by a finite element (FE) model.

Various alternatives can be considered to determine these modal amplitudes without using an FE model:

- from measurements of the sound pressure distribution across the water depth with a hydrophone array, see Dahl & Reinhall, [2013]
- from the acoustic source velocity distribution across the water depth resulting from the radial pile velocity calculated by a WEAP-type modelling

- from a description of the pile as a 'phased array', characterized by the (frequency dependent) amplitude of the down-going wave in the pile, with an appropriate estimation of the speed of that wave, possibly supplemented by a reflection coefficient at the lower end of the pile, see Reinhall & Dahl [2011] who include this 'phased array' description directly into the propagation modelling, via a coherent sum over calculations for the (phased) point sources in the array.

The third option is elaborated in the context of this project, based on the one-dimensional pile model that is described in Section 4.1.

### *4.2.1 Modal amplitudes*

In the normal mode models, the (complex) frequency domain sound field $\hat{p}(r,z)$ due to a point source at depth $z_s$ and range $r = 0$ in an range independent waveguide is expanded in terms of normal modes as

$$\hat{p}(r,z) \approx \frac{\mathrm{j}}{4\rho(z_s)} \sum_{m=1}^{\infty} \hat{S}(\omega)\Psi_m(z_s)\Psi_m(z)\, H_0^{(1)}(k_{rm}r)$$

Here, j is the imaginary unit, $\rho(z_s)$ represents the density of sea water at depth $z_s$, the functions $\Psi_m(z)$ describe the mode shapes (in the $z$ direction) and the Hankel function of the first kind of order zero $H_0^{(1)}(k_{rm}r)$ describes the propagation for each mode $m$ in radial direction $r$, with radial wave number $k_{rm}$. The term $\hat{S}(\omega)$ is the frequency dependent 'source factor' that describes the point source output in terms of the range-independent product of sound pressure and distance that would be observed due to a point source of the same volume velocity as the true source in a homogeneous free field.

For a line source with depth dependent source factor $\hat{S}(z_s,\omega)$ the pressure response is:

$$\begin{aligned}\hat{p}(r,z) &\approx \int_0^{\infty} \frac{\mathrm{j}}{4\rho(z_s)} \sum_{m=1}^{\infty} \hat{S}(\omega,z_s)\Psi_m(z_s)\Psi_m(z)\, H_0^{(1)}(k_{rm}r)dz_s \\ &= \sum_{m=1}^{\infty} \left\{ \int_0^{\infty} \frac{\mathrm{j}}{4\rho(z_s)} \hat{S}(\omega,z_s)\Psi_m(z_s)dz_s \right\} \Psi_m(z) H_0^{(1)}(k_{rm}r)\end{aligned}$$

Hence a series of 'modal' amplitude factors $A_m(\omega)$ can be defined:

$$A_m(\omega) = \int_0^{\infty} \frac{\mathrm{j}}{4\rho(z_s)} \hat{S}(\omega,z_s)\Psi_m(z_s)dz_s$$

so that:

$$\hat{p}(r,z) \approx \sum_{m=1}^{\infty} A_m \Psi_m(z)\, H_0^{(1)}(k_{rm}r)$$

These equations have been implemented in the new Aquarius 4.0 model, tentatively assuming that the source factor is dominated by the down-going wave in the pile, i.e. using the expressions from sections 4.1.2 and 4.1.6 for a semi-infinite pile.

## 4.3 A (high-frequency) line source energy flux model (improvement C)

Development of a (high-frequency) line source energy flux model requires deriving analytical expressions of the acoustic energy flux in a shallow water waveguide excited by a line source. Such is pursued, following the approach that Weston [1971,1976] used for point source excitation. This development is of particular interest for evaluating the parameter dependence in the results of the normal mode modelling results. Moreover, the normal mode method becomes less efficient at higher frequencies. The calculation time for the energy flux approach is independent of frequency. A hybrid modelling approach in which the higher frequencies are modelled via an energy flux approach is therefore considered to be a useful extension to a normal mode model for the lower frequencies. A similar hybrid approach has been applied by Özkan Sertlek in his Soprano model [Sertlek, 2016]. This extension has not yet been implemented in Aquarius 4, because the normal mode modelling appeared to be manageable for North Sea piling noise calculations up to the 20 kHz band.

### *4.3.1 Energy flux model for an omnidirectional point source*

The energy flux model for the propagation factor for a point source in a shallow water wave guide is derived by approximating the incoherent sum over the multipath propagation by an integral over the mode angles [Ainslie, 2010, §9.1.1.2.1]. This yields the following expression for the propagation factor:

$$F_p(r) \approx \frac{2}{rH}\int_0^{\theta_c} |R(\theta)|^{2m}\mathrm{d}\theta$$

Where $H$ is the water depth, $\theta$ the grazing angle of plane wave incidence at the sea bed, $\theta_c = \cos^{-1}\left(\frac{c_w}{c_b}\right)$ is the critical angle of incidence and $m = \frac{r\tan\theta_m}{2H}$ the mode number. Substitution of a linear approximation for the angle dependent reflection coefficient of the sea bed $R(\theta) = \exp(-\eta\,\theta)$ and approximating $m \approx \frac{r\theta}{2H}$ yields:

$$F_p(r) \approx \frac{2}{rH}\int_0^{\theta_c} \exp\left(-\frac{\eta\, r}{H}\theta^2\right)\mathrm{d}\theta = \frac{1}{rH}\sqrt{\frac{\pi H}{\eta\, r}}\,\mathrm{erf}\left(\sqrt{\frac{\eta\, r}{H}}\theta_c\right) = \sqrt{\frac{\pi}{\eta\, r^3 H}}\,\mathrm{erf}\left(\sqrt{\frac{\eta\, r}{H}}\theta_c\right)$$

For small arguments ($x \ll 1$): $\mathrm{erf}(x) \approx 2x/\sqrt{\pi}$, and for large arguments ($x \gg 1$): $\mathrm{erf}(x) \approx 1$, so that:

$$F_p(r) \approx \begin{cases} \dfrac{2\theta_c}{rH} & \text{for } \sqrt{\dfrac{\eta\, r}{H}}\theta_c \ll 1 \\ \sqrt{\dfrac{\pi}{\eta\, r^3 H}} & \text{for } \sqrt{\dfrac{\eta\, r}{H}}\theta_c \gg 1 \end{cases}$$

This describes the ‘cylindrical spreading’ ($\mathrm{PL} \propto 10\log\frac{r}{r_{ref}}$) and ‘mode-stripping’ ($\mathrm{PL} \propto 15\log\frac{r}{r_{ref}}$) propagation loss regions [Weston, 1971]. Eventually, as the range increases, one single propagating mode remains, which decays exponentially according to:

$$F_{p,\text{single mode}} \approx \frac{\lambda}{rH^2}\exp\left(-\frac{\eta\lambda^2 r}{4H^3}\right)$$

### 4.3.2 *Energy flux model for a directional source*

The directionality $D(\theta)$ of the sound radiated from a pile a line force can be accounted for in the angle integral for the propagation factor:

$$F_p(r) \approx \frac{2}{rH}\int_0^{\theta_c} D(\theta)\exp\left(-\frac{\eta\, r}{H}\theta^2\right)\mathrm{d}\theta$$

The pressure wave travelling down the pile at a speed of about 5000 m/s radiates it energy mainly at a 'Mach' angle $\theta_M$ of about 17 degrees from the direction normal to the pile. Hence, the idealized directionality is $D(\theta) = \delta(\theta - \theta_M)$ so that:

$$F_p(r) \approx \frac{2}{rH}\int_0^{\theta_c} \delta(\theta - \theta_M)\exp\left(-\frac{\eta\, r}{H}\theta^2\right)\mathrm{d}\theta = \frac{2}{rH}\exp\left(-\frac{\eta\, r}{H}\theta_M^2\right)$$

This solution was proposed in Zampolli et al [2013] and further elaborated in Lippert et al [2018] as 'damped cylindrical spreading'. The corresponding propagation loss is:

$$\begin{aligned}&\mathrm{PL}(r) \approx -10\log_{10}\{F_p(r) r_{ref}^2\}\,\mathrm{dB}\\ &\approx 10\log_{10}\left\{\frac{r}{r_{ref}}\right\}\mathrm{dB} \;+\; 10\log_{10}\left\{\frac{H}{2r_{ref}}\right\}\mathrm{dB} + \left\{\frac{\eta\,\theta_M^2}{H}(10\log_{10}(e)\,\mathrm{dB})\right\} r\end{aligned}$$

This idealized single angle plane wave radiation requires that the pile length is large compared to the acoustic wavelength. In a steered beam approximation for a pile of finite length $H$ (assuming that the pile spans the complete water depth) the directionality is (see Appendix B):

$$D(\theta) \approx \left(\frac{\sin\left((\sin\theta - \sin\theta_M)\frac{k_w H}{2}\right)}{(\sin\theta - \sin\theta_M)\frac{k_w H}{2}}\right)^2$$

Analytical solution of the propagation factor integral including this directionality is beyond the scope of the present study. However, the integral has been solved numerically (for typical parameters $H = 30$ m, $\eta = 0.5$, $\theta_c = 33°$ and $\theta_M = 17°$). The results are shown in Figure 7.

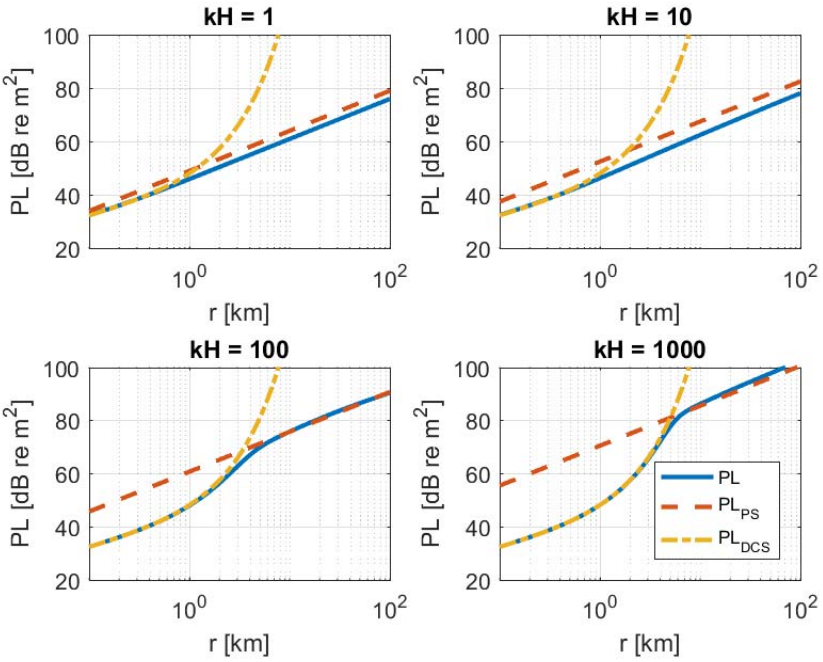


Figure 7 Energy flux propagation loss for a directional pile source (see text) as a function of range in shallow water ($H = 30$ m), for 4 values of the dimensionless frequency $k_w H$. The blue solid line (PL) gives the result of the propagation factor integral. The red dashed line ($\mathrm{PL_{PS}}$) gives the propagation loss trend for an equivalent point source and the yellow dash-dotted line ($\mathrm{PL_{DCS}}$) gives the damped cylindrical spreading loss resulting from Mach-wave radiation, see the equations in the text below this figure.

For large values of $k_w H$ and shorter propagation ranges the propagation factor integral is dominated by the contribution at $\theta = \theta_M$, resulting in a 'damped cylindrical spreading'.

$$\mathrm{PL_{DCS}}(r) \approx 10\log_{10}\left\{\frac{r}{r_{ref}}\right\}\mathrm{dB} \; + \; 10\log_{10}\left\{\frac{H}{2r_{ref}}\right\}\mathrm{dB} + \left\{\frac{\eta\,\theta_M^2}{H}(10\log_{10}(e)\,\mathrm{dB})\right\} r$$

For smaller values of $k_w L$ and at larger ranges, where the propagation loss associated with radiation at the Mach angle is high, the contribution of the low angles dominates. In these cases, the result of the propagation factor integral approaches a 'mode stripping' trend, similar to that for an omni-directional point source. However, the amplitude of the low angle contribution decreases with increasing $k_w H$. The simulations show that this results in an increase of the propagation factor in proportion to $k_w H$, for larger values of $k_w H$. Figure 7 shows that this behaviour appears to be captured reasonably well with the (fitted) approximation

$$\mathrm{PL_{PS}}(r) \approx 15\log_{10}\left\{\frac{r}{r_{ref}}\right\}\mathrm{dB} \; + \; 5\log_{10}\left\{\frac{\eta H}{\pi r_{ref}}\right\}\mathrm{dB} + 10\log_{10}\left\{\frac{1}{2} + \frac{k_w H}{2\pi}\right\}\mathrm{dB}$$

These energy flux expressions can be used to interpret the results of the normal mode calculations, up to the distance where the 'mode stripping' has eliminated the contribution of all waveguide modes except the lowest mode.

## 4.4 Comparison with the Aquarius 2 ‘hybrid’ model

The finite-element (FE) analysis of the pile in the Aquarius 2 model includes the full (axisymmetric) dynamic behaviour of the pile, which is approximated by a one-dimensional line source in Aquarius 4.

We have compared the two models in calculations for the Gemini U8 piling noise for which Aquarius 2 calculations were performed and compared with measurements in [Binnerts et al, 2016]. Both calculations are based on the same (KrakenC) normal mode solution for the sound propagation, but differ in the description of the line source. In Aquarius 2, the excitation of the normal modes is implemented via a modal decomposition of the pressure field in the vicinity of the pile, as calculated by the FE model. This FE model describes the dynamic response of pile and anvil to the hammer force. In Aquarius 4 the one dimensional line source is described in terms of a vertical array of point sources across the water depth with a phase delay according to the downward propagating compressional wave in the pile and a source factor as described In Section 4.1.6. The results of this comparison are shown in Figure 8. Environmental parameters are equal to these used in [Binnerts et al, 2016].

The hammer force (see Chapter 5) has been eliminated in this comparison by subtracting the difference between the calculation results from both models and measurement results at the shortest distance (MP1 at 750 m) from the model predictions at the other three distances.

This shows that the sound propagation predicted by both models is very similar. This implies that the vertical angular distribution predicted by line source model agrees quite well with the FE model. Only at higher frequencies (above ~500 Hz) and at larger distances (MP3 at 32 km and MP4 at 66km) the Aquarius 2 (FE) prediction seems to match somewhat better with the measurement data than the Aquarius 4 (line source). This suggests that the FE results excite the lowest modes (the smallest mode angles) somewhat more efficiently than the simplified line source model. Understanding why would require further investigation (beyond the scope of the current study).

Both models underestimate the broadband SEL at larger distances (32 and 66 km), since their output is nearly at the dominating frequencies, below ~250 Hz.
This is due to an overestimation of the propagation loss at these low frequencies by both models, related with the modelling of the sediment losses (see Chapter 7).

## 4.5 Conclusion

The new line source model included in Aquarius 4 provides a useful and efficient alternative for the more detailed (Aquarius 2) FE modelling of the pile. In contrast with the tentative point source assumption, as applied in the Aquarius 1 and 3 models, it describes the physics of the Mach-wave radiation from the pile.
A first comparison with Aquarius 2 shows that the results agree quite well. The model is particularly useful for modelling large scale North Sea piling scenarios in which the details of individual piling projects are not yet available.

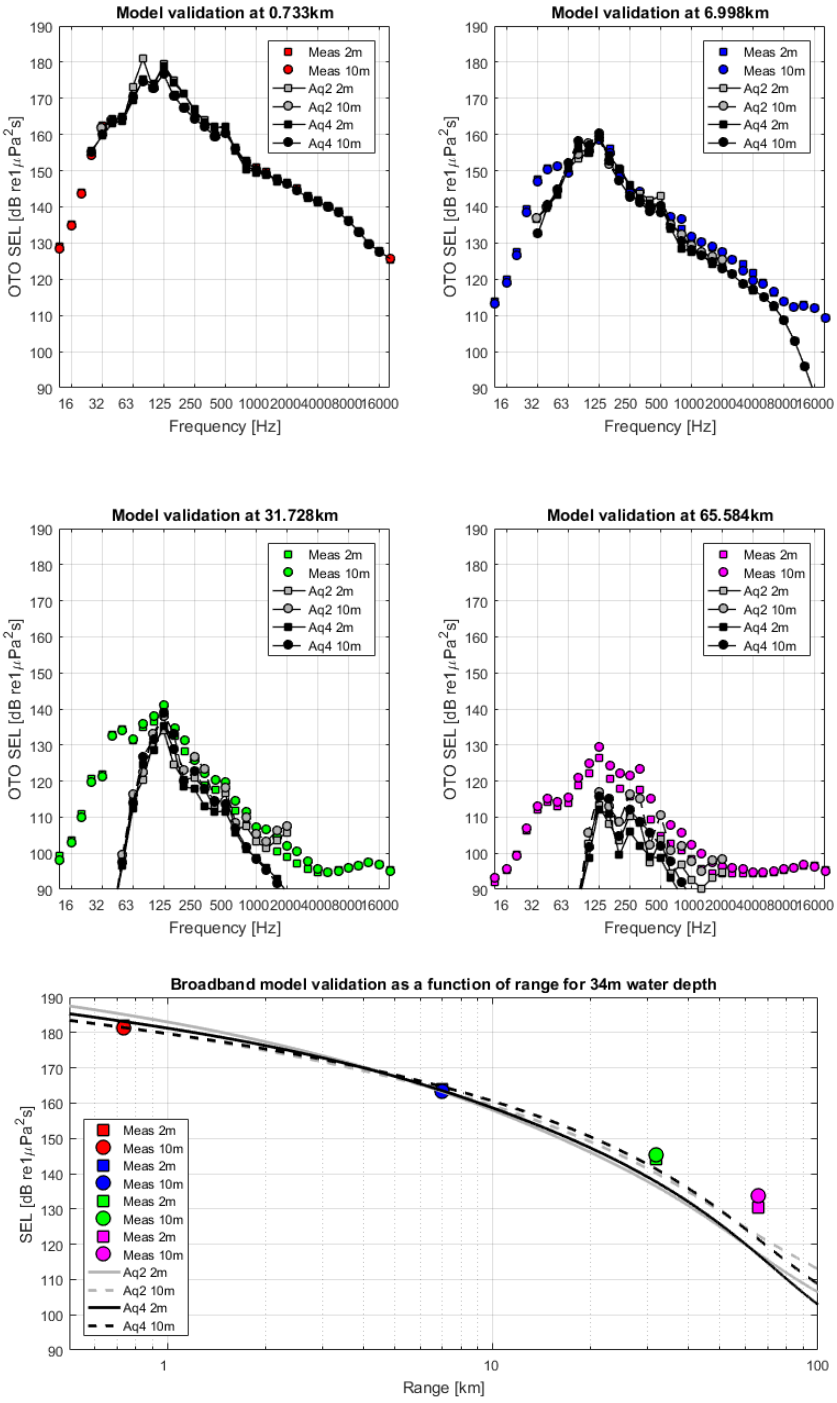


Figure 8 Comparison of Aquarius 4 (line source model) and Aquarius 2 (FE source model) predictions with measurements for the Gemini U8 piling, all predictions scaled to match with the measurement data at the shortest distance (0.733 km). Upper figures: 1/3-octave band spectra of SEL at the four measurement distances. Lower figure: broadband SEL as a function of range. Note that measurement data in the upper part of the frequency range are limited by background noise at 7 km and beyond.

# 5 Model for the hammer force (improvement D)

In the current applications of Aquarius 2, the hammer force excitation spectrum is estimated on the basis of a synthetic pulse description, reconstructed from pile dynamic analysis (PDA) data. These PDA are measured at about 2 m below the piling anvil. The excitation force spectrum is reconstructed via model inversion. Alternatively, the model inversion has also been applied to reconstruct the force spectrum from the measured sound pressure in the water.

A more direct approach would be to use a forward model of the hammer, as used in drivability studies, to calculate the forcing function. A first step in that direction could be an implementation of the analytical hammer model introduced by Deeks and Randolph [1994], as e.g. applied by Fricke & Rolphes [2015].

A Matlab version of such model was made available by Alexander Gavrilov for the COMPILE II workshop. This will be used as a starting point to evaluate the applicability and validity of this approach against available data and FE modelling. Available far-field SEL data will be used to determine the hammer force spectrum via an inversion of the combined line source and propagation models.

More advanced hammer-pile-soil models are implemented in the geotechnical 'WEAP' (Wave Equation Analysis for Piles) software used by the piling industry for drivability studies. WEAP models also include the losses of the acoustic waves in the pile due to interaction with the soil. Trimoreau et al [2014] proposed to run a WEAP code prior to the acoustic FE modelling of the pile, in order to provide the appropriate pile head loading function and pile-soil damping properties.
This approach is promising and being followed by e.g. Heitmann et al [2015] and Kringelum et al [2015]. Implementing such an approach in the Aquarius framework would involve the implementation of a customized WEAP code, which is considered to be outside the scope of the current proposal. It is our expectation that the inclusion of a WEAP model in the Aquarius suite will result in a reduction of the modelling uncertainty, in particular at higher frequencies.

## 5.1 Hammer model

Figure 9 sketches an idealized 'hammer on pile'. The 'ram' impacts on the cushion at an impact velocity $\dot{u}_r$, which corresponds with kinetic energy $E_k = \frac{1}{2} m_r \dot{u}_r^2$.

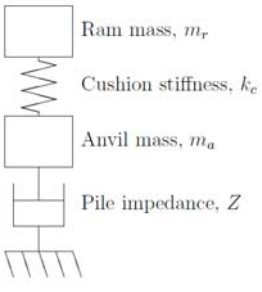


Figure 9 The idealised 'hammer on pile' mechanical system, from [Wood, 2016].

Due to the cushion stiffness, the force $F$ transmitted to the anvil will be:

$$F_a = k_c(u_r - u_a)$$

The force lost by acceleration of the anvil mass is:

$$F_a - F_p = m_a \ddot{u}_a$$

Impedance $Z$ governs the ratio between force and velocity at the top of the pile:

$$F_p = Z\dot{u}_p = Z\dot{u}_a$$

An analytical solution for the equations of motion for the ram-cushion-anvil-pile model shown in Figure 9 is given by Deeks & Randolph [1993]. In the context of the Compile II workshop, a Matlab-implementation of this time domain hammer model was kindly made available by Alexander Gavrilov of Curtin University [Wilkes et al, 2016]. This model has been evaluated and tested, see Appendix A.

The Deeks & Randolph hammer model combined with the one-dimensional pile model (Section 4.1) is considered to be an improvement compared to the previously used empirical point source level, because of its explicit dependence on hammer and pile parameters.

However, this simplified one-dimensional modelling approach has its limitations. Its validity is limited to low frequencies, typically below a few hundreds of Hertz, see e.g. [Fricke & Rolfes, 2015] and [Wilkes & Gavrilov, 2017].

## 5.2 Validation

As an example, this hammer model has been applied to the piling for the Princess Amalia Wind Park (formerly known as 'Q7'). The energy source level spectrum that is used for the Aquarius 1 and 3 models is based on underwater sound measurements at various distances (up to 5 km) from this pile.

The piling of the piles (diameter 4 m, wall thickness 2.5 cm) at Q7 was performed with a Menck MHU 1900S hammer. According to documentation of the BORA expert system [BORA, 2017], the ram mass for this hammer is about 92,000 kg and the mass of the anvil about 46,000 kg. The average hammer blow energy during the measurements was about 800 kJ. No cushion was applied and the anvil stiffness is not known. It was estimated to be about 20 GN/m, because this led to the best match with the measured underwater sound (Figure 11). With these parameters the model yields the time series of the hammer force shown in Figure 10 (left).
This is converted to a one-third octave band spectrum of the force exposure level $L_{E,F} = 10\log_{10}\left\{\int_0^T F^2(t)\mathrm{d}t\,/F_{ref}^2 t_{ref}\right\}$, with $F_{ref} = 1$ N and $t_{ref} = 1$ s, see Figure 10 (right).

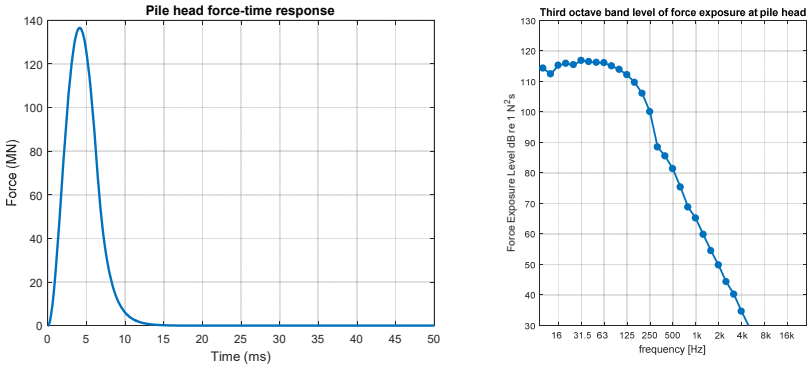


Figure 10 Modelled hammer force for Q7 piling: left: time series, right: one-third octave band (base-10) spectrum of the force exposure level.

This calculated force spectrum has been used to calculate an equivalent energy source level spectrum, see Section 4.1.6, for sound radiation from the complete wet pile length (equal to the water depth, here $H$ =22 m), approximated by the incoherent integral of the source factor:

$$L_{S,E}(\omega) = 10\log_{10}\left(\int_0^H \left|\hat{S}(\omega,z)\right| \mathrm{d}z / 1\ \mu\mathrm{Pa}^2\mathrm{m}^2\mathrm{s}\right)\ \mathrm{dB}$$

The result is shown in Figure 11.

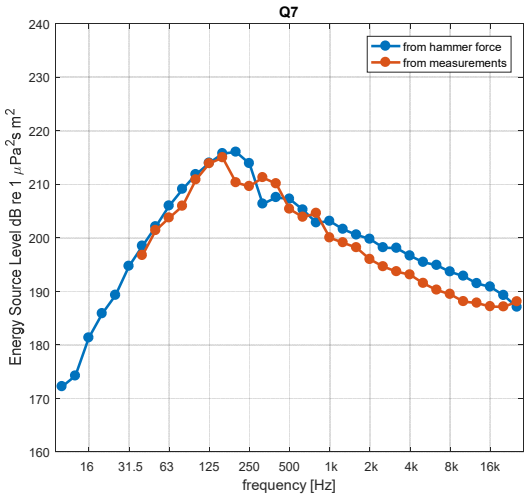


Figure 11 One-third octave band (base-10) spectrum of the energy source level for the Q7 piling: comparison of the spectrum calculated from the modelled hammer force with the spectrum estimated from underwater sound measurements corrected with calculated propagation loss (using the point source model in Aquarius 1).

This shows that the one-dimensional modelling approach for hammer and pile predicts the main characteristics of the measured piling sound. For this case, the level appears to be predicted quite well, particularly for lower frequencies (below 1 kHz). At higher frequencies the model predicts a decreasing source level proportional with $-10\log_{10} f$, while the data suggest a somewhat steeper decrease with increasing frequency.

The accuracy of these predictions is strongly dependent on the accuracy of the available information about pile, hammer and anvil. Such information is generally not available. In an early design stage these details have not yet been decided and also in later stages the information is often hard to obtain due to the commercial sensitivity of the information.
At this stage, we do not have direct access to the relevant details of the IHC S-2000 hammer and the anvil used for the Gemini U8 pile. Table 4 gives the hammer parameters that were taken from a report from the German BORA project [BORA, 2017]. The contact stiffness is a relevant parameter, which is not directly available. The value for the Q7 piling was obtained from a fit to the measured underwater sound (Figure 11). The same value was tentatively used for the Gemini pile.

Table 4 Hammer, anvil and pile parameters for the piles at Q7 and Gemini U8.

| Pile | Hammer | Wet length (m) | Radius (m) | Wall thickness (mm) | Mass anvil (kg) | Mass ram (kg) | Contact stiffness (N/m) | E (kJ) |
|---|---|---|---|---|---|---|---|---|
| **Q7** | Menck MHU 1900S | 25 | 2 | 60 | 46e3 | 92e3 | 20e9 | 800 |
| **U8** | IHC S-2000 | 34 | 2.75 | 80 | 104e3 | 100e3 | 20e9 | 1100 |

Figure 12 shows the calculated equivalent energy source level for the complete wet pile when excited by both hammer blows.

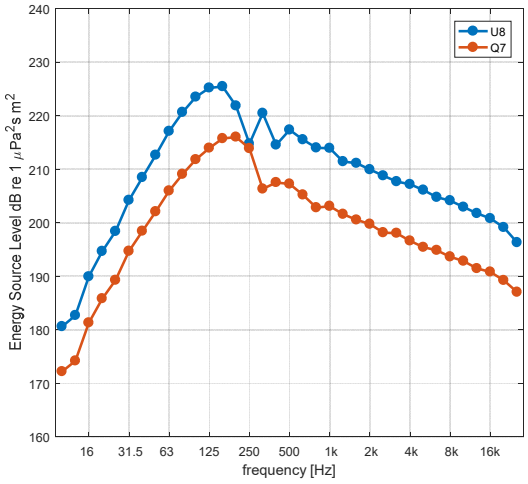


Figure 12 One-third octave band (base-10) spectra of the energy source level for the Q7 and U8 hammer blows, calculated using the Deeks & Randolph hammer model with parameters of Table 4.

The model has the benefit that it can be combined with a line source model and accounts for effects of geometry (water depth and pile diameter) that were not included in the empirical source model (based on Q7 data) used in previous Aquarius studies.

A first assessment of the validity of the updated source model is shown in Figure 13. Environmental parameters are equal to these used in [Binnerts et al, 2016], with zero wind speed.

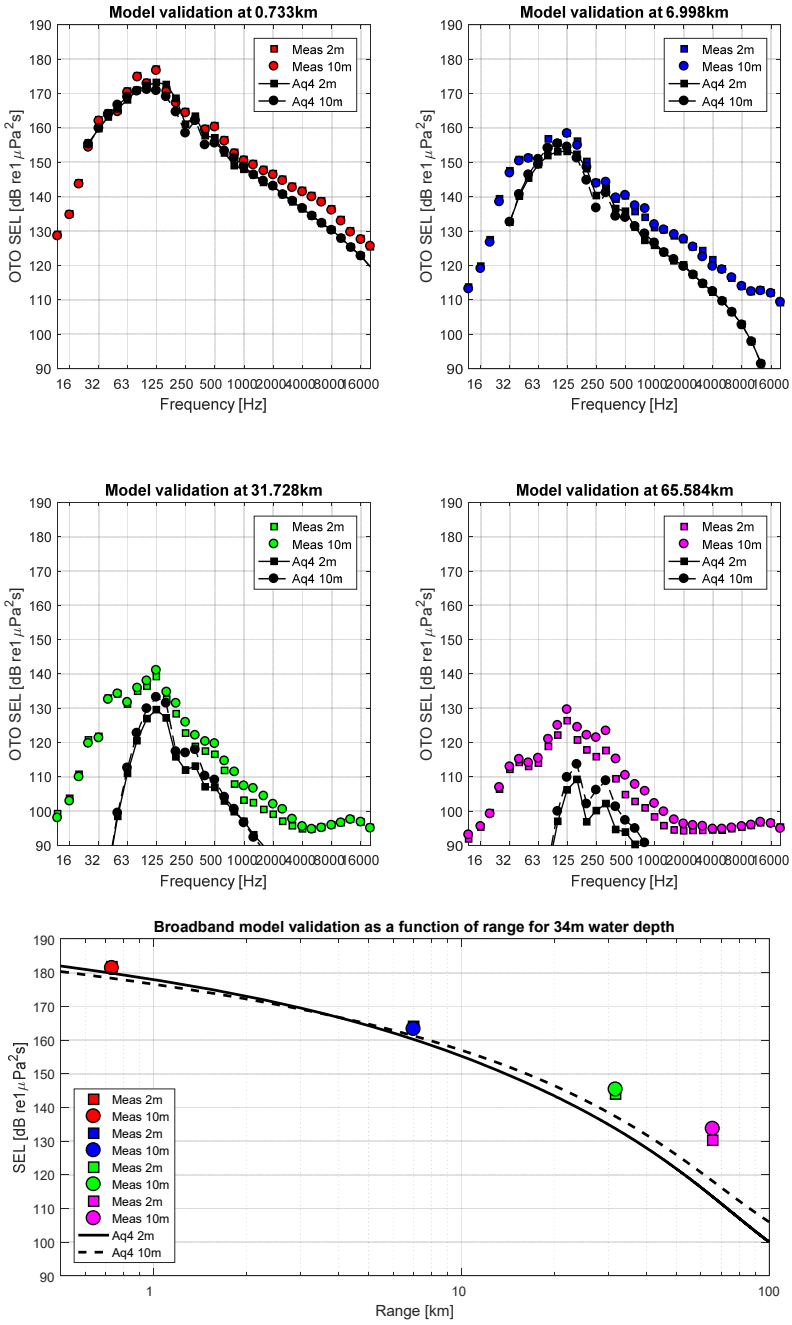


Figure 13 Comparison of predictions with the updated Aquarius 4 line source model including the Deeks model for the hammer force (and zero wind speed) with measurements for the Gemini U8 piling. Upper figures: 1/3-octave band spectra of SEL at the four measurement distances. Lower figure: broadband SEL as a function of range. Note that measurement data in the upper part of the frequency range are limited by background noise at 7 km and beyond.

The agreement between low frequency predictions and measurements at the shortest distance (MP1) illustrates that the Deeks model for the hammer force provides a useful prediction of the force level for the Gemini U8 scenario as well as for the Q7 scenario (compare Figure 11 and Figure 12) at the frequencies (50 Hz to 500 Hz) that dominate the unweighted broadband SEL.

The Deeks hammer model appears to underestimate the force at higher frequencies (>500 Hz). This appears to confirm the suggestions by e.g. [Fricke & Rolfes, 2015] and [Wilkes & Gavrilov, 2017] that the validity of the simplified one-dimensional modelling approach is limited to lower frequencies. Extension of the model to higher frequencies, as suggested by Fricke & Rolfes [2015], could be achieved by means of finite element modelling (beyond the scope of the current study).

The underestimation of the broadband SEL at larger distances (32 and 66 km) is due to an overestimation of the propagation loss, most likely related with the modelling of the sediment losses (see Chapter 7).

# 6 Updated model for wind losses (improvement E)

The losses associated with disturbance of the sea surface by wind are currently included in the Aquarius 1 and 3 models via the semi-empirical low-frequency surface loss model described in Section 8.1.1.2.1 of Ainslie [2010]. It is based on measurement data from Weston and Ching [1989], for the frequencies range between 1 and 4 kHz. This semi-empirical model is currently extrapolated towards lower and higher frequencies. The validity of these extrapolations has not yet been studied, however, the results from [Binnerts et al, 2016] suggest that the predicted dependence of the propagation loss on wind speed is not as clearly observed in the North Sea piling measurement data as predicted by this model.

The ‘Kraken’ solver for the normal mode modelling also contains a semi-empirical wind model. This is globally described in [Porter, 2001]. The approach seems to be invalid in a large angle-frequency regime. This wind model is currently not used in the Aquarius modelling, because we have insufficient confidence in the validity.

The modelling of wind effects has been further investigated. The results of this study are described in Appendix C and show that the effects of rough sea-surfaces on sound propagating underwater remains an area of considerable uncertainty.

Appendix C describes an attempt to combine the two semi-empirical expressions for surface loss, applicable for 1-4 kHz and above 10 kHz respectively, into a consistent equation that avoids step-changes in behavior or predictions that defy ‘common sense’. It cannot yet be said to produce a validated surface model. Nevertheless, this study has led to an updated and implemented surface loss model that avoids unwanted effects from extrapolation of the semi-empirical models beyond their range of validity. In particular, the previous Aquarius implementation of the Weston and Ching surface loss model appeared to overestimate the surface losses at low frequencies (below 1 kHz) for higher wind speeds. A weighting function has been included that smoothly removes the effect of the sea surface for high windspeeds at frequencies below a minimum frequency at which the rough sea surface is likely to be acoustically significant.

Figure 14 shows the effect of the Weston and Ching surface loss model on the computed SEL for the Gemini U8 scenario. It has been implemented as described in Appendix C, though the extension to the APL model at frequencies above 10 kHz has not yet been implemented for lack of time in the current project and because the focus was on the lower frequencies which dominate the broadband SEL.) The results of the predictions with wind (8.8 m/s) are compared with the results without wind, from Figure 13.

This shows that the low frequency weighting function indeed removes the effect of wind at lower frequencies. Consequently, no effects of the wind model are observed in the unweighted broadband SELs, which are dominated by these lower frequencies.

At higher frequencies the modelled effect of wind losses appears to increase the deviation between measurements and model predictions. This suggests that the wind model overestimates the wind related propagations loss, though it cannot be

excluded from these measurements at a single wind speed that the overestimated propagation loss is due to other discrepancies in the modelling, like the description of the sediment (next chapter).

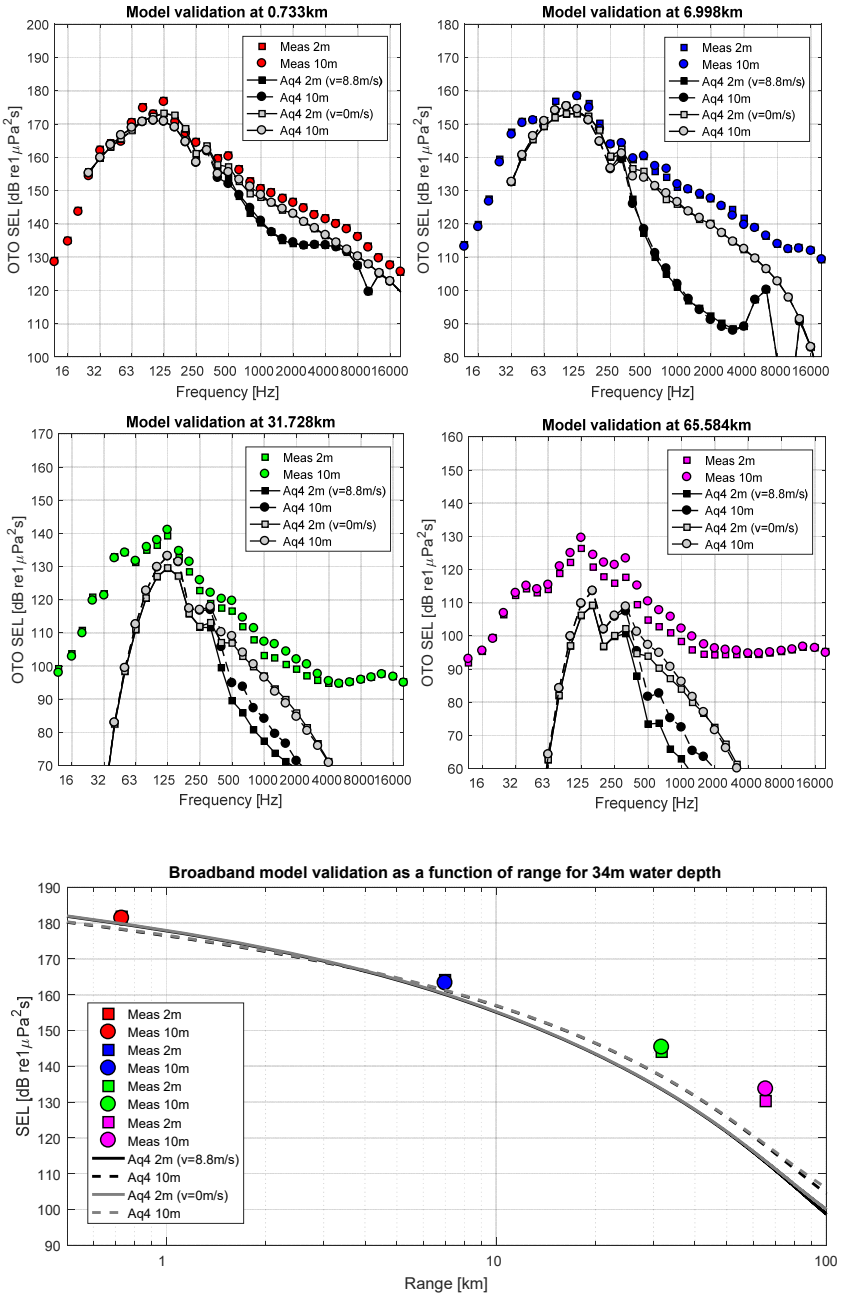


Figure 14 Comparison of predictions with the updated Aquarius 4 line source model including the Deeks model for the hammer force and the updated Weston & Ching model for the effects of wind (wind speed 8.8 m/s) with measurements for the Gemini U8 piling. Upper figures: 1/3-octave band spectra of SEL at the four measurement distances. Lower figure: broadband SEL as a function of range. Note that measurement data in the upper part of the frequency range are limited by background noise at 7 km and beyond.

Figure 14 shows that the difference between model predictions with and without wind losses reduces at the larger distances. This effect is likely related to the dependence of the wind losses model on grazing angle. At shorter ranges the effect of wind in the model is larger because most of the acoustic energy travels at a relatively large grazing angle of ~17 degrees, while at larger distances the acoustic field is dominated characterized by modes with smaller grazing angles, for which the effect of the wind on the reflection loss is smaller.

**Conclusions:**

- Although there is empirical evidence in literature that wind has an effect of sound propagation at higher frequencies due to scattering and absorption by bubbles at the water surface [Ainslie, 2005], the propagation loss predicted by including the Weston and Ching model (as described in Appendix C) in the normal mode based Aquarius 4 model seems to overestimate the effects of wind as observed in the North Sea piling noise measurements.
- Although this effect does not affect the broadband predictions, it would become a critical aspect of the model when one is interested in frequencies > 500 Hz.
- The effects of rough sea-surfaces on sound propagating underwater remains an area of considerable uncertainty. Further progress in modelling these effects would probably require large scale investigations and data gathering, far beyond the scope of the current model development. Until more reliable models and data become available, it is recommended to ignore the wind effects in Aquarius 4 calculations for future impact assessment studies. This would avoid the risk of an undesirable underestimation of the high frequency content of the received SEL.

# 7 Updated model for sediment losses (improvement F)

## 7.1 Introduction

As suggested in [Binnerts et al, 2016] and in the previous chapters, the deviations between measurement results and Aquarius predictions at low frequency can be reduced by improving the geoacoustic model and parameters used by Aquarius. The present sediment model is an infinitely thick uniform sediment layer, the properties of which are taken from Table 4.18 from Ainslie [2010], which is based on the correlations of Bachman [1985]. These are applicable to intermediate acoustic frequencies approximately in the range 1kHz to 10 kHz. Below this frequency the properties of sand are known to vary with frequency [Kibblewhite,1989], [Williams, 2001 & 2013], [Zhou et al, 2009], as illustrated by Figure 15 for attenuation.

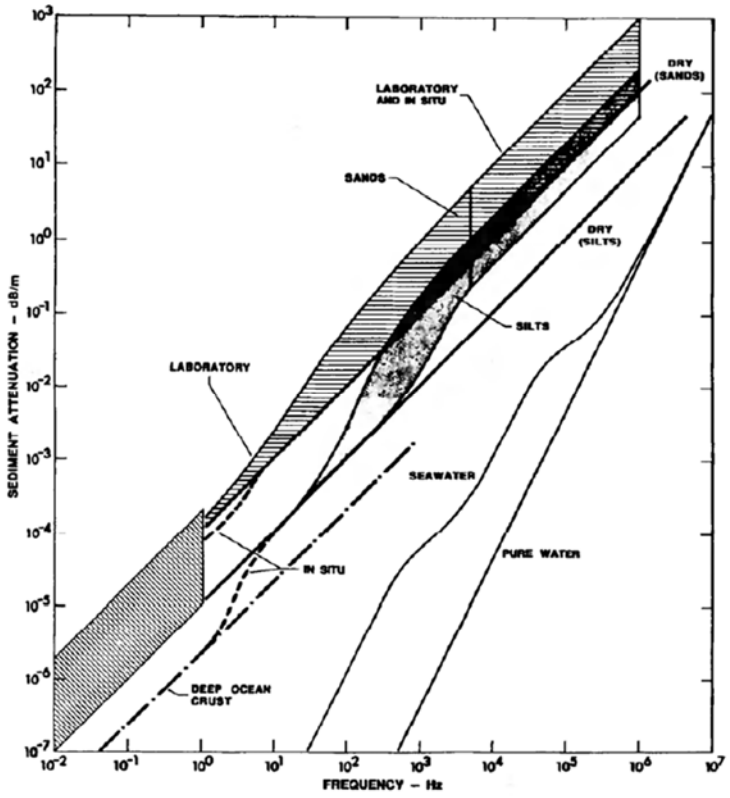


Figure 15: Summary of attenuation coefficient, α, (in dB/m) vs frequency, f, (in Hz) for different sediment types. Reproduced from Kibblewhite [1989].

Hamilton [1980] parametrizes the frequency dependence of the attenuation coefficient, $\alpha$, in terms of the attenuation parameter, $k$, in the form $\alpha(f) = kf$. If $k$ is a constant, $\alpha(f)$ is a straight line on a log-log plot. It can be seen in Figure 15 that data suggest that $k$ is locally constant but takes different constant values in different regions of the graph. In the transitions between the regions $k$ is frequency dependent. It is often assumed that this behaviour can approximately be

expressed by an empirical form of a power law $\alpha(f) \propto f^n$, with values of $n$ roughly between 0.5 and 2, see e.g. Kibblewhite [1989].

The value of $k$ also varies with grain size, as illustrated by Figure 16 for the case $n = 1$. See Ainslie [2010] for an explanation of grain size. Sand sediments have grain sizes in the range 0-4 $\phi$ which means that $k$ is in the range 0.2-0.7 dB/(m kHz), corresponding to the high frequency limit of Figure 15.

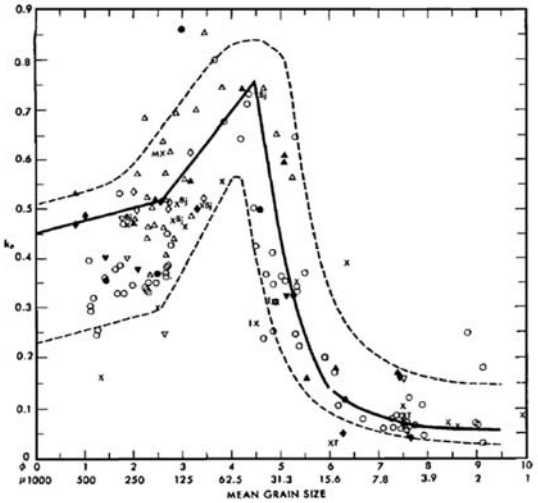


FIG. 19. Surface-sediment mean grain size versus attenuation of compressional waves (expressed as $k_\beta$, defined in Fig. 18). The symbols and lines are as indicated in Fig. 18. For additional information and regression equations see Hamilton.[55]

Figure 16: Summary of attenuation parameter $k$ (in dB/(m kHz)) vs grain size (in $\phi$). Reproduced from Hamilton [1980].

The properties of sand are also known to vary with depth in the sediment, with the sound speed and attenuation coefficient increasing and decreasing, respectively, with increasing depth, see for example the data from [Hamilton, 1980] reproduced in Figure 17.

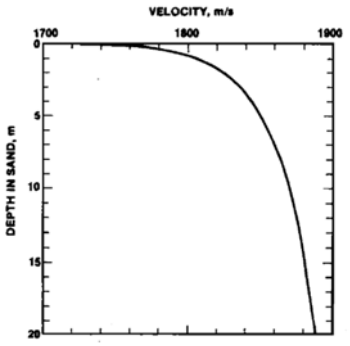


FIG. 7. Compressional wave (sound) velocity versus depth in fine sand. Curve computed from laboratory measurements (see Hamilton[21] for discussion). See Table IV for regression equation.

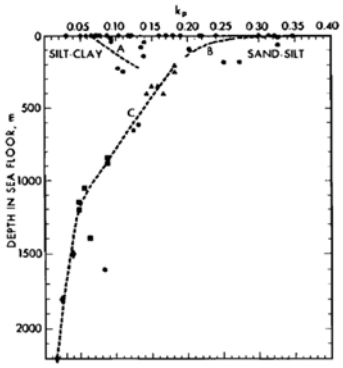


FIG. 20. Attenuation of compressional waves (expressed as $k_\beta$, defined in Fig. 18) versus depth in the sea floor, or in sedimentary strata. For discussion of symbols and curves see Hamilton.[56] Symbols: circles—measurements from the literature; triangles—squares, and diamonds represent the first, second, and third layers, respectively, in the sea floor in seven areas (from Neprochnov[65]).

Figure 17: Left: Sound speed vs depth in fine sand (deep sea sediment). Right: Attenuation parameter (in dB/(m kHz)) vs depth (in m) for different sediment types. Figures reproduced from Hamilton [1980].

The effects of dispersion (i.e. frequency dependence of sound speed and attenuation factor $k$) and layering are considered in the following sections.

The effect of non-zero shear speed of sand has a small effect on reflection loss (see Figure 8.4 of [Ainslie, 2010]) unless the sediment layer is very thin, which is not the case in the Dutch part of the North Sea. The effects of sediment shear are therefore not considered further.

The roughness of the water-sediment boundary has an important effect on reflection loss at high frequency [APL, 1994]. Since we focus on frequencies, for which the acoustic wavelength is large compared with the sediment roughness, the roughness is not considered further.

## 7.2 Dispersion

Zhou et al [2009] have analysed and summarized a large set of data for frequency dependent sound speed and attenuation derived from long-range acoustic measurements conducted at 20 locations in different coastal zones around the world (mainly Asia and the US, plus a location in the Mediterranean Sea).
This provides a reference data set for sandy bottoms in the 50 Hz –400 kHz range. The data are reproduced in Figure 18. We are not aware of similar data for the North Sea, but see no direct reason to believe that the North Sea sediment properties are very different from these data.

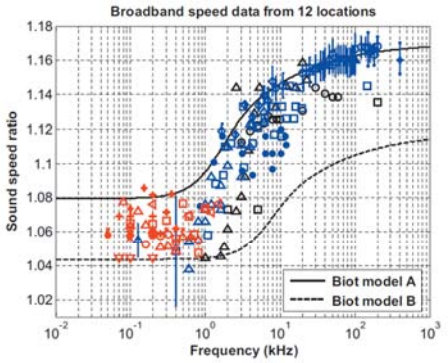


FIG. 12. Broadband sound speed ratio in sandy seabottoms, and data/model comparison. Blue with and without uncertainty bars: SAX99 data (Ref. 19) and SAX04 (Ref. 66); other colors: LF-field-derived data from seven locations of this paper; black: from mid-frequency to HF direct measurements (see text for details). The Biot parameters for models *A* and model *B* are listed in Table X.

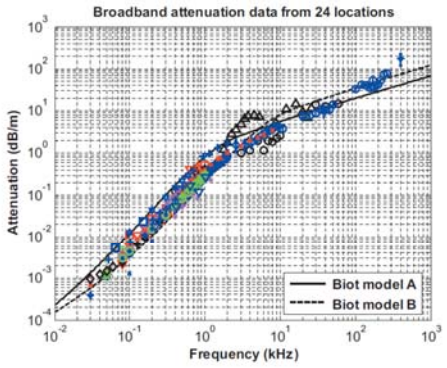


FIG. 13. Broadband sound attenuation in sandy seabottoms, and data/model comparison. Blue with uncertainty bars: SAX99 data (Ref. 19); other colors: LF-field-inverted data from 20 locations; black: from mid-frequency to HF direct measurements (see text for details). The Biot parameters for models *A* and *B* are listed in Table X.

Figure 18: Sound speed ratio (left) and attenuation coefficient (dB/m) (right) vs frequency (kHz) in sand sediments. Of particular interest is the inflexion centred around 5 kHz, suggesting dispersion around this frequency. Reproduced from [Zhou et al, 2009].

Zhou et al [2009] concluded that:

- The average sound speed ratio at the bottom-water interface in the 50–600 Hz range is $\frac{c_s}{c_w} = 1.061 \pm 0.009$.
- The effective sound attenuation in the 50–1000 Hz range can be expressed by $\alpha\ (\mathrm{dB/m}) = (0.37 \pm 0.01)\left(\frac{f}{1000\ \mathrm{Hz}}\right)^{1.80\pm0.02}$.

- Both the LF-field-derived sound speed and attenuation can be well described by the Biot–Stoll model with parameters that are consistent with either theoretical considerations or experimental measurements.

The three most important parameters in the Biot model for coarse granular sediments are the permeability $\kappa$, the porosity $\beta$ and the tortuosity $\alpha_t$. Table 5 gives the parameter values that were selected for the 'Biot model A' and 'Biot model B' curves in Figure 18.

Williams [2001&2013] proposed an 'effective density fluid model' (EDFM) and demonstrated that it is for many applications an accurate alternative to full Biot theory and much simpler to implement.

Table 5 Selected Biot model parameters from [Zhou et al, 2009], used for the curves in Figure 18, and from [Williams, 2013].

| | Biot model A | Biot model B | Williams 2013 |
|---|---|---|---|
| permeability $\kappa$ [m$^2$] | $2.3\times10^{-11}$ | $0.5\times10^{-11}$ | $1.0\times10^{-11}$ |
| porosity $X_f$ [-] | 0.39 | 0.45 | 0.394 |
| tortuosity $\alpha_t$ [-] | 1.25 | 1.45 | 1.2 |
| fluid density $\rho_w$ [kg/m$^3$] | 1023 | 1023 | 1023 |
| fluid bulk modulus $K_w$ [Pa] | $2.395\times10^9$ | $2.395\times10^9$ | $2.395\times10^9$ |
| fluid sound speed $c_w$ [m/s] | 1530 | 1530 | 1530 |
| fluid viscosity $\eta$ [kg/ms] | 0.00105 | 0.00105 | 0.00105 |
| grain density $\rho_s$ [kg/m$^3$] | 2690 | 2690 | 2664 |
| grain bulk modulus $K_s$ [Pa] | $3.2\times10^{10}$ | $3.2\times10^{10}$ | $3.2\times10^{10}$ |
| frame bulk modulus $K_0$ [Pa] | $4.23\times10^7$ | $4.36\times10^7$ | $4.36\times10^7$ |

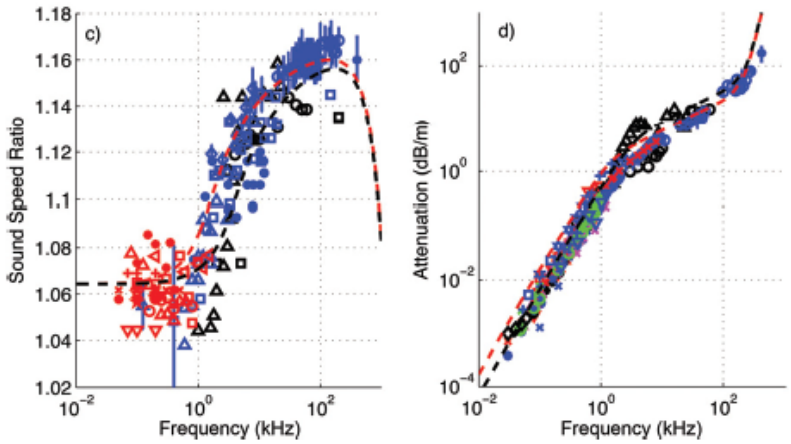


Figure 19: Sound speed ratio (left) and attenuation coefficient (dB/m) (right) vs frequency (kHz) in sand sediments. Reproduced from [Williams, 2013]. Data points from [Zhou et al, 2009], as shown in Figure 18, compared with lines calculated by the EDFM with thermal conductivity and multiple scattering, using parameters given in Table 5 (black curve) and higher value for the permeability parameter $\kappa = 2.5 \times 10^{-11}$ m$^2$ (red curve).

We have implemented the EDFM [Williams 2013] in a Matlab program that calculates the effective density of the sediment, the ratio of the effective sound speed in the sediment to the sound speed in the water (above the sea bottom) and the attenuation in the sediment as a function of sediment parameters (see Table 5). Figure 20 to Figure 22 show the calculated effect of the three most relevant sediment parameters: porosity, permeability and tortuosity on the results.

These simulation results demonstrate that the EDFM predicts that:

- *porosity* has a strong effect on sound speed ratio over the complete frequency range and on low frequency attenuation;
- *permeability* mainly affects low frequency attenuation;
- *tortuosity* has a smaller effect than porosity and permeability and only affects the higher frequencies;
- low frequency attenuation per wavelength increases linearly with frequency
- high frequency attenuation per wavelength decreases in proportion to the frequency to the power -0.5.

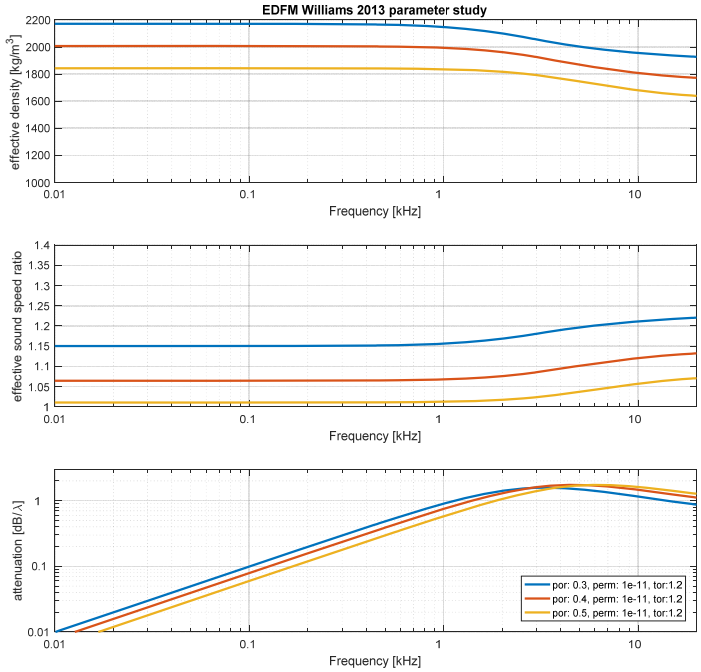


Figure 20: Effective sediment density (top), sound speed ratio (middle) and attenuation coefficient (lower) vs frequency (kHz), calculated by the EDFM [Williams, 2013], for sediment **porosity** between 0.3 and 0.5.

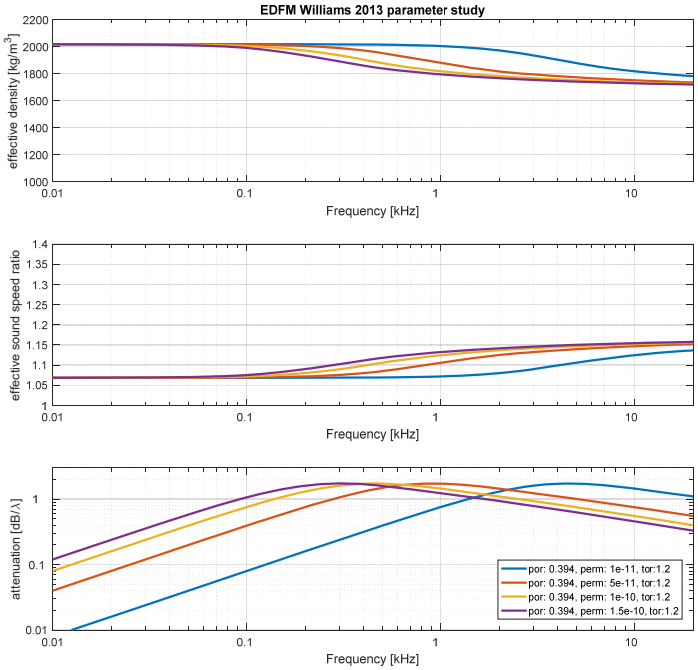


Figure 21: Effective sediment density (top), sound speed ratio (middle) and attenuation coefficient (lower) vs frequency (kHz), calculated by the EDFM [Williams, 2013], for sediment **permeability** between $1.0\times10^{-11}$ m$^2$ and $1.5\times10^{-10}$ m$^2$.

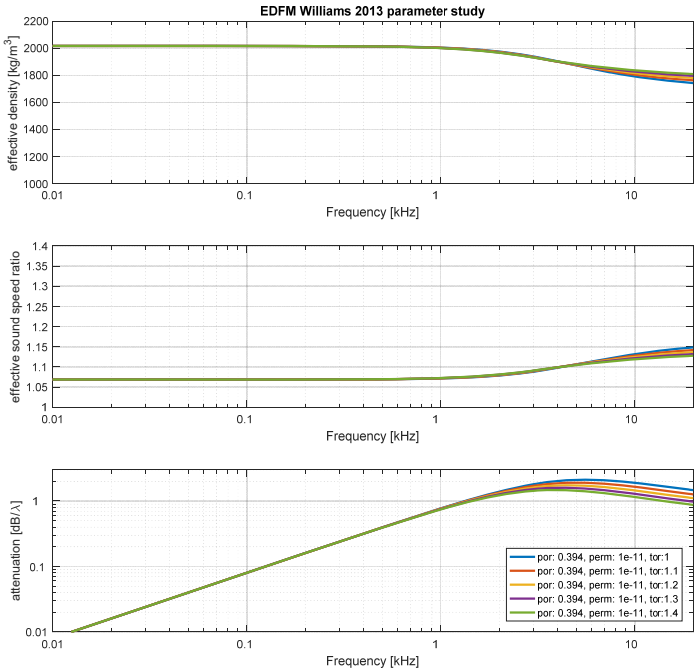


Figure 22: Effective sediment density (top), sound speed ratio (middle) and attenuation coefficient (lower) vs frequency (kHz), calculated by the EDFM [Williams, 2013], for sediment **tortuosity** between 1.0 and 1.4.

In previous Aquarius studies for sound propagation at the North Sea we have used the ‘medium sand’ values from Table 4.18 from [Ainslie, 2010] to characterize the sediment properties. According to that table (applicable to frequencies between 1 and 10 kHz), the (frequency-independent) sound speed ratio for medium sand is about 1.2 and the attenuation per wavelength about 0.88 dB. The corresponding porosity is about 0.3, hence lower than the values estimated for the data reported by Zhou et al [2009], where porosity was estimated at about 0.4. The choice for using these constant ‘medium sand’ parameters was based on TNO’s experience with naval sonar performance modelling, with emphasis on frequencies above ~1 kHz range, but also because of a lack of appropriate available data for the North Sea.

Due to the uncertainty associated with the detailed parameters for the Biot and EDFM models, we are not confident that we are ready to use these models for the North Sea environment in the Aquarius toolbox. Nevertheless, the literature survey provides sufficient evidence to include some form of empirical dispersion correction in the sediment properties towards the lower frequencies (e.g. below 1 kHz).

## 7.3 Depth dependence and layering

Zhou et al [2009] note that most of the inverted low-frequency data for sound speed and attenuation were obtained from long-range acoustic field data for which the surficial sediment layer with a thickness on the order of a few wavelengths plays the dominant role. Thus, the bottom sound speed and attenuation values as well as the Biot parameter values should be interpreted as “averaged” values in the effective medium of the top layer of the sandy bottom.

The speed of sound in sand is known to increase with increasing pressure (Figure 17) but the relatively high sound speed in sand relative to that of silt or clay makes the effect of a sound speed gradient less important, making any effect correspondingly difficult to measure. However, the dispersion described in §7.2 results in a lower sound speed in the upper sediment layers than might be expected from high frequency measurements, potentially making the layering important at low frequency.

Dahl & Choi [2006] present an analysis of low frequency (140-420 Hz) geoacoustic measurements in shallow water with a silty (very fine) sand (mean grain size 3-4 $\phi$) bottom. The data are from short-range (<1 km) propagation measurements in the Yellow Sea at a water depth of about 75 m. Using travel time analysis involving the precursor arrival and the first-arriving water-borne ray, the sound speed just below the water-sediment interface was estimated to be 1573 m/s, with a gradient of 1.1 (m/s)/m. Their estimation of the sound speed in the water above the sea bed is 1480 m/s, hence the surface sound speed ratio is 1.06, which is close to the average value for sandy sediments reported by Zhou et al [2009]. In the 150–420 Hz frequency range, the wavelength decreases from about 10 m to 4 m. From the energy spectrum of the precursor arrival, the sediment compressional wave attenuation was estimated to be 0.08 dB/m/kHz over the frequency range 150–420 Hz. Hence they suggest a linear dependence $\alpha(f) = kf$ in this frequency range. At 150 Hz the attenuation is 0.012, and agrees with the $\alpha(f) = 0.37f^{1.8}$ trend found by Zhou et al [2009]. At 420 Hz the attenuation coefficient found by Dahl & Choi [2006] is 0.034, while the Zhou et al [2009] trend predicts 0.078.

To investigate the effect of the sound speed gradient, we have used a previously developed Matlab code for calculating the reflection loss at a multi-layered bottom as a function of frequency and grazing angle. This code implements the theory described in Ainslie [1995].

The sound speed gradient was approximated by a large number of layers, with depth-dependent sediment properties linearly interpolated between selected values from Table 4.18 from Ainslie [2010], here reproduced in Table 6.

Table 6 selected sediment geo-acoustic parameters from Table 4.18 from [Ainslie, 2010], applicable for the frequency range 1 to 10 kHz.

| sediment | grain size $M$ [ϕ] | sound speed ratio $c_s/c_w$ | density ratio $\rho_s/\rho_w$ | attenuation coefficient $\beta$ [dB/$\lambda$] | porosity $X_f$ |
|---|---|---|---|---|---|
| Very coarse sand | -0.5 | 1.3067 | 2.401 | 0.89 | 0.13 |
| Medium sand | 1.5 | 1.1978 | 2.086 | 0.88 | 0.32 |
| Fine sand | 2.5 | 1.1522 | 1.945 | 0.89 | 0.41 |

Figure 24 and Figure 25 show the calculated propagation loss due to sediment loss in a shallow water waveguide of 34 m depth, for various frequencies and distances.

Note that the modelled sound speed gradients are more than an order of magnitude larger than the gradient found by Dahl & Choi [2006]. To evaluate the effect of the reflection loss per bottom bounce on long range propagation loss, it is multiplied by the number of bottom bounces, which depends on grazing angle and distance (and water depth). Figure 23 gives an example calculation of the number of bottom bounces for a water depth of 34 m (which is the local water depth at the Gemini U8 pile).

Comparison of the solid lines (for a uniform sediment) and the dashed lines (for a sediment with a linear sound speed gradient over the upper 10 m of the sediment) shows that the gradient causes a frequency-dependent reduction of the propagation loss. However, the frequency-dependent reduction associated with the dispersion in the porous sediment (as described in Section 7.2 and represented by the dash-dotted lines in Figure 25) is an order of magnitude larger. This suggests that (at least for the parameter values chosen for this comparison) modelling the sediment as a fluid half-space with frequency-dependent sediment properties should provide a reasonable approximation. That would mean the additional complexity (and the increased calculation time) of incorporate layering of the sediment in the normal mode model can be avoided.

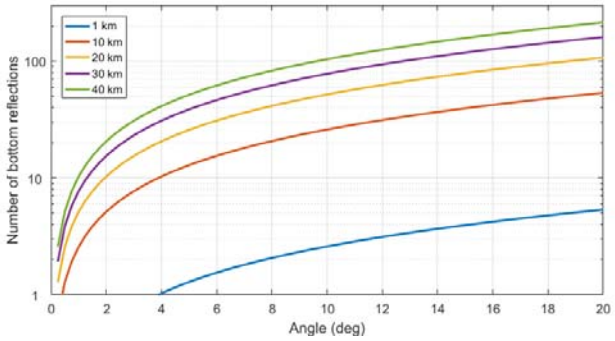


Figure 23: Number of bottom reflections as a function of grazing angle, for sound propagation to various distances in a shallow water waveguide of 34 m depth.

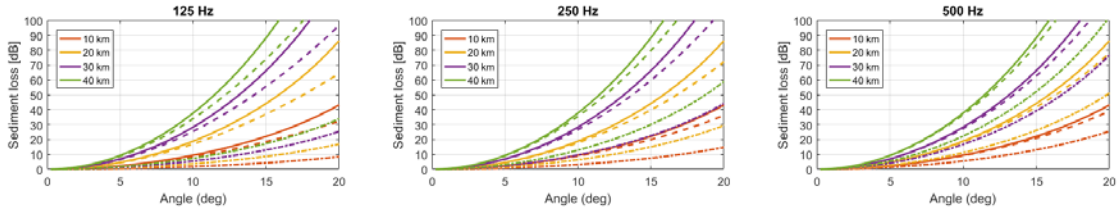


Figure 24: Propagation loss over 10 to 40 km distance due to interactions with the sediment in a shallow water waveguide of 34 m depth, for a sediment with the properties of 'fine sand' (Table 6) at the surface. The corresponding gradient of the sound speed ratio is 23 (m/s)/m. Solid lines are for a uniform 'fine sand' sediment without gradient or layering. Dashed lines are for a linear gradient in the sediment properties between 'fine sand' at the surface and 'very coarse sand' at 10 m depth (and below). The dash-dotted lines are for a uniform 'fine sand' sediment in which the absorption follows a $f^{1.8}$-trend at frequencies below 1600 Hz [Zhou et al, 2009].

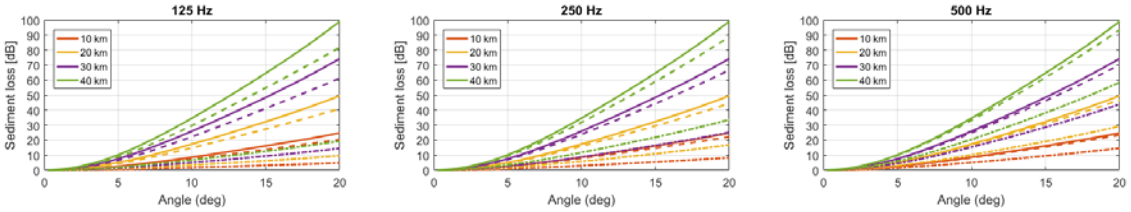


Figure 25: Propagation loss over 10 to 40 km distance due to interactions with the sediment in a shallow water waveguide of 34 m depth, for a sediment with the properties of 'medium sand' (Table 6) at the surface. The corresponding gradient of the sound speed ratio is 16 (m/s)/m. See the caption of Figure 24 for a description of the different lines.

## 7.4 North Sea geoacoustic model

Development of a proper and validated geoacoustic model for the North Sea is beyond the scope of the current study. Nevertheless, it was concluded from the Aquarius validation study [Binnerts et al, 2016] that the bias in the prediction of long range broadband SEL generated by marine piling is strongly related with uncertainty in the description of the sediment properties. Hence, including some form of frequency dependence in the sediment parameters is considered necessary to reduce this observed bias. However, at this stage we can only propose parameter values based on the piling noise data, for which we focus on the Gemini U8 measurements [Binnerts et al, 2016]. Characterization of North Sea sediment

acoustical properties, particularly at lower frequencies, is becoming more relevant, due to the increasing interest in environmental effects of anthropogenic sound. Hence, further research in this field is highly recommended.

For the Aquarius 4 modelling we have evaluated four options. Figure 26 shows the four different options that were considered in the modelling of the dispersion in the sediment parameters (from left to right density, sound speed ratio and attenuation). The coloured lines corresponds to the tabulated values from table 4.18 [Ainslie, 2010], for 'medium' and 'coarse' sand, with a correction for a decreasing absorption towards lower frequencies, in proportion with $f^{1.8}$ [Zhou et al 2009] at frequencies below 250 Hz. This transition frequency was obtain from a parameter fit that gave the best agreement between the Aquarius 4 model predictions and the U8 data at these low frequencies. As an alternative, the Williams [2013] model curves where obtained by choosing the porosity and tortuosity values such that the same sound speed ratio and damping values was obtained at 1 kHz, for the two sediment types.

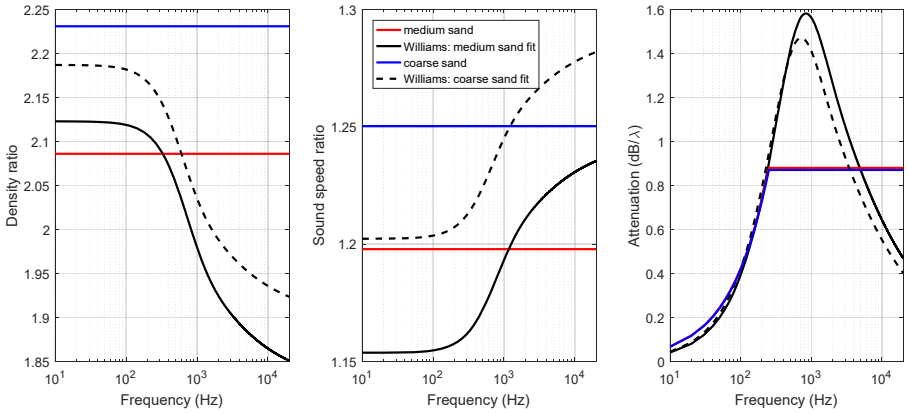


Figure 26: from left to right updated frequency dependent parameters for the density ratio, sound speed ratio and attenuation. The coloured lines describe the values as tabulated in table 4.18 in [Ainslie, 2010], except for the attenuation below 250 Hz, where a $f^{1.8}$ power law, as suggested by Zhou et al [2009], is used to obtain a better agreement with the Gemini U8 piling measurement results at the lower frequencies. The black lines describe the parameters calculated by the Williams [2013] model, where the porosity was tuned to obtain an agreement with the sound speed ratio at 1 kHz, which is the outer limit of validity according to [Ainslie, 2010].

Figure 28 shows the result of applying the updated 'coarse' and 'medium' sand properties with a reduced absorption towards low frequencies in the Aquarius 4 predictions for the Gemini U8 piling. Figure 28 shows the results when applying the Williams [2013] model for 'medium sand'.

The updated sediment modelling provides a much better agreement with the measurements at low frequencies (< 250 Hz), and consequently for the unweighted broadband SEL. However, the levels at large distances and higher frequencies are underestimated, which will result in a bias in the predicted levels when a weighting for the hearing sensitivity of harbour porpoises is applied or the frequency dependent transmission loss from mitigation measures (Chapter 8).

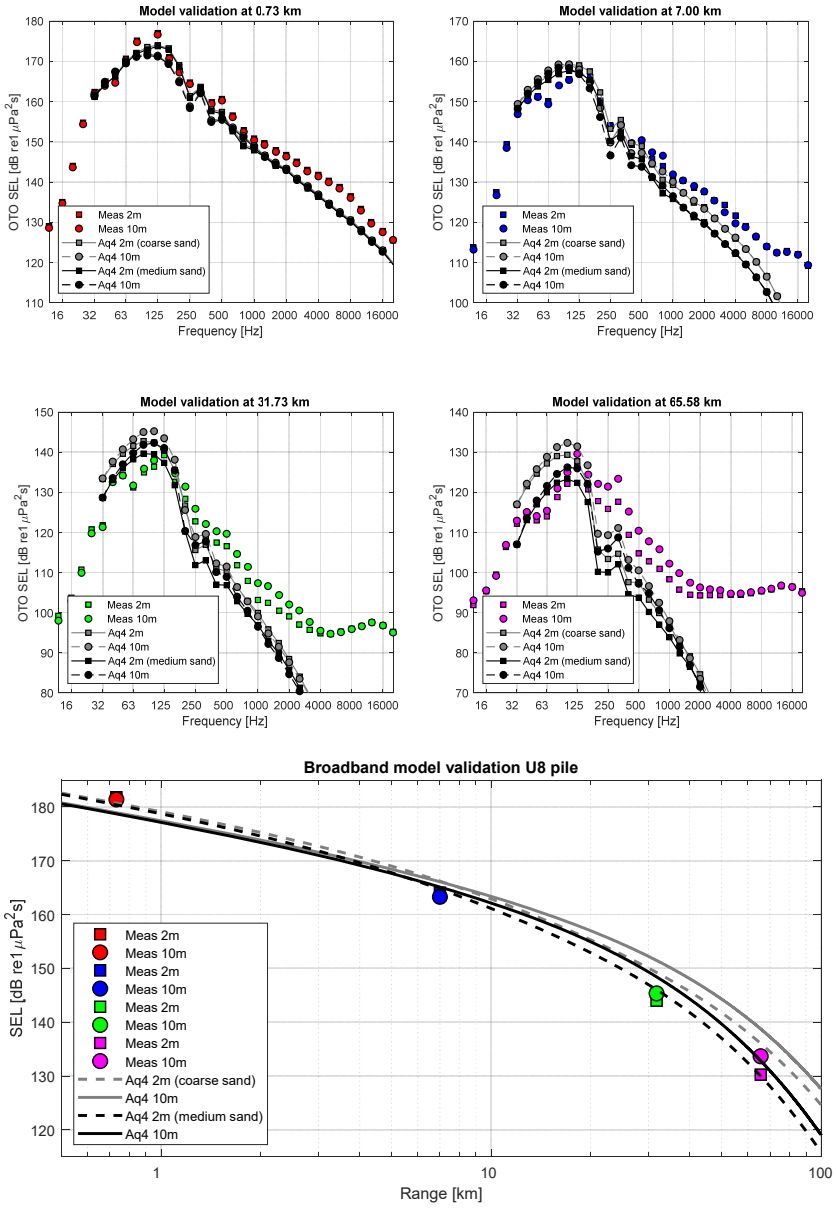


Figure 27 Comparison of predictions with the updated Aquarius 4 line source model including the Deeks model for the hammer force, for wind speed 0 m/s, and 'medium' and 'coarse' sand sediment parameters (attenuation trend $f^{1.8}$ below 250 Hz) with measurements for the Gemini U8 piling. Upper figures: 1/3-octave band spectra of SEL at the four measurement distances. Lower figure: broadband SEL as a function of range. Note that measurement data in the upper part of the frequency range are limited by background noise at 7 km and beyond.

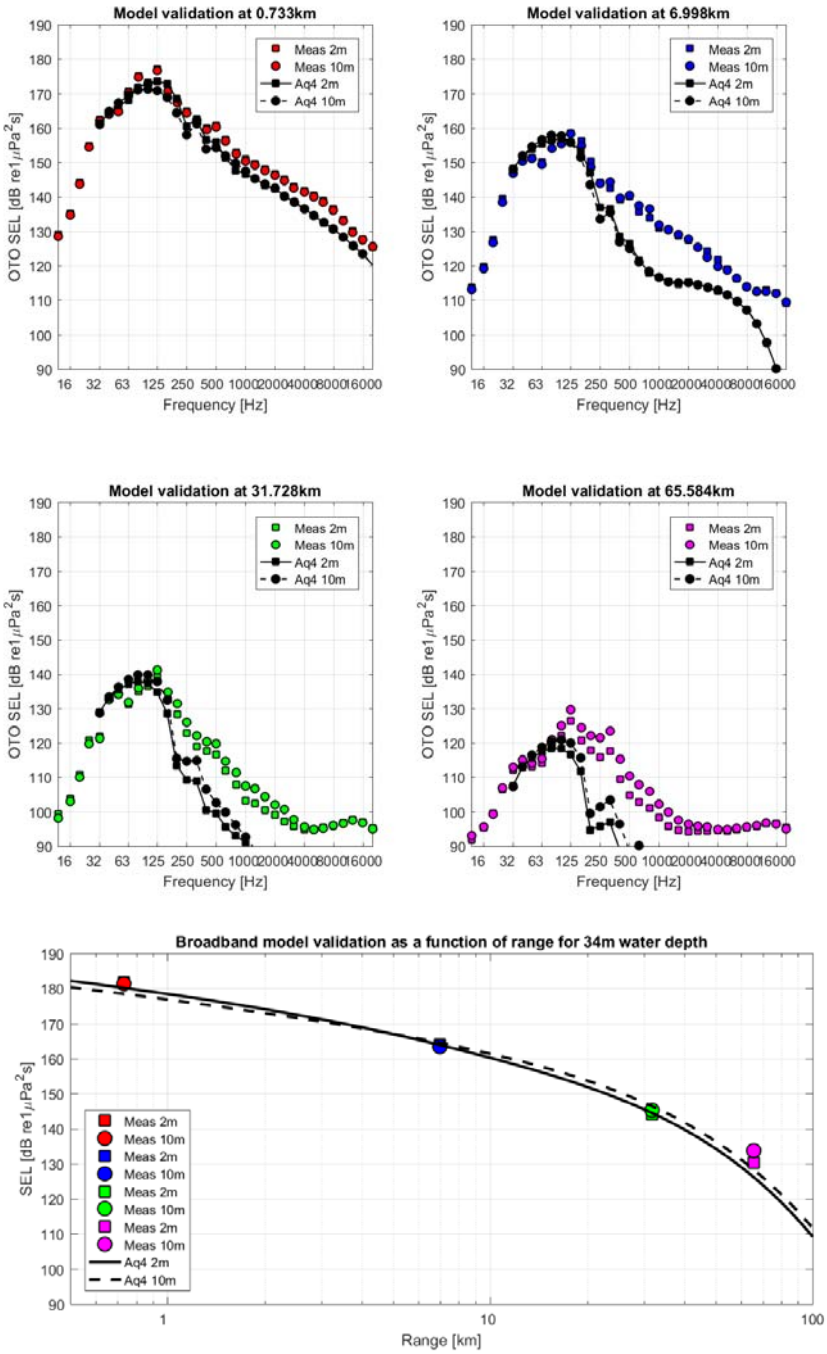


Figure 28 Comparison of predictions with the updated Aquarius 4 line source model including the Deeks model for the hammer force, for wind speed 0 m/s, and 'medium sand' sediment parameters according to the Williams [2013] model (Figure 26) with measurements for the Gemini U8 piling. Upper figures: 1/3-octave band spectra of SEL at the four measurement distances. Lower figure: broadband SEL as a function of range. Note that measurement data in the upper part of the frequency range are limited by background noise at 7 km and beyond.

## 7.5 Conclusions

- The scientific literature indicates that ‘sandy’ sediment in shallow coastal waters exhibits frequency dependent acoustic properties. In particular the absorption at frequencies below ~1 kHz is generally lower than predicted by a linear extrapolation from empirical values for higher frequencies.
- Geoacoustic models for porous sand media are available (e.g. Williams [2001&2013]), but the specific sediment properties (porosity, permeability and tortuosity as a function of depth) required by these models are not readily available for the North Sea piling environments. The local geotechnical surveys for the wind farm projects do not directly provide these parameters and, moreover, do not cover the area over which the sound propagation is to be calculated. Finally, the comparison with the available data [Williams, 2001&2013] shows that uncertainty in the sediment models is significant even for known specific sediment properties.
- The Aquarius 4 implementation with the updated sediment models for ‘medium sand’, either with an adapted attenuation (trend $f^{1.8}$) below 250 Hz or using the Williams [2013] EDFM model with an appropriate estimation of the input parameters, provide a much better agreement with the measurements at low frequencies, and for the broadband SEL, than the previous predictions [Binnerts et al, 2016].
- At higher frequencies (> 125 Hz), the Aquarius 4 predictions underestimate the measured SEL spectrum (Figures 27 and 28). This will result in an underestimation of weighted SEL metrics and of the effectiveness of mitigation measures (Chapter 8).
- We tentatively identify the following possible explanations for the underestimation of the SEL at higher frequencies:
    - the validity of the simplified hammer model is limited to lower frequencies (Chapter 5)
    - the simplified line source model underestimates the excitation of the lowest modes (small grazing angle) in the waveguide (Section 4.4)
    - the sediment model overestimates the bottom losses at higher frequencies
- Further investigation of these explanations could not be achieved in the scope of the current study.

# 8 Model for frequency dependent effects of mitigation measures on sound radiation (improvement G)

To date, all Aquarius 1 and 3 predictions of the effect of mitigation measures, such as bubble screens, have been based on the tentative assumption that the broadband transmission loss that has been measured in the field for various mitigation measures can be subtracted from the calculated broadband SEL distribution. This approach does not well represent the physics of the effect of the various mitigation measures on the piling noise. It ignores the frequency-dependence of the mitigation measure, the role of the sound transmission in the seabed below measures close to the pile and the effect of the measures on the directionality of the sound radiation.

As a first step, we have implemented a frequency dependent loss, based on published data of measured insertion loss of noise mitigation systems.

Various underwater noise mitigation systems for marine pile driving are available. Since 2011 these are required in German waters to meet the limiting values imposed by the authorities to protect harbour porpoises [BMU, 2014]. Overviews of various systems are given by Koschinski & Lüdemann, [2013] and by Bellmann [2014]. Figure 29 shows the measured effectiveness of some configurations, in terms of their 'insertion loss'.

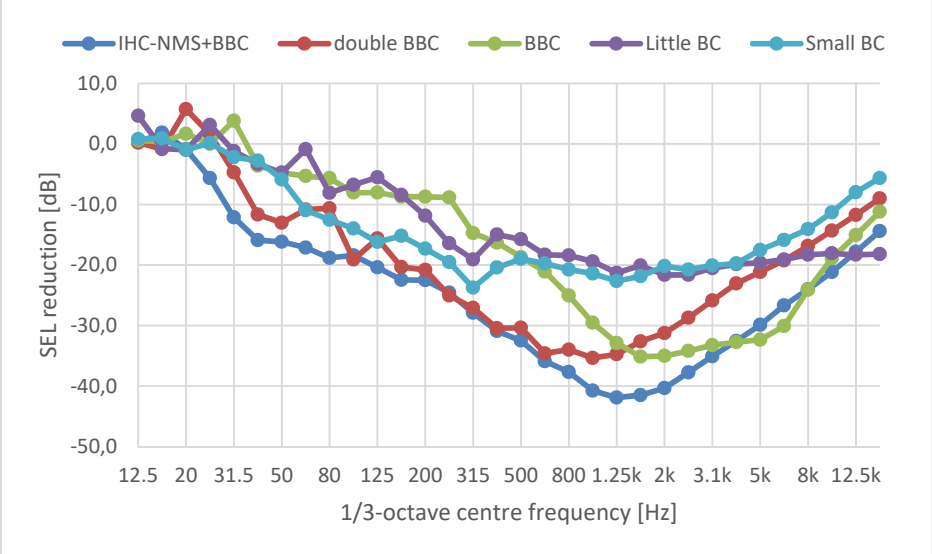


Figure 29: Overview of the measured insertion loss of different noise mitigation systems, after [Bellmann, 2014]: IHC-NMS = IHC noise mitigation screen, BBC = big bubble curtain.

Here insertion loss is defined as the difference between the measured SEL 1/3-octave band spectra at a fixed distance (750 m) from the pile for piling configurations with and without mitigation.

This demonstrates that the insertion loss is strongly frequency-dependent, with the highest reductions at frequencies above 500 Hz. Note that we have doubts whether the decreasing effectiveness towards higher frequencies is real. It might be due to measurement problems. However, this does not affect the assessment of broadband sound reduction, since the main energy of the piling sound is at lower frequencies.

The scientific modelling of the effectiveness of noise reduction measures such as bubble curtains is under development, see e.g. Bohne et al [2016]. Implementation of such models in the Aquarius suite would require more effort than foreseen in the scope of the current project.

Further investigation of 'Shielding noise by bubble curtains and the effect of water quality', has been included in a PhD proposal (part of the program proposal *"AQUA" – water quality in maritime hydrodynamics*) from Twente University, in which TNO and MARIN participate, for the NWO 'perspective round 2017/2018 phase 3'.

In the TKI project '*Underwater Noise Abatement System for Pile Driving*' (*UNAS*), TNO will be developing a model for the AdBm Noise Abatement System, which uses encapsulated air bubbles, tuned to specific frequencies and arranged in specific configurations, to mitigate underwater noise.

The outcomes of these projects will be relevant for future updates of the Aquarius suite, but will not be available on time to be used for the model update in the current project. Hence, the Aquarius 4 update will be limited to an implementation of measured insertion loss for selected mitigation systems (insofar as data are available). This approach is based on the (unverified) assumption that the vertical directionality of the acoustic field is not affected by the insertion loss.

In attempt to quantify the contribution of sound propagating through the seabed under the bubble screen and to what extent that path contributes to the assessment of the effectiveness of the screen, we have built a simple model, described in Appendix D. This model focusses on the effects of the distance between pile and the bubble screen and the distance to the measurement position. Example calculations suggest that these bottom path contributions are mainly relevant at shorter distances from the pile. Because the bottom path corresponds with rather steep ray angles in the water, above the critical angle for reflection, the cycle distance is rather short and the reflection loss is high, resulting in a high propagation loss. Beyond a distance of e.g. 10 times the water depth the contribution of this path appears to be negligible.

# 9 Update and verify model infrastructure (improvement H)

The model updates suggested in the previous chapters have been integrated into a new Aquarius 4 sound mapping tool which is included in the SORIANT sound risk assessment tool, that is used by TNO for environmental impact assessment studies [von Benda Beckmann et al, 2015].

## 9.1 Software update

The following software updates have been carried out within the Wozep project

- Development of a new 'Aquarius 4' line source and propagation model, which includes the following model improvements:
  - Point source excitation replaced by a line source model (Section 4.2)
  - Option to model wind losses using an updated version of the Weston and Ching model (Chapter 6, appendix C)
  - The integration of the Deeks hammer excitation model (Chapter 5)
  - Option to include nonlinear frequency dependence of the sediment properties used by the propagation model (Chapter 7)
- The option to add frequency dependent mitigation effectiveness (Chapter 8)
- An update of the sound mapping framework that can provide the same type of graphical output generated by the Aquarius 1 tool previously used for piling noise studies.

## 9.2 Model input

The following model input is required to run the new Aquarius 4 model:

**Environment parameters:**

- Sediment: sand type or properties (default 'medium sand' parameters [Ainslie, 2010, table 4.18], with a non-linear attenuation trend $f^{1.8}$ below 250 Hz))
- Water: sound velocity (iso-velocity, default 1500 m/s) and density (default 1024 kg/m$^3$). Attenuation is included using Thorp's formula [Ainslie, 2010]
- Surface: wind speed at 10 m height above the water surface (default 0 m/s)

**Pile parameters:**

- Pile location (Lat-Lon)
- Water depth at pile location (m)
- Pile diameter (m)
- Wall thickness (mm)
- Pile length (m)
- Penetration depth in the sediment (m)

- Material parameters (default steel): Young's modulus (default 210 GPa), Poisson ratio (default 0.3) and density (default 7800 kg/m$^3$).

**Hammer parameters:**

- Strike energy (kJ)
- Ram mass (kg)
- Anvil mass (kg)
- Contact stiffness ram-anvil (default 20 GPa)

## 9.3 Examples of Aquarius 4 sound mapping

The Aquarius 4 sound mapping uses an $N \times 2D$ modelling approach, in which the propagation of piling sound is calculated in two spatial dimensions (range and depth) along a series of $N$ radial straight tracks, as shown in Figure 30.
The SEL values at other map locations (outside these radials) are determined by spatial (linear) interpolation.

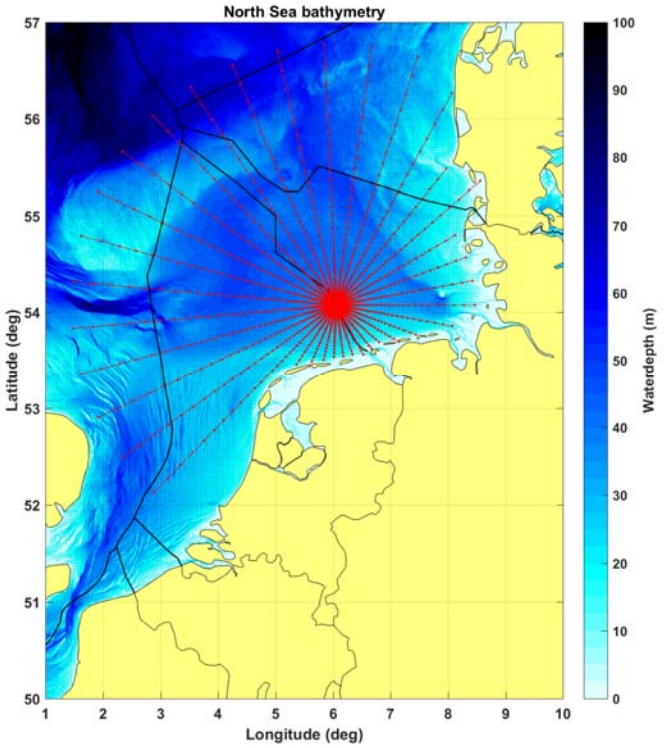


Figure 30: North Sea bathymetry map with black lines indicating the national borders and red lines indicating the radial track lines along which the sound propagation is calculated, for piling of the Gemini U8 wind turbine foundation.

Figure 31 illustrates the resulting sound maps, for the Gemini U8 piling, modelled with Aquarius 1 (with wind (8.8m/s) and 'medium sand' sediment) and Aquarius 4 (no wind and 'medium sand' sediment with non-linear absorption correction) and the capability to determine the area in which the SEL exceeds a threshold values.

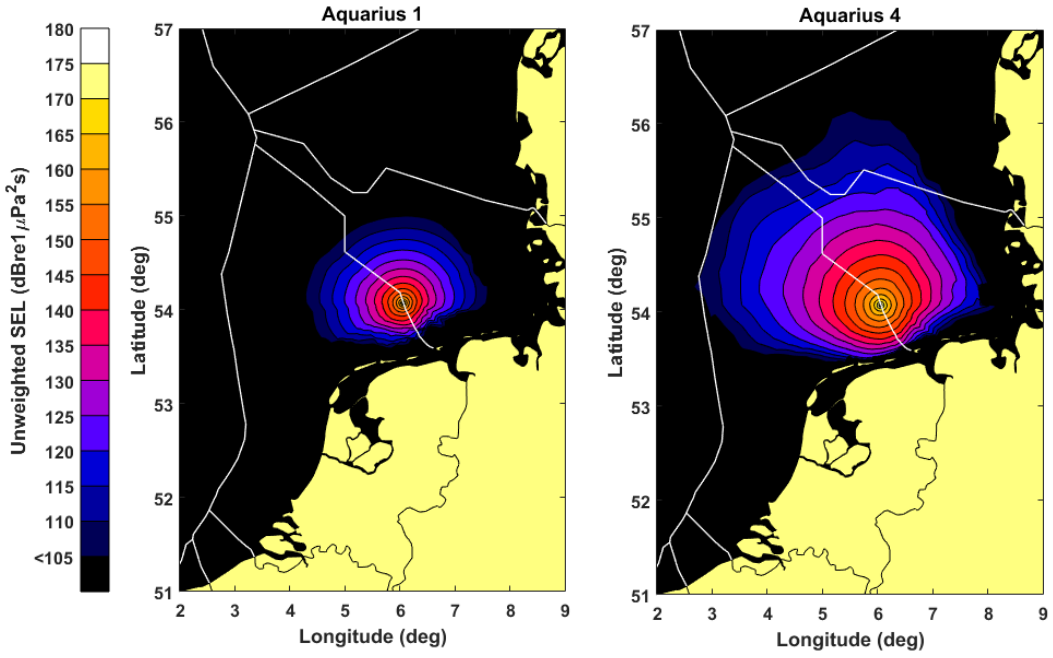


Figure 31: Example maps of the maximum over depth unweighted broadband single strike sound exposure level for piling of the Gemini U8 wind turbine foundation, calculated by Aquarius 1 (left) and Aquarius 4 (right).

The new Aquarius 4 tool introduces a directional line source model in combination with a normal mode propagation model. This approach deviates significantly from the point source model in combination with an energy flux model in Aquarius 1. Figure 32 illustrates the differences between model predictions. Where Aquarius 1 predicts the highest SEL values at the sea floor, the dominating lowest mode at lager distances in Aquarius 4 has the highest SEL closer to mid water.
The measurement results at larger distances for the Gemini piling (see e.g. Figure 28) confirm that the SEL at 2 m above the sediment is lower than at 10 m.

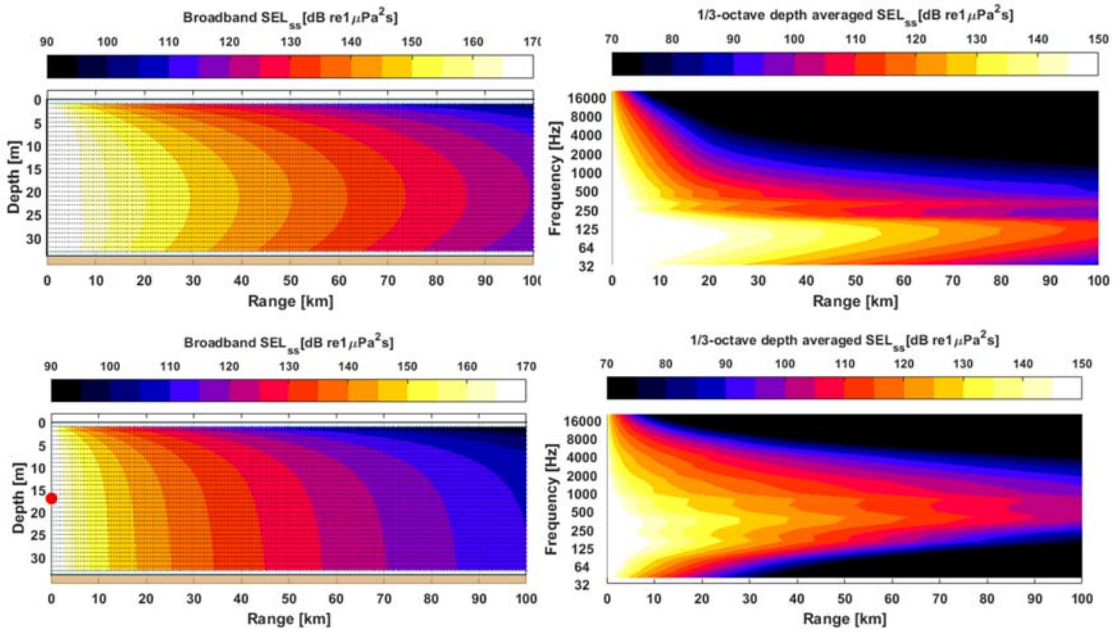


Figure 32: Examples of the calculated unweighted broadband single strike sound exposure level as a function of depth and range (left figures), and of the depth averaged 1/3-octave band spectrum of the SEL, as calculated by Aquarius 1 (top) and Aquarius 4 (bottom).

## 9.4 Aquarius 4 validation and comparison with Aquarius 1

A final comparison of the updated Aquarius 4 and the original Aquarius 1 modelling results with the measurement data from the piling for the Gemini U8 foundation pile [Binnerts et al,] is shown in Figure 33.

The upper figure shows that the Aquarius 4 improvements lead to an acceptable agreement between predicted and measured broadband unweighted SELss for the Gemini U8 pile. Further validation against data from other North Sea piling projects is highly recommended, since the model parameters for the source (e.g. contact stiffness) and the environment (sediment properties) were optimized to achieve the best match with the measurements results for Gemini U8.

The comparison of modelled and measured SELss spectra show that the Aquarius 4 improvements mainly affect the low frequencies (< 250 Hz) that dominate the unweighted broadband SELss. The deviation between predictions and measurement results increases with increasing frequency and increasing measurement distance. Though this might suggest that this is mainly caused by a deviation in the applied propagation model, it cannot be excluded that (part of) this deviation is caused by the (directional) line source model. Increasing differences with increasing distance may indicate an underestimation of the source level for the shallower angles, which contribute most to the long distance propagation.

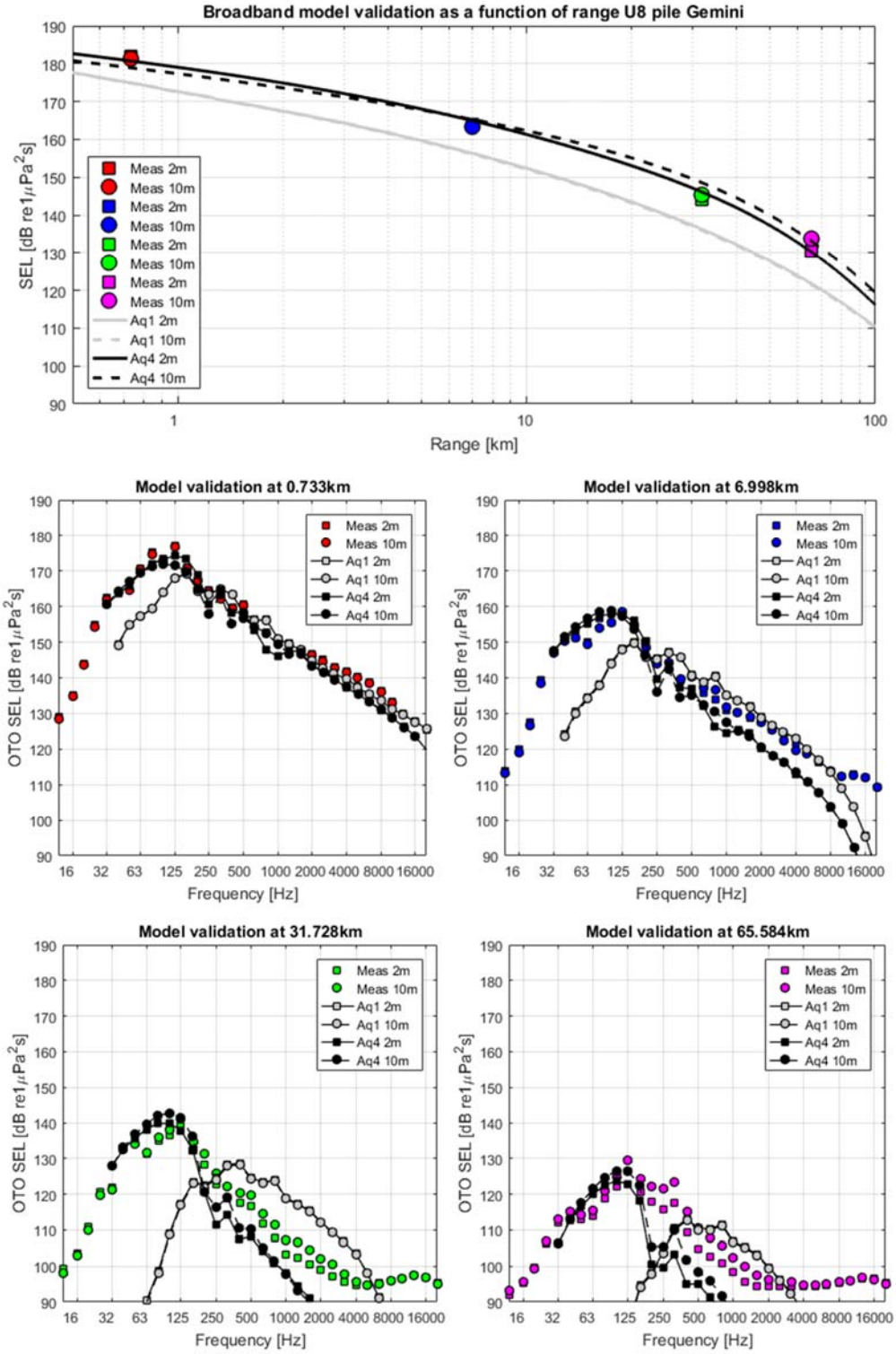


Figure 33: Broadband(top) and One Third Octave SEL for the U8 pile in the Gemini windfarm. Shown are the measurements (coloured markers) and modelling results (solid and dashed lines) for the Aquarius 1 (grey) and Aquarius 4 (black) models. Note that the measurement results in the highest frequency bands are background noise limited.

# 10 Summary and conclusions

Work Package 2 of the Wozep underwater sound study has resulted in a major step forward towards including the proper physics (line source model, hammer model) in the piling sound modelling as first step in the assessment of the impact of the underwater sound of North Sea piling projects on porpoises and seals.

The model updates have been integrated into a new Aquarius 4 sound mapping tool which is included in the SORIANT sound risk assessment tool, that is used by TNO for environmental impact assessment studies.

Aquarius 4 includes the following model improvements:

- Point source excitation replaced by a line source model (Chapter 4)
- The integration of the Deeks hammer excitation model (Chapter 5)
- Option to model wind losses using an updated version of the Weston and Ching model (Chapter 6)
- Option to include nonlinear frequency dependence of the sediment properties used by the propagation model (Chapter 7)
- The option to add frequency dependent mitigation effectiveness (Chapter 8)
- An update of the sound mapping framework that can provide the same type of graphical output generated by the Aquarius 1 tool previously used for piling noise studies Chapter 9).

The introduction of the hammer model and the one-dimensional model for the pile enable incorporating the effects of pile length, pile diameter and hammer and anvil properties on the radiated sound. This largely reduces the uncertainty in the source modelling at the frequencies (~50-250 Hz) that dominate the unweighted broadband SEL. This new modelling approach avoids the underestimation of the SEL for the large piles at Gemini that was observed for the semi-empirical point source model in Aquarius 1.

This study also demonstrated the need for a better characterization of the influence of environmental parameters (sediment and wind) on the sound propagation. Modelling of these influences remains an area of considerable uncertainty. Determining if the uncertainty can be further reduced would require significant additional research, well outside of the scope of this study. In the scope of this project, tentative suggestions for selecting environmental parameters are proposed which seem to reduce the uncertainty in the SEL estimations for the dominant low frequency component of the SEL for the North Sea piling scenarios for which the models have been validated.

In spite of improvements in the description of the physics of the piling sound radiation and propagation, quantitative prediction of the high frequency content of the SEL remains very uncertain. Here a further investigation of the available data from different projects might lead to suggestions for (empirical) corrections to the modelling.

To what extend the modelling uncertainty affects the KEC assessment depends on the final selection of the relevant metric. The figures in Section 9.2 demonstrate that the prediction of the broadband SEL is satisfactory, but the predicted levels at higher frequencies (typically > 1 kHz) are up to 10 dB lower than the measured levels. It is still unclear whether this underestimation is the result of an underestimation of the radiated sound from the pile or of an overestimation of propagation loss, or a combination of both. Further validation of the models against data from other North Sea piling projects is highly recommended to reduce this uncertainty.

Further improvements of the Aquarius model could be:

- **Improvement of the source modelling:** More detailed modelling of the dynamic behaviour of ram, anvil and pile, e.g. using finite element modelling or wave equation analysis (WEAP), could possibly lead to a better prediction of the piling sound at higher frequencies. However, the amount of detail in the modelling is necessarily limited by availability of detailed information in the prediction stage of the wind farm construction projects and by numerical requirements (memory use and calculation time).
- **Improvement of the acoustic modelling of the sea floor:** In particular the acoustic properties of the sediment at lower frequencies (< 1 kHz) requires further investigation. Frequency dependence of these properties has been demonstrated to have a large impact on propagation loss. Moreover, the Aquarius 4 model does not include propagation from the seabed into the water column which is particularly relevant when mitigation measures are taken close to the pile.
- **Improvement of the acoustic modelling of the sea surface:** The available semi-empirical models are currently used outside the range of applicability in terms of frequencies and wind speeds. Further research would be needed to extend the applicability of the acoustic models of the sea surface.

At this moment, the amount of data suitable for the validation of the model is limited, resulting in a significant uncertainty associated with the current modelling capability. While modelling results showed good agreements with the measured broadband SEL for the U8 Pile, seabed properties were calibrated against measurement data for this pile. Therefore, the first step towards reducing the uncertainty would be the validation of the model for a wider range of scenarios (both for different pile-hammer configurations and different environmental conditions).

Ideally the source model would be validated independently from the propagation model. Direct validation of the line source model can be carried out by comparing the radial expansion of the pile or the sound pressure distribution over the water column close to the pile with measurements. However, previous validation efforts for the Kinderdijk pile showed that measuring the radial accelerations on the pile is subject to large uncertainties.

To reduce the uncertainty regarding the sound propagation, additional validation at both small and large distances is needed. Such measurements should include scenarios with and without applying mitigation measures, preferably for the same pile location to quantify the mitigation effectiveness.

# 11 References


| | |
|---|---|
| Ainslie, 1995 | Ainslie, M.A. (1995) 'Plane-wave reflection and transmission coefficients for a three-layers elastic medium', J. Acoust. Soc. Am. 97 (2): 954-961 |
| Ainslie, 2005 | Ainslie, M.A. (2005) 'Effect of wind-generated bubbles on fixed range acoustic attenuation in shallow water at 1–4 kHz', J. Acoust. Soc. Am. 118(6): 3513–3523 |
| Ainslie, 2010 | Ainslie, M.A. (2010), 'Principles of sonar performance modelling', Springer-Praxis, Chichester, UK |
| APL, 1994 | APL (1994) 'APL-UW High-Frequency Ocean Environmental Acoustic Models Handbook', Technical Report APL-UW TR 9407 AEAS 9501, Applied Physics Laboratory, University of Washington, Seattle |
| Bachman, 1985 | Bachman, R.T. (1985), 'Acoustic and physical property relationships in marine sediment', J. Acoust. Soc. Am. 78(2), 616-621 |
| Bellmann, 2014 | Bellmann, M.A. (2014) 'Overview of existing noise mitigation systems for reducing pile-driving noise', Proc. Internoise 2014, Melbourne, Australia |
| von Benda-Beckmann et al, 2015 | von Benda-Beckmann, S., de Jong, C., Binnerts, B., de Krom, P., Ainslie, M., Nijhof, M. and te Raa, L.(2015) 'SORIANT VUM - final report', report TNO 2015 R10791 |
| von Benda-Beckmann et al, 2017 | von Benda-Beckmann, S., de Jong, C., Prior, M., Binnerts, B., Lam, F.-P., Ainslie, M. (2017) 'Modelling sound and disturbance maps using the impulsive noise register for assessing cumulative impact of impulsive sound', report TNO 2017 R11282 |
| Binnerts et al, 2016 | Binnerts, B., de Jong, C.A.F., Ainslie, M.A., Nijhof, M.J.J., Müller, R.A.J. and Jansen, H.W. (2016), 'Validation of the Aquarius models for prediction of marine pile driving sound', report TNO 2016 R11338 |
| BMU, 2014 | German Federal Ministry for the Environment and Nuclear Safety (2013) `Konzept für den Schutz der Schweinswale vor Schallbelastungen bei der Errichtung von Offshore- Windparks in der deutschen Nordsee (Schallschutz - konzept)', BMUB, Berlin |
| Bohne et al, 2016 | Bohne, T., Griessmann, T. and Rolfes, R. (2016), ,Integral approach for modelling offshore bubble curtains', Proc. Internoise 2016, Hamburg, Germany |
| BORA, 2017 | "Documentation of the underlying data base and the numerical model of the BORA Expert System", Available from: https://bora.isd.uni-hannover.de/ (last accessed 4 May 2018) |
| Dahl & Choi, 2006 | Dahl, P.H. and Choi, J.W. (2006) 'Precursor arrivals in the Yellow Sea, their distinction from first-order head waves, and their geoacoustic inversion', J. Acoust. Soc. Am. 120(6), |
| Dahl & Reinhall, 2013 | Dahl, P.H. and Reinhall, P.G. (2013), 'Beam forming of the underwater sound field from impact pile driving', J. Acoust. Soc. Am. 134(1): EL1 |

| | |
|---|---|
| Deeks & Randolph, 1993 | Deeks, A.J. and Randolph, M.F. (1993), 'Analytical modelling of hammer impact for pile driving', International Journal for Numerical and Analytical Methods in Geomechanics, 17: 279-302 |
| Fricke & Rolfes, 2015 | Fricke, M. and Rolfes, R. (2015) "Towards a complete physically based forecast model for underwater noise related to impact pile driving," J. Acoust. Soc. Am. 137(3): 1564-1575 |
| Geelhoed et al, 2013 | Geelhoed, S.C.V., Scheidat, M., van Bemmelen, R.S.A. and Aarts, G. (2013), 'Abundance of harbour porpoises (*Phocoena phocoena*) on the Dutch Continental Shelf, aerial surveys in July 2010-March 2011', Lutra 2013 56 (1): 45-57 |
| Hamilton, 1980 | Hamilton, E.L. (1980) "Geoacoustic modeling of the sea floor", J. Acoust. Soc. Am. 68(5), 1313-1340 |
| Hamilton, 1985 | Hamilton, E.L. (1985) "Sound velocity as a function of depth in marine sediments", J. Acoust. Soc. Am. 78 (4), 1348-1355 |
| Harrison, 2003 | Harrison, C.H. (2003) "Closed-form expressions for ocean reverberation and signal excess with mode stripping and Lambert's law", J. Acoust. Soc. Am. 114(5): 2744–2756 |
| Harwood et al, 2014 | Harwood, J., King, S., Schick, R., Donovan, C. & Booth, C. (2014) A protocol for implementing the interim population consequences of disturbance (PCoD) approach: quantifying and assessing the effects of UK offshore renewable energy developments on marine mammal populations. Report number smrul-tce-2013-014. *Scottish Marine and Freshwater Science*, **5**(2). |
| Heinis & de Jong, 2015 | Heinis, F., de Jong, C.A.F. and Rijkswaterstaat Underwater Sound Working Group (2015), 'Cumulative effects of impulsive underwater sound on marine mammals', report TNO 2015 R10335-ENG |
| Heitmann et al, 2015 | Heitmann, K., Mallapur, S., Lippert, T., Ruhnau, M., Lippert, S. and von Estorff, 0. (2015) "Numerical determination of equivalent damping parameters for a finite element model to predict the underwater noise due to offshore pile driving," in Euronoise 2015, Maastricht |
| Jensen et al, 2011 | Jensen, F.B., Kuperman, W.A., Porter, M.B. and Schmidt, H. (2011) "Computational Ocean Acoustics", 2nd ed., Springer, New York |
| de Jong, 1994 | de Jong, C.A.F. (1994), 'Analysis of pulsations and vibrations in fluid-filled pipe systems', PhD Thesis, Eindhoven University of Technology |
| de Jong & Ainslie, 2012 | de Jong, C.A.F. and Ainslie, M.A. (2012) 'Underwater sound due to piling activities for Prinses Amaliawindpark', report TNO 2012 R10081 |
| de Jong & von Benda-Beckmann, 2018 | de Jong, C.A.F. and von Benda-Beckmann, A. (2018), 'Wozep underwater sound: frequency sensitivity of porpoises and seals', report TNO 2017 R11238 |
| Kibblewhite, 1989 | Kibblkewhite, A.C. (1989) "Attenuation of sound in marine sediments: a review with emphasis on new low-frequency data", J. Acoust. Soc. Am. 86(2), 716-738 |

| | |
|---|---|
| Kornhauser & Raney, 1955 | Kornhauser, E.T. & Raney, W.P. (1955), 'Attenuation in shallow-water propagation due to an absorbing bottom', J. Acoust. Soc. Am. 27(4): 689-692 |
| Koschinski & Lüdemann, 2013 | Koschinski, S. & Lünemann, K. (2013), 'Development of Noise Mitigation Measures in Offshore Wind Farm Construction', Federal Agency for Nature Conservation (Bundesamt für Naturschutz, BfN) report, Germany |
| Kringelum et al, 2015 | Kringelum, J.V., Lippert, S., Heimann, K., Schmidt Lützen, Trimoreau, B & Skjellerup, P. (2015), 'The use of numerical modelling to assist and improve industrial understanding of underwater noise and relevant mitigation measures', Proc. Euronoise 2015, Maastricht |
| Lippert et al, 2018 | Lippert, T., Ainslie, M.A., von Estorff, O. (2018), ,Pile driving acoustics made simple; damped cylindrical spreading model', J. Acoust. Soc. Am. 143(1): 310-317 |
| Nijhof et al, 2014 | Nijhof,M.J.J., Binnerts, B., de Jong, C.A.F., Ainslie, M.A. (2014) 'An efficient model for prediction of underwater noise due to pile driving at large ranges', Proc. Internoise 2014, Melbourne |
| Nijhof et al, 2015 | Nijhof,M.J.J., Binnerts, B., Ainslie, M.A., de Jong, C.A.F, (2015), 'Integration source model and propagation model', report TNO 2015 R10186 |
| NMFS, 2016 | National Marine Fisheries Service (2016) 'Technical Guidance for Assessing the Effects of Anthropogenic Sound on Marine Mammal Hearing: Underwater Acoustic Thresholds for Onset of Permanent and Temporary Threshold Shifts'. NOAA Technical Memorandum NMFS-OPR-55, http://www.nmfs.noaa.gov/pr/acoustics/Acoustic%20Guidance%20Files/opr-55_acoustic_guidance_tech_memo.pdf |
| Porter, 2001 | Porter, M.B. (2001) 'The Kraken normal mode program', manual available from http://oalib.hlsresearch.com |
| Reinhall & Dahl, 2011 | Reinhall, P. and Dahl, P. (2011) "Underwater Mach wave radiation from impact pile driving: Theory and observation," J. Acoust. Soc. Am. 130(3): 1209-1216 |
| Remmerts & Bellmann, 2015 | Remmerts, P. & Bellmann, M.A. (2015) 'Ecological monitoring of underwater noise during piling at Offshore Wind Farm *Eneco Luchterduinen*', report 2322-14-bel, ITAP Oldenburg |
| Remmerts & Bellmann, 2016 | Remmerts, P. & Bellmann, M.A. (2016) 'Ecological monitoring of underwater noise during piling at Offshore Wind Farm *Gemini*', report 2571-15, ITAP Oldenburg |
| Sertlek & Ainslie, 2014 | Sertlek, H.Ö. and Ainslie, M.A. (2014) "A depth-dependent formula for shallow water propagation," J. Acoust. Soc. Am. 136(2): 573-582 |
| Sertlek, 2016 | Sertlek, H.Ö. (2016) "ARIA OF THE DUTCH NORTH SEA: Propagation, source and sound mapping simulations for the Dutch North Sea", Leiden: PhD Thesis |
| Trimoreau et al, 2014 | Trimoreau, B., Schmidt Lützen, R., Kringelum, J.V., Shajarati, A.& Skjellerup, P. (2014), 'New achievements in underwater noise modelling for offshore pile driving', Proc. Internoise 2014, Melbourne |
| van Walree et al, 2007 | Van Walree, P., Ainslie, M.A. and Janmaat, J (2007) 'Influence of bottom trawling on the normal incidence reflection coefficient', |

| | |
|---|---|
| | Proceedings 2nd International Conference on Underwater Acoustic Measurements, Heraklion, Greece |
| Weston, 1971 | Weston, D.E. (1971) “Intensity-range relations in oceanographic acoustics,” Journal of Sound and Vibration 18(2): 271-287 |
| Weston, 1976 | Weston, D.E. (1976) “Propagation in water with uniform sound velocity but variable-depth lossy bottom,” Journal of Sound and Vibration 47(4): 473-383 |
| Weston & Ching, 1989 | Weston, D.E. and Ching, P.A. (1989), ‘Wind effects in shallow-water acoustic transmission’, J. Acoust. Soc. Am. 86(4): 1530-1545 |
| Wilkes et al, 2016 | Wilkes, D.R., Gourlay, T.P., Gavrilov, A.N. (2016) ‘Numerical Modeling of Radiated Sound for Impact Pile Driving in Offshore Environments’, IEEE JOURNAL OF OCEANIC ENGINEERING, VOL. 41, NO. 4, 1072-1078 |
| Wilkes & Gavrilov, 2017 | Wilkes, D.R., Gavrilov, A.N. (2017) ‘Sound radiation from impact-driven raked piles’, J. Acoust. Soc. Am. 142 (1), 1-11 |
| Williams, 2001 | Williams, K.L. (2001) ‘An effective density fluid model for acoustic propagation in sediments derived from Biot theory’, J. Acoust. Soc. Am. 110(5), 2276-2281 |
| Williams, 2013 | Williams, K.L. (2013) ‘Adding thermal and granularity effects to the effective density fluid model’, J. Acoust. Soc. Am. 133 (5), EL431-437 |
| Wood, 2016 | Wood, M.A. (2016) ‘Modelling and prediction of acoustic disturbances from off-shore piling’, PhD Thesis, University of Southampton, Faculty of Engineering and the Environment |
| Zampolli et al, 2013 | Zampolli, M., Nijhof, M.J.J., de Jong, C.A.F., Ainslie, M.A., Jansen, E.H.W. and Quesson, B.A.J. (2013) ‘Validation of finite element computations for the quantitative prediction of underwater noise from impact pile driving’, J. Acoust. Soc. Am. 133(1), 72-81 |
| Zhou et al, 2009 | Zhou, J.-X., Zhang, X.-Z. and Knobles, D. (2009), ‘Low-frequency geoacoustic model for the effective properties of sandy seabottoms’, J. Acoust. Soc. Am. 125(5): 2847-2866 |

# 12 Signature

The Hague, January 2018

TNO

Coen Ort
Head of department

Christ de Jong
Author

# A Analytical model for pile hammer impact

Author: Ingrid Mulders, TNO

## A.1 An analytical solution for pile hammer impact

For environmental impact assessment studies and in the development of permitting conditions for future windfarm installations acoustic modelling of the pile and its surrounding is applied. The starting point of such a modelling study is a model for the hammer force. Currently an empirically derived point source level is used, though uncertainties related to scaling the source level with pile diameter, water depth and hammer energy can be reduced by updating the hammer model (de Jong & Binnerts, 2018).
An analytical solution for pile hammer impact is given by Deeks & Randolph (Deeks & Randolph, 1993) for four different pile cases as shown in Figure A.1. The pile is represented by a dashpot with impedance Z and a lumped mass for the ram (case A). An anvil cushion can be added, which is represented by a spring (case B). Another lumped mass represents the anvil (case C). And finally, a damped anvil cushion can also be represented by a combination of a spring and a dashpot (case D).

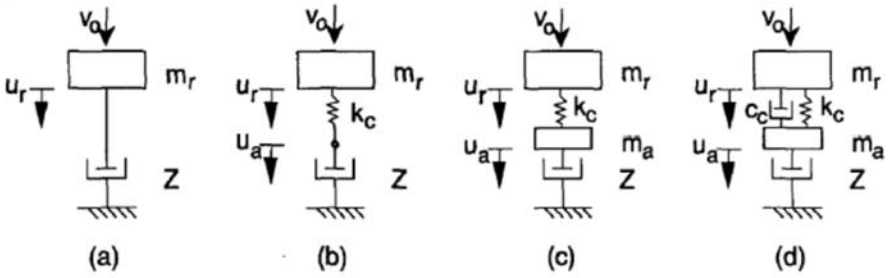


Figure A.1 Analytical pile hammer models as given by Deeks (Deeks & Randolph, 1993). (a) Ram/pile, (b) Ram/cushion/pile, (c) Ram/cushion/anvil and (d) Damped cushion model.

For all cases the accompanying equations of motions are analytically solved in the time domain using a Laplace transformation. Deeks & Randolph have used dimensionless variables to solve the equations. The final results are given below with the dimensionless substituted for dimensional parameters. A detailed derivation is given in Deeks & Randolph.

### *A.1.1 Parameters*

$f_p$ = force exerted on the pile
$v_0$ = velocity of the ram when it strikes the pile
$Z$ = pile impedance
$m_r$ = ram mass
$k_c$ = cushion stiffness
$m_a$ = anvil mass
$c_c$ = cushion damping

**Dimensionless variables**

$$f_p^* = \frac{f_p}{Z v_0}$$
$$t^* = \frac{Z}{m_r} t$$
$$k_c^* = \frac{k_c m_r}{Z^2}$$
$$m_a^* = \frac{m_a}{m_r}$$

### *A.1.2 Ram/Pile model (a)*

$$f_p = Z v_0 e^{-Zt/m_r}$$

### *A.1.3 Ram/Cushion/Pile model (b)*

For $k_c^* > 4$ $f_p = e^{-k_c/2Zt} \frac{v_0 k_c m_r \sinh\left(\frac{Z}{m_r t}\sqrt{\frac{k_c m_r}{Z^2}\left(\frac{k_c m_r}{4Z^2}-1\right)}\right)}{Z\sqrt{\frac{k_c m_r}{Z^2}\left(\frac{k_c m_r}{4Z^2}-1\right)}}$

For $k_c^* = 4$ $f_p = \frac{v_0 Z^2}{m_r t} e^{-k_c/2Zt}$

For $k_c^* < 4$ $f_p = e^{-k_c/2Zt} \frac{v_0 k_c m_r \sin\left(\frac{Z}{m_r t}\sqrt{\frac{k_c m_r}{Z^2}\left(1-\frac{k_c m_r}{4Z^2}\right)}\right)}{Z\sqrt{\frac{k_c m_r}{Z^2}\left(1-\frac{k_c m_r}{4Z^2}\right)}}$

### *A.1.4 Ram/Cushion/Anvil model (c)*

$$f_p = F_p Z v_0 e^{-c_2 t^*}\left(1 - e^{-c_2 t^*}\frac{\cos(\omega t^* - \varphi)}{\cos\varphi}\right)$$

With

$$a_0 = \frac{k_c^*}{m_a^*} = \frac{k_c m_r^2}{m_a Z^2} \quad a_1 = k_c^*\left(\frac{1}{m_a^*}+1\right) = \frac{k_c m_r}{Z^2}\left(\frac{m_r}{m_a}+1\right) \quad a_2 = \frac{1}{m_a^*} = \frac{m_r}{m_a}$$

$$\alpha = \frac{a_1 a_2}{6} - \frac{a_0}{2} - \frac{a_2^3}{27} = \frac{k_c^*}{2m_a^*}\left(\frac{1}{3}\left(\frac{1}{m_a^*}+1\right)-1\right) - \frac{{k_c^*}^2}{6}\left(\frac{1}{m_a^*}+1\right)^2$$

$$\beta = \sqrt{\frac{{k_c^*}^2}{27}\left(\frac{1}{m_a^*}+1\right)^3 - \frac{{k_c^*}^2}{108{m_a^*}^2}\left(\frac{1}{m_a^*}+1\right)^2 - \frac{{k_c^*}^2}{6{m_a^*}^2}\left(\frac{1}{m_a^*}+1\right) + \frac{{k_c^*}^2}{4{m_a^*}^2} + \frac{k_c^*}{27{m_a^*}^4}}$$

$$c_1 = \frac{a_2}{3} - (\alpha+\beta)^{1/3} - (\alpha-\beta)^{1/3}$$

$$c_2 = \frac{3}{2}\left[(\alpha+\beta)^{1/3} + (\alpha-\beta)^{1/3}\right]$$

$$\varphi = \tan^{-1}\left(\frac{\frac{3}{2}\left[(\alpha+\beta)^{1/3} + (\alpha-\beta)^{1/3}\right]}{\frac{\sqrt{3}}{2}\left[(\alpha+\beta)^{1/3} - (\alpha-\beta)^{1/3}\right]}\right)$$

$$\omega = \frac{\sqrt{3}}{2}\left((\alpha+\beta)^{1/3} - (\alpha-\beta)^{1/3}\right)$$

$$F_p = \frac{a_0}{3\left[(\alpha+\beta)^{2/3} + (\alpha-\beta)^{2/3} + (\alpha^2-\beta^2)\right]}$$

This solution is only valid for $\beta^2 > 0$, which is in practice almost always the case. This condition is not met for:
$k_c^* = 4 - 20$ & $m_a^* = 0 - 0.1$ → for $m_a \leq 100 m_r$

### *A.1.5 Damped cushion model*

An analytical solution for he damped cushion model is given by Deeks, though not implemented in the model of Gavrilov (see section below). Therefore no derivation is given here.

## A.2 Ram separation

For most values of dimensionless cushion stiffness and anvil mass the ram will separate from the cushion as it rebounds. Deeks and Randolph calculated the range of dimensionless parameters for which ram separation does and does not occur. As shown in Figure A.2 most hammers fall in the region for which ram separation occurs. For the cases where separation does occur, the time of separation, $t_s$, can be determined up to which time the given hammer model is valid.

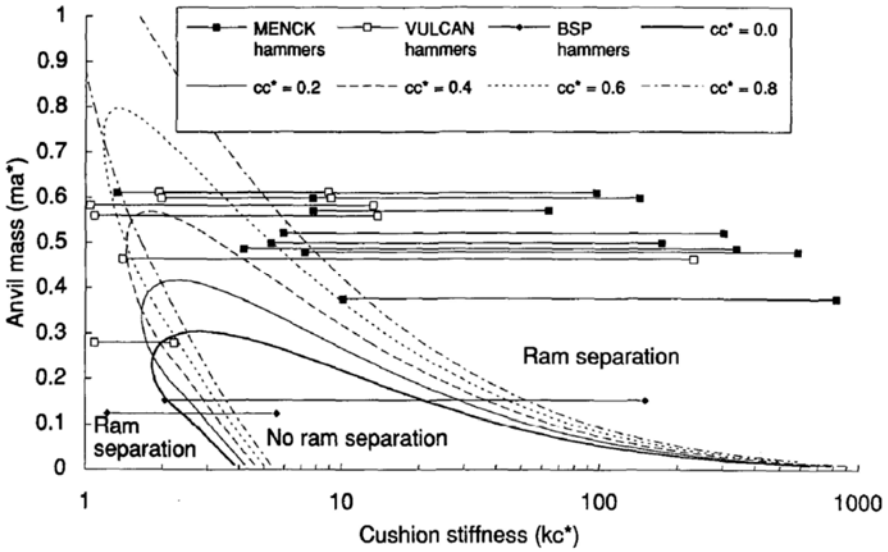


Figure A.2 Range of dimensionless parameters for a selection of hammers, and regions for which ram separation occurs (Deeks & Randolph, 1993).

The ram will separate when the spring force is zero. For the ram/cushion/pile model the force in the spring is equal to the force exerted on the pile, so $t_s$ can be determined for $k_c^* < 4$.

Ram/cushion/pile model: $t_s = \frac{\pi m_r}{\sqrt{k_c m_r \left(1 - \frac{k_c m_r}{4Z^2}\right)}}$

For the ram/cushion/anvil model the spring force is not equal to the force exerted on the pile, but equal to the force exerted on the anvil. $f_s$ can be determined, though it is not possible to find an analytical solution for $t_s$.

Ram/cushion/anvil model: $f_s = F_s Z v_0 \left(e^{-c_2 t^*} - \frac{\cos(\omega t^* - \theta)}{\cos\theta}\right)$

$$F_s = \frac{a_0(a_2 - c_1)}{\frac{3}{4}\left((\alpha+\beta)^{1/3} - (\alpha-\beta)^{1/3}\right)^2 + c_2^2}$$

$$\theta = \tan^{-1}\left(\frac{c_2(a_2 - c_1 - c_2) - \frac{3}{4}\left((\alpha+\beta)^{1/3} - (\alpha-\beta)^{1/3}\right)^2}{\frac{\sqrt{3}}{2}\left((\alpha+\beta)^{1/3} - (\alpha-\beta)^{1/3}\right)(a_2 - c_1)}\right)$$

And $t_s$ can be represented by

$$e^{c_2 t_s^*} = \frac{\cos(\omega t^* - \theta)}{\cos\theta}$$

For both cases: $f_p = 0$, for $t > t_s$

The effect of hammer impact after ram separation has been analytically determined by Take et al. (Take, et al., 1999) for a hammer that includes a cap cushion spring on top of the pile. Instead of using Laplace transforms Take et al. use closed form solutions.

## A.3 Other limitations of the analytical hammer model

The analytical model of Deeks and Randolph has been validated by comparing modelled results to measured forces. In general the two data sets match well as shown in Figure A.3 (right), though the field data shows more high frequency variation. Similar high frequency characteristics can be found in Fricke and Rolfes (Fricke & Rolfes, 2015). They use an analytical hammer model with a distributed mass for the ram instead of a lumped mass as the ram is in general several meters long. Their modelled results show similar high frequency behaviour as the field data for a mass distribution with n=200, though lack high frequency behaviour (>250 Hz) for a mass distribution with n=1 (i.e. a lumped mass). This mismatch is caused by vertical compression modes in the ram, which are neglected when the ram is represented by a lumped mass.

Another limitation is the validity of the model with respect to time and hammer parameters. First of all, the model only represents drop hammers, not diesel hammers. Luckily for marine use drop hammers are usually operated. Neither is it possible to incorporate a cap cushion on top of the pile. More recent models such as the one from Take et al. do take a cap cushion into account. As a last, the hammer model is only valid up to the point where reflections from the surface have reached the pile head again.

## A.4 Implementation of hammer model

The analytical hammer model of Deeks as described above has been implemented in Matlab by Gavrilov (Gavrilov, 2014) for the ram/pile, ram/cushion/pile and ram/cushion/anvil cases. Gavrilov uses the exact same approach as Deeks, though there are a few small deviations, which are discussed below.

### *A.4.1 Adaptations/deviations in the model*

1. Ram/cushion/pile model, equation for dimensionless pile force in the case $k_c^* = 4$.
   Deeks (eq. 21): $f_p^* = t^* e^{-k_c^* t^*/2}$
   Gavrilov: $f_p^* = t^* k_c^* e^{-k_c^* t^*/2}$
2. Ram/cushion/pile model, setting pile force to zero for $t > t_s$
   Gavrilov: $f_p^* < 0 \rightarrow f_p^* = 0$
   Debug: $f_p^*(t > t_s) = 0,\ t_s \text{ is } \min(t) \text{ for which } f_p^* < 0$
3. Ram/cushion/anvil model, equation to determine spring force (i.e. the force exerted on the anvil), $f_s$.
   Deeks (eq. 35): $f_s = F_s Z v_0 \left(e^{-c_2 t^*} - \frac{\cos(\omega t^* - \theta)}{\cos\theta}\right)$

Gavrilov: $f_s = Zv_0\left(\frac{m_a}{m_r}e^{-b_1 t^*}\left(-b_1\left(1-\frac{e^{-c_2 t^*}\cos(\omega t^*-\varphi)}{\cos\varphi}\right)+\frac{e^{-c_2 t^*}}{\cos\varphi}\right)(c_2\cos(\omega t^*-\varphi)+\omega\sin(\omega t^*-\varphi))\frac{a_0}{\omega^2+c_2^2}+f_p\right)$

At this stage it is unclear which of the two formulas is correct. However, a test case shows the same results for both calculations as shown in Figure A.3. Although, this is a realistic test case, we can't conclude that the calculations are identical for all hammer setups. As the separation time of Gavrilov seems more likely than the one from Deeks, the recommendation is to use equation the fix of Gavrilov.

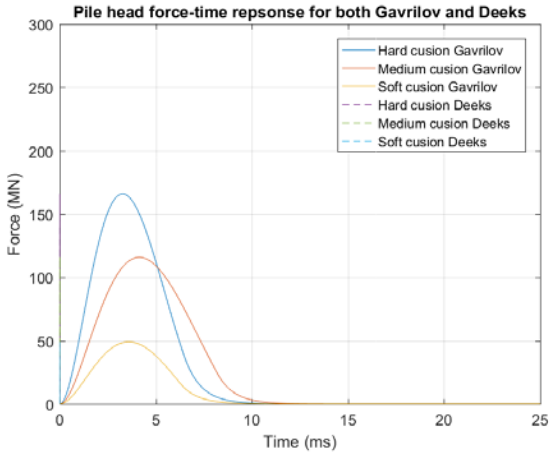


Figure A.3 Pile head force-time response using the spring force equation of both Gavrilov (solid line) and Deeks (dashed line).

### *A.4.2 Validation*

To assess the quality of the implemented hammer model, the modelled results need to be compared to field data or modelled result of a different model. In Table A.1 four hammer setups are given.

1. The Compile II test case is the hammer setup used by Gavrilov, though no force-time response of the hammer is given meaning this is not a valid test case. However, the pile parameters are realistic and can be used to get a general idea of the force-time response of hammers. Further details of this example can be found in (Lippert, et al., 2017).

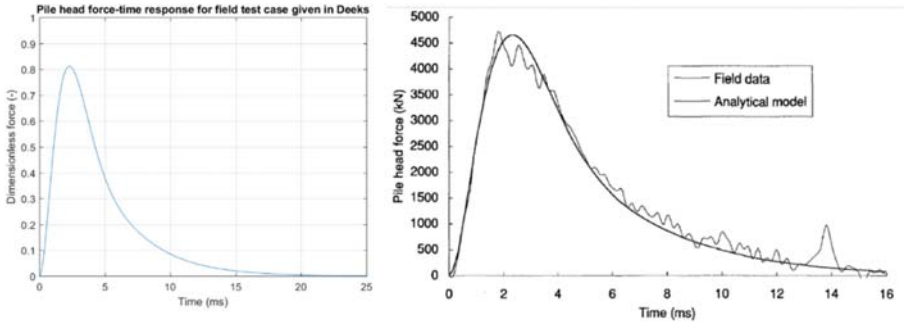


Figure A.4 Pile head force-time response for the pile parameters given for the field test in Deeks calculated using the implementation of Gavrilov (left, (Gavrilov, 2014)) and the model and field test data of Deeks (right, (Deeks & Randolph, 1993)).

2. Deeks compares the results of the hammer model with field test data. Unfortunately, Deeks doesn't provide the initial speed or energy of the hammer, so that only the dimensionless force-time response can be computed as shown in Figure A.4 (left). The shape of the curve, the timing of the maximum force and the time for which the force approximates zero are similar to the results given in Deeks (Figure A.4, right). The initial velocity and energy applied to the pile can be determined from both results and are given in Table A.1 and seem reasonable values.

3. Wood (Wood, 2016) uses a model described by Take et al. (Take, et al., 1999) and an implementation in Simulink. The model of Take et al. uses a similar setup as Deeks, but includes a pile cap cushion. Note that in the implementation of Wood the pile cap cushion is discarded.

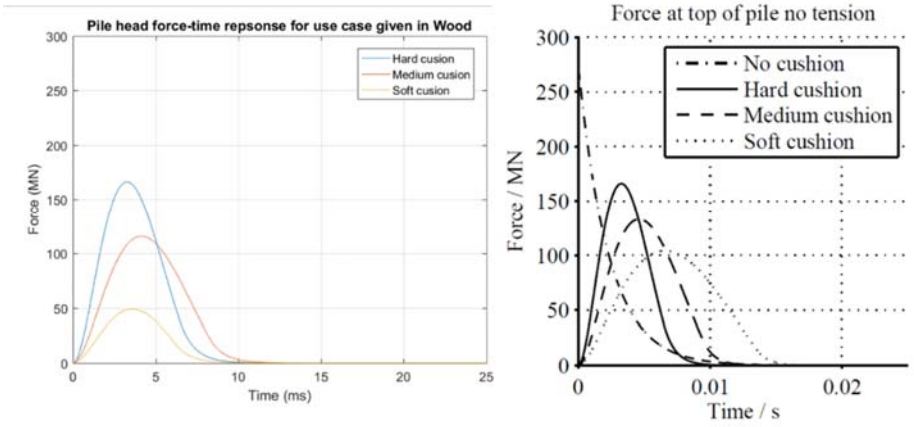


Figure A.5 Pile head force-time response for pile parameters given in Wood calculated using the Gavrilov implementation (left, (Gavrilov, 2014)) and the Wood implementation (right, (Wood, 2016)) for different cushion stiffnesses.

The results of the implementations of both Wood and Gavrilov are given in Figure A.5 for three different cushion stiffness's. The results are similar for the cases with a hard and medium cushion, but deviate in amplitude and timing for the soft cushion case. Note that for marine piles, cushions are usually absent.

4. Two other pile setups are given by Fricke (Fricke & Rolfes, 2015). Fricke compares field data from the BARDO offshore windmill park with modelled results in which a distributed mass is used for the ram and a damped cushion is included. The cushion stiffness is calculated using $k_c = \frac{E_{steel} m_r}{h_r^2 \rho_{steel}}$ and the damping coefficient using $c_c = 0.6\sqrt{m_r k_c}$. The results for the Gavrilov implementation, the Fricke implementation and the field data are given in Figure A.6. The results do not precisely match, which is expected as no damping is included in the Gavrilov implementation.

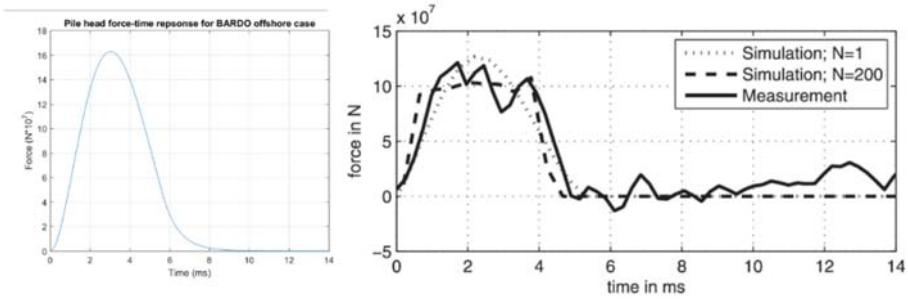


Figure A.6 Pile head force-time response for BARDO offshore case calculated using Gavrilov implementation (left, (Gavrilov, 2014)) and Fricke implementation (right, (Fricke & Rolfes, 2015)). The measured pile head force-time response is also given on the right.

Table A.1 Pile parameters for four different test cases. Shaded cells are values that are calculated using the dimensional and non-dimensional force exerted on the pile. The rest of values are measured or directly derived from measured data.

| | Test case Compile II | Field test Deeks | Test case Wood | BARDO offshore (Fricke) |
|---|---|---|---|---|
| Pile radius [m] | 5 | 0.381 | 3 | 3.35 |
| Wall thickness of pile [mm] | 90 | 18.5 | 65 | 70 |
| Mass anvil [kg] | 187 000 | 850 | 38 000 | 45 000 |
| Mass ram [kg] | 175 000 | 6860 | 100 000 | 95 000 |
| Cushion stiffness [N/m] | 10 – 100e9 | 1.6e9 | [5.25e9 10.5e9 21e9] | 2.5e10 |
| Cushion damping | - | - | - | 2.9e7 |
| Impedance [kNs/m] | 109 510 | 1750 | 43 470 | 57 067 |
| Initial speed of hammer [m/s] | 4.2 | 3.3 – 3.5 | 6.325 | 5.4 |
| Kinetic energy of hammer [kJ] | 1525 | 30 – 40 | 2000 | 1370 |

## A.5 Conclusion

An analytical model for pile hammer impacts has been given by Deeks & Randolph. The model gives a solution for simple hammer representations and shows a good match to field data. Note that the model is only valid up to the point of ram separation and does not include compressional modes in the ram or cushion damping. Although the model has some limitations and modifications are possible, the model is an improvement compared to the previously used point source level.

An implementation in Matlab has been made by Gavrilov, which has been compared to various data sets. Unfortunately, none of the available data sets were a complete match to the Gavrilov implementation and lacked either hammer parameters or used a slightly different hammer impact model. The closest validation data set is the data given by Wood, which showed similar results, except for a hammer with a soft cushion.

# B Line source model

Reinhall and Dahl [2011] introduce the concept of a 'Mach wave' to describe the sound wave radiated from the compression pulse travelling down the pile due to the hammer strike at the top. The pulse travels down the pile at a speed that is about 3.3 times faster than the speed of sound in the surrounding water. This results in a wave front with a cone angle of about 17° from the pile axis. In an infinitely long pile this would correspond with plane waves travelling at this Mach angle, but in realistic cases, the length of the pile in the water is finite. What does this mean for the directionality of the radiation as a function of frequency?

To investigate this, we model the pulse travelling down the pile as a 'phased array', consisting of a vertical series of monopole sound source, radiating harmonic sound with a phase delay corresponding with the compressional wave speed at which the pulse travels down the pile. The sound pressure radiated by each of these monopoles can be written as:

$$p(r,z) = F_p(r,z|r_s,z_s)s_s e^{\mathrm{i}k_p(l_0+z_s)} = s_s \frac{e^{\mathrm{i}k_w R+\mathrm{i}k_p(l_0+z_s)}}{R} \quad \text{(B 1)}$$

where $s_s$ is the (amplitude) source factor (in μPam) and $f_p(r,z|r_s,z_s)$ the corresponding propagation factor between source position $(r_s,z_s)$ and receiver position $(r,z)$. $l_0$ is the distance between the top of the pile, where it is excited by the hammer and the water surface ($z_s = 0$). The distance between source and receiver is $R = \sqrt{(r-r_s)^2+(z-z_s)^2}$. $k_w$ is the wavenumber for sound waves in water and $k_p$ is the wavenumber for the compressional waves in the pile.

For a finite length array of length $L$ at $r_s = 0$ in an infinite medium:

$$p(r,z) = \frac{1}{L}\int_0^L f_p(r,z|0,z_s)s_s e^{\mathrm{i}k_p(l_0+z_s)}dz_s = s_s e^{\mathrm{i}k_p l_0}\frac{1}{L}\int_0^L \frac{e^{\mathrm{i}k_w R+\mathrm{i}k_p z_s}}{R}dz_s \quad \text{(B 2)}$$

In the 'far field', where $r \gg L$ and $z \gg L$

$$R = \sqrt{r^2+(z-z_s)^2} \approx \sqrt{r^2+z^2-2zz_s} \approx \sqrt{r^2+z^2}\left(1-\frac{zz_s}{r^2+z^2}\right) = R_0\left(1-\frac{zz_s}{R_0^2}\right)$$

where $R_0 = \sqrt{r^2+z^2}$ is the distance from the top of the array ($z_s = 0$) to the receiver position. Then:

$$p(r,z) \approx s_s \frac{e^{\mathrm{i}k_p l_0+\mathrm{i}k_w R_0}}{R_0}\frac{1}{L}\int_0^L e^{-\mathrm{i}k_w\frac{z}{R_0}z_s+\mathrm{i}k_p z_s}dz_s \approx -\mathrm{i}s_s \frac{e^{\mathrm{i}k_p l_0+ik_w R_0}}{R_0}\frac{1-e^{-\mathrm{i}\left(k_w\frac{z}{R_0}-k_p\right)L}}{\left(k_w\frac{z}{R_0}-k_p\right)L} \quad \text{(B 3)}$$

Hence:

$$|p(r,z)|^2 \approx \left|\frac{s_s}{R_0}\right|^2 \left|\frac{\sin\left[\left(k_w\frac{z}{R_0}-k_p\right)\frac{L}{2}\right]}{\left(k_w\frac{z}{R_0}-k_p\right)\frac{L}{2}}\right|^2 \quad \text{(B 4)}$$

With observation angle $\theta$ defined by $\sin\theta = z/R_0$ and Mach-number $M = k_w/k_p$ this can be written as:

$$|p(r,z)|^2 \approx \left|\frac{s_s}{R_0}\right|^2 \left|\frac{\sin\left[\left(\sin\theta-\frac{1}{M}\right)\frac{k_w L}{2}\right]}{\left(\sin\theta-\frac{1}{M}\right)\frac{k_w L}{2}}\right|^2 \quad \text{(B 5)}$$

The function $\frac{\sin x}{x} = \operatorname{sinc} x$ is equal to 1 for small arguments ($x \ll 1$). The first zero of this function occurs when the argument $|x|$ equals $\pi$. The sound pressure level is reduced by 3 dB when $|x| \approx 1.4$. The angles at the '3 dB' beam width are:

$$\theta_{3\mathrm{dB}\pm} \approx \sin^{-1}\left(\frac{1}{M} \pm \frac{2.8}{k_w L}\right) \quad \text{(B 6)}$$

This describes a steered beam in the direction $\theta_M = \sin^{-1}\left(\frac{1}{M}\right)$, with a '3 dB' beam width dependent on $k_w L$. The lower angle of the steered beam equals zero when $f \gg \frac{1.4\, c_p}{\pi L}$

For example: the steel pile at Q7 (PAWP) the water depth was $L$=21 m and $c_p$ ≈5000 m/s, so that $M$ ≈3.3 and $\theta_M$ ≈ 17° and $\frac{1.4\, c_p}{\pi L}$ ≈106 Hz. The highest SELs were measured in the 100 Hz to 400 Hz bandwidth. The corresponding beam width at 400 Hz is $\theta_{3\mathrm{dB}\pm}$ ≈ 13° – 22°.

In the marine piling application, the sound radiation will also be influenced by the presence of the water surface. This effect has been ignored here.

# C Update of surface loss modelling

Authors: Mark Prior and Mathieu Colin, TNO

## C.1 Introduction

In spring 2018 a requirement arose to improve the handling of surface losses in propagation codes used in the calculation of the noise produced by pile-driving activities. The current implementation used an approach based on (Weston & Ching, 1989) which was considered valid only up to 4 kHz. An alternative expression by (Dahl, 2004) was available for frequencies above 10 kHz but there were implementation issues with this. These were associated with the fact that WC89 formula had a linear variation of surface loss (in nepers) with angle which was convenient to implement in a flux-based propagation model. A practical implementation (Ainslie, 2010) of Dahl, on the other hand, shows that it involves an inverse-linear relationship between loss and angle and the consequences of this on the expression for propagation were not clear.

This note sets out the consequences of the inverse-linear relationship between grazing angle and surface loss and proposes a method by which the effects of surface loss can straightforwardly be included in the existing propagation formulae in both low- and high-frequency cases.

## C.2 Caveat

The effects of rough sea-surfaces on sound propagating underwater remains an area of considerable uncertainty. The two expressions considered here have opposite dependencies on grazing angle: an absolutely fundamental level of disagreement. Other candidate formulae have quadratic dependencies on grazing angle and there is no hard reason why any formula should be preferred to another. Reviews (Jones et al, 2015) of calculations made with different expressions may attempt to identify the theoretical validity of various approaches but the fundamental physical problem of predicting the scattered acoustic field from a rough surface remains a challenging problem with no complete solution.

Comparisons of predictions with measured data are necessary for any complete validation of a surface-loss mechanism but these do not provide definitive indications of any single, ‘correct’ formula. It is common for surface-reflection-loss calculations to include empirical factors to allow for poorly understood relationships between loss and driving environmental parameters such as wind-speed or sea state. Consequently, many expressions provide good fits to the data on which their empirical elements were based. However, it is rare for an expression to give an accurate description of an independently gathered dataset.

The work reported here is an attempt to combine two expressions for surface loss into a consistent equation that avoids step-changes in behavior or predictions that defy ‘common sense’. It cannot be said to produce a validated surface model.

## C.3 Low-frequency case: Weston-Ching formula with linear relationship

The starting point for both cases is the small-angle form of the range-averaged propagation expression

$$F = \frac{2}{rh} e^{-2\beta_{Th} r} \int_0^{\theta u} e^{-\frac{r\theta}{2h}\, l(\theta)} d\theta$$

Where the propagation factor $F$ is the linear version of propagation loss, $\theta u$ is the upper angle of propagation (usually equated to the seabed critical angle), $\beta_{Th}$ is the attenuation coefficient from the Thorp formula for absorption in sea water, $r$ is the range variable and $h$ is the water depth. $l(\theta) = 2\eta_{sb}\theta$ is the loss (in nepers) per cycle range and the factor by which this is multiplied in the exponent is equal to the range expressed in cycle ranges. This loss is made up of a reflection loss at the seabed and a reflection loss at the sea surface. In the low-frequency case, both of these are proportional to angle and the expression may be written as

$$F_L = \frac{2}{rh} e^{-2\beta_{Th} r} \int_0^{\theta u} e^{-\frac{r\eta_{sb}\theta^2}{h}\, l(\theta)} \mathrm{d}\theta$$

Where $\eta_{sb} = \eta_b + \eta_s$ is the sum of the loss-gradients (in nepers per radian) for amplitude reflection at the seabed and sea-surface, such that the amplitude reflection coefficient can be written as

$$R = \exp -\eta\theta \,.$$

The value of $\eta_b$ is determined by the sediment properties and WC89 gives (Ainslie, 2010, Eq. 8.22)

$$\eta_s = 3.8 f_{kHz}{}^{\frac{3}{2}} \left(\frac{\hat{v}_{10}}{10}\right)^4$$

Where $\hat{v}_{10}$ is the wind-speed measured 10 m above the sea surface.
The flux integral reduces to

$$F_L = \sqrt{\frac{\pi}{r^3 \eta_{sb} h}}\, e^{-2\beta_{Th} r} \mathrm{erf}\left[\sqrt{\frac{r\theta_u{}^2 \eta_{sb}}{h}}\right]$$

Where the familiar "three-halves" power of range is observed for "mode stripping" conditions at ranges long enough for the erf function to have reached its large-argument value of 1.

## C.4 High-frequency case: Dahl, 2004 with inverse-linear relationship

The expression for the propagation factor in this case becomes

$$F_H = \frac{2}{rh} e^{-2\beta_{Th} r} \int_0^{\theta u} e^{-\frac{r}{h}\left(\eta_b \theta^2 + \frac{\beta_{SL}}{2}\right)}\, \mathrm{d}\theta$$

Where the reflection loss at the surface given by the simplified formula of Dahl (Ainslie, 2010; Eqs. 8.31, 8.32) is

$$\frac{\beta_{SL}}{\sin(\theta)} \approx \frac{\beta_{SL}}{\theta}$$

Where

$$\beta_{SL} = {f_{kHz}}^{0.85} 10^{-6.45+0.47\hat{v}_{10}}$$

and the loss per cycle consequently has an angle-independent term. This arises because the acoustic loss modelled by this expression is associated with absorption by the near-surface bubble layer. Total loss per surface interaction increases with path length through the layer and this is greater for shallower angles. Conversely, the number of surface interactions per unit range decreases for shallower angles and the two factors cancel to give a surface loss per cycle that is independent of propagation angle.

The angle-independent part of the exponential function can be taken outside the integral over angle which then becomes of the same form as the low-frequency case, the only difference being that the reflection-loss gradient term is due to the seabed alone. Thus

$$F_H = \sqrt{\frac{\pi}{r^3 \eta_b h}} e^{-2\left(\beta_{Th} + \frac{\beta_{SL}}{4h}\right) r} \operatorname{erf}\left[\sqrt{\frac{r {\theta_u}^2 \eta_b}{h}}\right]$$

Where the effect of the sea-surface now takes the form of an attenuation that is scaled by four times the water depth and added to the Thorp coefficient.

- Frequency-interpolated expression

The effect of the surface loss can therefore be seen to take the form of

- a modification of the seabed properties at low frequencies and
- a modification of the seawater volume-absorption coefficient at high frequencies.

This fortuitous form allows surface loss to be included in the existing propagation expressions via modifications to the seabed and water-volume properties that vary smoothly with frequency.

## C.5 Flux Formulae

In the case of propagation formulae based on flux, the propagation factor can be written as

$$F = \sqrt{\frac{\pi}{r^3 \eta h}} e^{-2\beta r} \operatorname{erf}\left[\sqrt{\frac{r {\theta_u}^2 \eta}{h}}\right]$$

Where the seabed and water-volume properties are described by parameters $\eta$ and $\beta$ that vary with frequency according to

$$\eta = \eta_b + \eta_s (1 - V(f)) W(f)$$

$$\beta = \beta_{Th} + \frac{\beta_{SL}}{4h} V(f)$$

And the transition between very-low, low and high-frequency cases are handled by smooth window functions $V(f)$ and $W(f)$ such that

$$V(f) = \frac{1}{2}\left(1 + \mathrm{erf}\left[\frac{(f_{kHz} - 7.5)}{2}\right]\right)$$

$$W(f) = \frac{1}{2}\left(1 + \mathrm{erf}\left[\frac{\left(8f_{kHz} - 4(1 + f_{c\,kHz})\right)}{(1 - f_{c\,kHz})}\right]\right);\ f_{c\,kHz} < 1$$

$$W(f) = 1\ ;\ f_{c\,kHz} > 1$$

The form of $V(f)$ is chosen simply to make a smooth changeover between low- and high-frequency cases between 4 kHz (the upper frequency for WC89) and 10kHz (the lower frequency for Dahl, 2004). The presence of an erf[] function in the expressions for $V(f)$ and $F$ is coincidental.

The weighting function $W(f)$ is used to account for cases where the windspeed is high enough for surface effects to be significant at frequencies below the lower frequency-limit of the WC89 dataset. This is quoted as being 1 kHz and for lower windspeeds, WC89 will predict only very small surface effects below this frequency. However, for higher windspeeds, it is possible that the effects of the surface will be significant at 1 kHz. If the equation is applied 'sharply' (i.e. no surface losses are calculated below 1 kHz) then the spectra of predicted signals will show an unphysical step-change at this frequency.
To avoid this, $W(f)$ smoothly removes the effect of the sea surface for high windspeeds at frequencies below $f_{c\,kHz}$. This value represents an estimate of the minimum frequency at which the rough sea surface is likely to be acoustically significant. To estimate $f_{c\,kHz}$ an expression (Jensen et al., 2000) for the reflection coefficient $R$ from a sea surface with a Pierson-Moskowitz spectrum is used

$$R = e^{-\frac{\gamma^2}{2}}$$

Where

$$\gamma = 2k\sigma \sin\theta$$

And $\gamma$ is a measure of the acoustically scaled surface roughness for propagation at angle $\theta$ with acoustic wavenumber $k$, and sea-surface rms height $\sigma$. For the Pierson-Moskowitz spectrum this is given by

$$\sigma = \sqrt{\frac{\alpha \hat{v}_{10}{}^4}{4\beta_{PM} g^2}}$$

Where $\alpha$ = 0.0081, $\beta_{PM}$=0.74, and g is the acceleration due to gravity. Setting a critical value for $R$ of 0.90 and averaging over angle such that a sine-squared term is average to 0.5 gives

$$f_{c\,kHz} = \left(\frac{3.79}{\hat{v}_{10}}\right)^2$$

So that, for example, for a windspeed of 10 m/s, surface effects should be considered for frequencies greater than 144 Hz and for 6 m/s for frequencies greater than 400Hz. $W(f)$ forces a smooth increase in the predicted effects of the wind between $f_{c\,kHz}$ and 1 kHz but the function is a simple heuristic to avoid step-

changes in predicted signal spectra. For low windspeeds (<3.79 m/s), it is possible that $f_{c\,kHz}$ will be greater than 1 kHz and in these cases, $W(f)$ is set to 1 for all frequencies but the effects of the surface roughness will be small so that step-changes in predicted spectra should not be observed.

## C.6 Non-flux formulae

For propagation models not based on the concept of acoustic flux, the effects of surface roughness in the regime of (Dahl, 2004) can be incorporated directly by modification of the sea-water attenuation in the way described above. The only possible exception to this is for propagation models that use internal calculations of sea-water attenuation, rather than allowing the user to specify a value. Low-frequency effects, however, cannot be implemented by an addition of $\eta_s$ to $\eta$ because the parameter is used only in flux-based formulae. However, the same effect can be achieved by modifying the seabed intrinsic attenuation (usually measured in dB per wavelength) to a value that would give the modified value of $\eta$ . Equations 8.71, 8.73, 8.76, 8.77 and 8.86 from (Ainslie, 2010) give (for coarse-grained sediments, in which $\frac{c_{water}}{c_{sed}} < 1$):

$$\eta_B = \frac{\rho_{sed}}{\rho_{water}} \frac{\log_e(10)}{20\pi} \beta_{sed} \frac{\cos^2(\psi_c)}{\sin^3(\psi_c)}$$

Where $\rho_{sed}$ is the density of the sediment and $\rho_{water}$ is that of water, $\beta_{sed}$ is the attenuation coefficient of the sediment expressed in dB per wavelength and $\psi_c$ is the critical angle of the seabed, given by

$$\psi_c = \operatorname{acos}\left(\frac{c_{water}}{c_{sed}}\right)$$

The effects of the sea surface may be included in the propagation model via a modification of the seabed intrinsic attenuation from $\beta_{sed}$ to a value $\beta_{eff}$ which would replace $\eta_B$ in the equation above by

$$\eta = \eta_B + \eta_s(1 - V(f))W(f)$$

This value is given by

$$\beta_{eff} = \beta_{sed} + \frac{3.8 f_{kHz}^{\frac{3}{2}} \left(\frac{\hat{v}_{10}}{10}\right)^4 (1 - V(f))W(f)}{\frac{\rho_{sed}}{\rho_{water}} \frac{\log_e(10)}{20\pi} \frac{\cos^2(\psi_c)}{\sin^3(\psi_c)}}$$

So that the effect of the windspeed takes the form of a modification to the seabed attenuation.

## C.7 Results

Example results of the interpolated algorithm are shown below for a flux-based model of propagation.

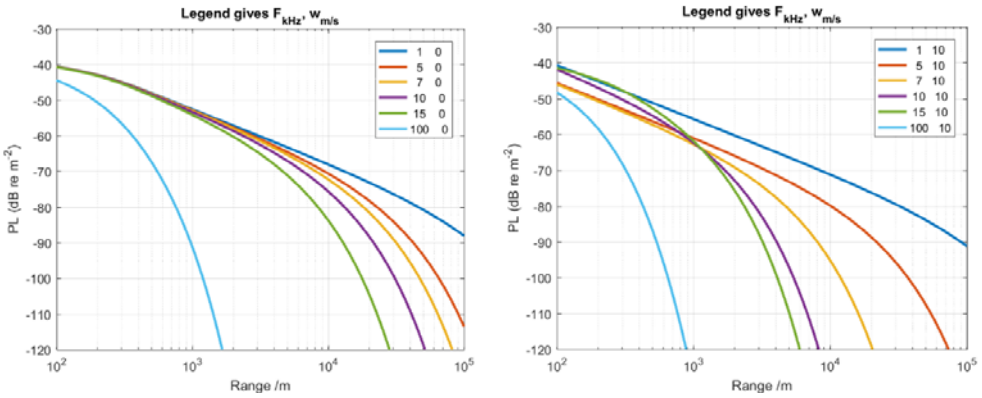


Figure C.1 PL versus range at various frequencies given in the legend in kHz, together with the wind speed in m/s.

It is interesting to note in the case of the 10 m/s wind that the frequency order in which loss increases changes with range, i.e. at short ranges the 15 kHz frequency has the lowest loss but at ranges beyond a few km, this loss is higher than all but the 100 kHz curve.

This behaviour arises because the low-frequency expression causes a downward shift of the $15 \log R$ curve while the high-frequency expression changes the shape of the curve, causing it to fall off more rapidly with range. Thus, the 5 kHz curve is shifted down the axes at short ranges but emerges from beneath the higher frequency curves as these are attenuated with range. The same effect is observed in the 'kinks' in the contours of the figure below.

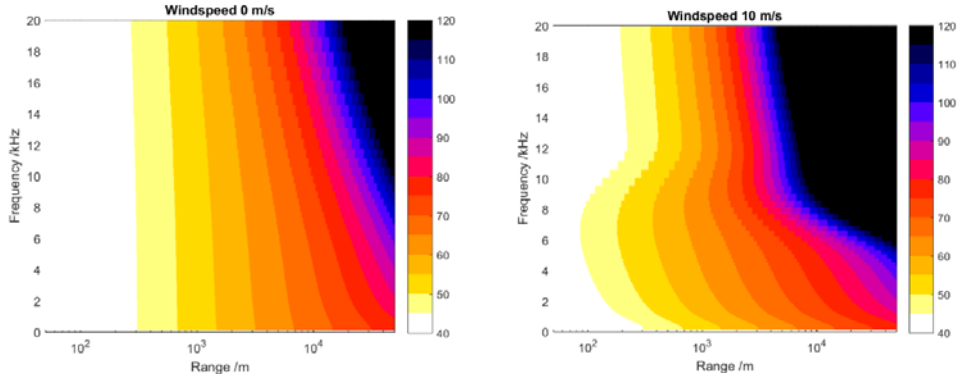


Figure C.2 Contours of propagation loss versus range and frequency.

The location and shape of the 'kinks' are determined by the interpolation functions $V(f)$ and $W(f)$ and, since these are heuristics, the precise value of the frequency of minimum loss should be regarded as doubtful. Nonetheless, the two surface-loss expressions have frequency limits which are stated by their authors and the 'kinks' will inevitably be found in the region between these bounds: 4 kHz to 10 kHz where there is a changeover between formulae.

It should be noted the that 'kinks' are not present at ranges beyond a few km and loss increases monotonically with frequency at long ranges.

## C.8 Extension to range-varying water depth

The expressions derived so far are specific to environments that do not vary with range from the source. Real environments change horizontally in (potentially) all parameters. Some models allow the user to specify range-varying environmental properties and the effects of sea-surface can be incorporated in these via changes to the seabed and seawater attenuation properties.
However, changes of seabed type and wind-speed are difficult to incorporate in flux-based models. The effect of range-dependent water depth can, to a first approximation be incorporated in the modification to the volume absorption coefficient in the following way.
We begin with

$$F = \sqrt{\frac{\pi}{r^3 \eta h}} e^{-2\beta r} \operatorname{erf}\left[\sqrt{\frac{r{\theta_u}^2 \eta}{h}}\right]$$

Where

$$\eta = \eta_b + \eta_s(1 - V(f))$$

$$\beta = \beta_{Th} + \frac{\beta_{SL}}{4h} V(f)$$

$$V(f) = \frac{1}{2}\left(1 + \operatorname{erf}\left[\frac{(f_{kHz} - 7.5)}{2}\right]\right)$$

Restricting considerations of range-varying bathymetry to its effect on $\beta$ , the term of interest is

$$e^{-2\beta_{Th} r + \frac{\beta_{SL} V(f) r}{2} \frac{}{h}}$$

Multiplication of a single-valued reciprocal water depth can be replaced with integration over range of a range-dependent value. The decay term then becomes is

$$e^{-2\beta_{Th} r + \frac{\beta_{SL} V(f)}{2} \int_0^r \frac{1}{h(s)} ds}$$

Which can be re-written more concisely as

$$e^{-2\left(\beta_{Th} + \frac{\beta_{SL} V(f)}{4} \frac{1}{r} \int_0^r \frac{1}{h(s)} ds\right) r}$$

And hence

$$e^{-2\left(\beta_{Th} + \frac{\beta_{SL} V(f)}{4} \overline{\left(\frac{1}{h}\right)}\right) r}$$

Thus, the effect or range-dependent water depth is included via the use of a range-averaged reciprocal water depth. The additional depth-dependent surface loss term can be straightforwardly added to all Aquarius models using the Matlab “cumsum” routine.

# D Contribution of bottom path

In attempt to quantify the contribution of sound propagating through the seabed under the bubble screen and to what extent that path contributes to the assessment of the effectiveness of the screen, we have built a simple model, which is described below. This model focusses on the effects of the distance between pile and the bubble screen and the distance to the measurement position.

Figure D.1 shows a schematic representation of a monopole radiating sound into water column and sediment at two distinct Mach angles. The blue line represent the direction of the wave front radiating from the downward travelling wave in the monopile into the water. The Mach grazing angle of this wave front for a steel pile in water is given by:

$$\theta_{M,w} = \sin^{-1}\left(\frac{c_w}{c_{pile,w}}\right) \approx \sin^{-1}\left(\frac{1500}{5012}\right) \approx 17.4 \text{ deg}$$

The red line represents the direction of the wave front radiating from the upward travelling wave in the buried part of the pile into the sediment. The wave front grazing angle in the sediment (medium sand) and water is given by:

$$\theta_{M,s} = \sin^{-1}\left(\frac{c_s}{c_{pile,s}}\right) \approx \sin^{-1}\left(\frac{1797}{5082}\right) \approx 20.7 \text{ deg}$$

At the sediment-water interface, the wave front of this wave refracts into the water according to Snell's law, resulting in refracted wave grazing angle

$$\theta_{Ms,w} = \cos^{-1}\left(\cos(\theta_{M,s}) \cdot \frac{c_w}{c_s}\right) \approx 38.7 \text{ deg}$$

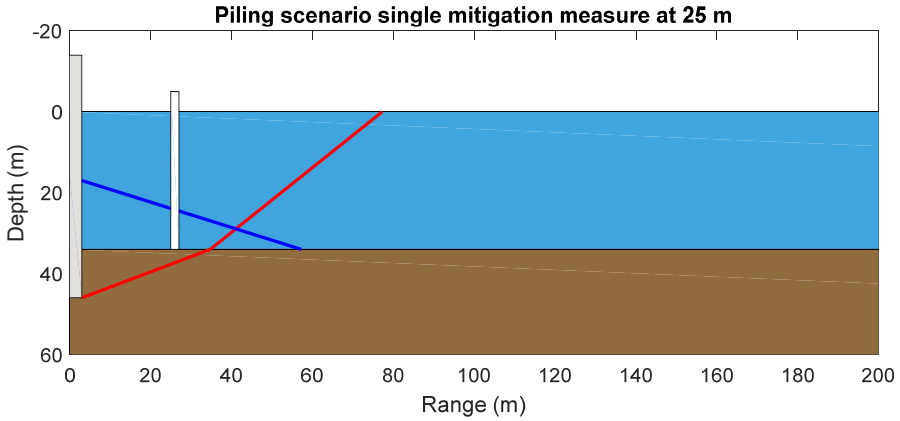


Figure D.1 Schematic representation of a pile radiating sound at two distinct Mach angles for the downward travelling wave in water (blue) and the upward travelling wave in the water and the sediment(red). See text for further explanation.

In order to estimate the contribution of the sediment-borne path relative to the water-borne path, the following parameters need to be quantified:

- Sand and water acoustic model parameters
- The reflection loss at the end of the pile $R_{pile,end}$
- The transmission loss when the wave transits through the sediment water interface $T_{s,w} = 1 + R_{s,w}$ at $\theta_s$.
- The reflection loss of the two wave fronts $(R_w, R_{s,w})$ at the water sediment interface at grazing angles $\theta_w$ and $\theta_{s,w}$
- The number of interaction of the waves with the sediment, described by their cycle distances $d_w$ and $d_{s,w}$
- The relative source level energy of the pile section in the sediment to the section in the water column
- The effectiveness of the mitigation measures for both the water and sediment born paths

The following water, sediment and pile parameters are used as input for the equations below:
$\rho_w = 1024\ kg/m^3, c_w = 1500\ m/s$
$\rho_s = 2136\ kg/m^3, c_s = 1797\ m/s, \alpha_s = 0.88\ dB/\lambda$
$\rho_p = 7750\ kg/m^3, c_{p,s} = 5082\ m/s, c_{p,w} = 5051\ m/s$

For perpendicular incidence at the end of the pile, the reflection loss at the lower end of the pile is (with $Z = \rho c$):

$$R_{pile,end} = -20 \log_{10}\left(\left|\frac{Z_s - Z_{p,s}}{Z_S + Z_{p,s}}\right|\right) = 1.7\ dB$$

Figure D.2 shows the reflection loss at the water sediment interface and the transmission loss for propagation from the sediment to the water layer. The values have been computed using the theory described in [Ainslie, 1995].

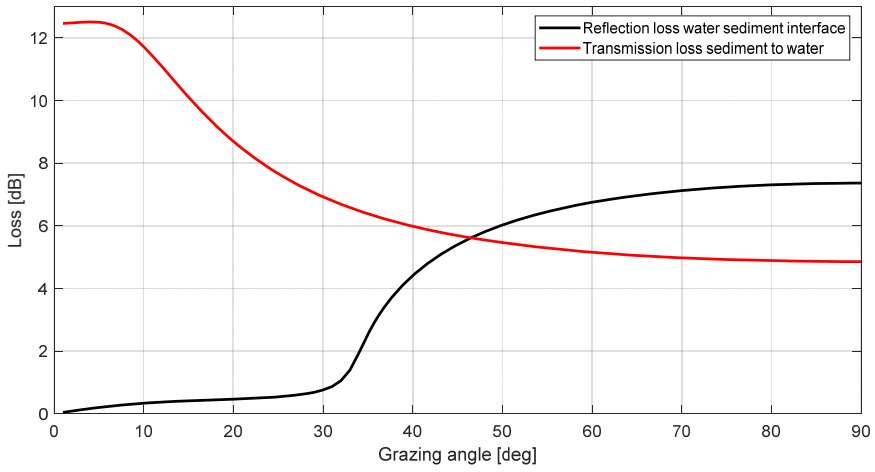


Figure D.2 reflection loss at the water sediment interface and the transmission loss for propagation from the sediment to the water layer.

From this figure, the following values are obtained for $\theta_s, \theta_w$ and $\theta_{s,w}$

$$T_{s,w}(\theta_s) = 8.5\ dB, \qquad R_w(\theta_w) = 0.436\ dB, \qquad R_{s,w}(\theta_{s,w}) = 4.026\ dB$$

The cycle distances for a 34 m water depth in meters is $d = \frac{2H}{\tan\theta}$, which gives $d_{s,w}$=85 m and $d_w$=217 m.

The last two parameters, i.e. the relative energy source level of the pile in the sediment and the effectiveness of the mitigation are difficult to quantify. The relative source level of the pile will depend on the penetration depth which will change during the pile driving process. Also, for small penetration depth, it is likely that a significant portion of the bottom born path enters the water column before the mitigation measure, resulting in additional attenuation. With regard to the efficiency of the mitigation measure, its efficiency dependent on frequency and on the incident angle. In order ensure that the relative contribution of the bottom born path is not underestimated, it is assumed that it is (i) not affected by the mitigation measure (i.e. it enters the water column after, as shown in figure 1) and that it radiates over the same pile length as the pile section in the water.

Figure D.3 shows the modelled losses of the water and sediment born path, using the loss factors computed above. For the water born path, the curve are shown for no mitigation (0 dB), a single bubble curtain (~10 dB) and a double bubble (~14 dB), where the mitigation measure effectivity is based on the lower limit values presented for single and double bubble curtains in table 1 of [Bellmann, 2014].
The effect of the screens is modelled by subtracting their effect from the water born path at 25 meter (10 dB) and 50 meter (4 dB) distance from the pile.
Comparing the sediment born path front against the water born path shows that the larger grazing angle of the bottom born part in the water results in an decreasing relevance with range. At ten times the water depth (340 m) the difference between the sediment born path and the single\double bubble screen is already 11.6/7.6 dB respectively. At shorter ranges it follows from these results that the bottom borne path might limit the effectiveness of the mitigation measure.

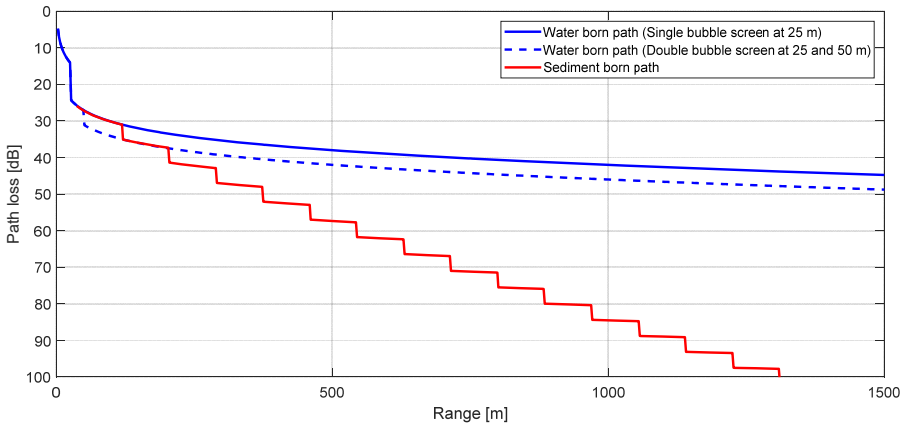


Figure D.3 propagation loss as a function of distance, for fluid- and sediment-borne sound transmission and for two scenarios: a single and a double bubble curtain.

The following notes should however be considered regarding the accuracy of this observation

- For a finite pile length, the wave front is not only radiating at the Mach angle, and in particular at lower frequencies and small penetration depth this assumption becomes increasingly invalid. Wave radiating smaller grazing angles are less efficiently transmitting into the water column, but propagate more efficiently after because of their reduced grazing angle.
- It is very likely, in particular for a second bubble screen, that the sediment borne path will be affected.